ACSNANO

www.acsnano.org

REVIEW

Photothermal Microscopy: Imaging the Optical Absorption of Single Nanoparticles and Single Molecules

Subhasis Adhikari, Patrick Spaeth, Ashish Kar, Martin Dieter Baaske, Saumyakanti Khatua,* and Michel Orrit*

Cite This: *ACS Nano* 2020, 14, 16414−16445

Read Online

ACCESS | Metrics & More | Article Recommendations

ABSTRACT: The photothermal (PT) signal arises from slight changes of the index of refraction in a sample due to absorption of a heating light beam. Refractive index changes are measured with a second probing beam, usually of a different color. In the past two decades, this all-optical detection method has reached the sensitivity of single particles and single molecules, which gave birth to original applications in material science and biology. PT microscopy enables shot-noise-limited detection of individual nanoabsorbers among strong scatterers and circumvents many of the limitations of fluorescence-based detection. This review describes the theoretical basis of PT microscopy, the methodological developments that improved its sensitivity toward single-nanoparticle and single-molecule imaging, and a vast number of applications to single-nanoparticle imaging and tracking in material science and in cellular biology.

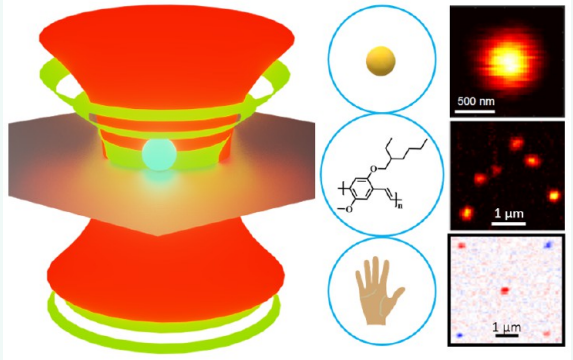

KEYWORDS: *photothermal microscopy, single-molecule imaging, single-particle absorption spectroscopy, nanoparticles, label-free imaging, thermoplasmonics, nonlinear spectroscopy, nano-optics, live-cell imaging, thermal lens microscopy*

INTRODUCTION

In the past 30 years, the optical detection of single molecules and nanoparticles has had a tremendous impact on investigations of biological and condensed-matter systems, as well as on our understanding of complex photophysics in molecular systems.[1,2] Despite the fact that the first single-molecule detection was based on its absorption,[3] fluorescence-based detection[4] is overwhelmingly more common owing to its easier implementation and very low background. However, fluorescence-based detection schemes suffer from two major drawbacks: (i) the photoblinking and photobleaching of fluorophores and (ii) their limitation to a narrow class of molecular probes with high fluorescence quantum yields. The past two decades have seen several demonstrations of single nano-object detection through nonfluorescent approaches.[5] Notable examples of such methods include spatial modulation spectroscopy,[6−8] ground-state depletion microscopy,[9] interferometric scattering microscopy (iSCAT),[10−13] direct extinction-based methods using balanced photodiodes,[14−16] optical microresonators,[17−19] photothermal microscopy,[20−29] nanomechanical photothermal sensing,[30] and photothermal-induced resonance (PTIR) spectroscopy also known as AFM-IR.[31] Among them, photothermal microscopy addresses absorbing nano-objects that do not necessarily fluoresce and has shown great promise to overcome several of the limitations of single-molecule fluorescence. This review will focus on describing various photothermal microscopic techniques and their applications in material science and biology.

Photothermal detection is based on the absorption of a heating beam by a small sample, down to a single nano-object, usually a metal nanoparticle. Heat absorbed by the particle and released in its environment gives rise to a temperature gradient and thereby to a refractive index gradient surrounding the

Received: September 10, 2020
Accepted: November 16, 2020
Published: November 20, 2020

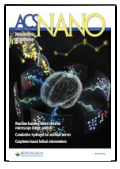

https://dx.doi.org/10.1021/acsnano.0c07638
ACS Nano 2020, 14, 16414−16445

heated nano-object, called the thermal lens. This thermal lens is then imaged through scattering of a probe beam, generally at a different wavelength from the heating beam to facilitate rejection of the intense heating light by spectral filters. The photothermal signal is the change of probe intensity caused by the absorption of the heating beam and is therefore a nonlinear signal caused by a nonlinear susceptibility of the $\chi^{(3)}$ type,[32] similar to pump−probe measurements. It arises from cross-talk between two beams with different colors and is therefore easy to detect in a difference measurement of the probe intensity, from where stray heating light is very thoroughly removed by spectral filters. This detection method benefits from very low background because the medium surrounding the objects of interest is usually transparent, and its $\chi^{(3)}$ susceptibility, being of nonresonant electronic origin, is very low. Any electronic or vibrational absorbing level of the objects of interest will resonantly enhance the local $\chi^{(3)}$ and thereby provide optical contrast.

In photothermal microscopy, the contrast arises from the long-lived temperature changes caused by absorption of the heating beam. The ensuing change of optical response of the medium and/or of the object itself is detected by modulating the heating intensity at a high frequency and by analyzing the scattered probe intensity with a lock-in amplifier, after careful removal of stray heating light by high-quality spectral filters. In the 1990s, Kitamori and co-workers[33] proposed the thermal lens microscopy to detect very small amounts of absorbing microparticles in solutions. They later demonstrated detection of single nanometer-sized particles[34] and of very low concentrations of nonfluorescent molecules[35] in solutions. Thermal lens microscopy has mainly been implemented for detecting diffusing nanoparticles in suspension or in microfluidics with a rather low modulation frequency of the heating beam. To image immobilized nanoparticles, Boyer *et al.*[20] proposed a photothermal technique derived from differential interference contrast (DIC) microscopy, known as photothermal interference contrast (PIC) microscopy. PIC uses a high-frequency modulation of the heating beam, typically in the MHz range, better to reject the low-frequency $1/f$ noise. The PIC phase signal was transformed into an intensity change through interference between a reference and a probe beam having orthogonal polarizations. The modulated heating beam induced a modulation of the interference signal, which was sensitively detected by a lock-in amplifier. The PIC method successfully demonstrated imaging of single 2.4 nm gold nanoparticles. However, the PIC method required a perfect overlap between the heating beam and the probe beam and, just as DIC microscopy, was sensitive to polarization defects of the setup or of the specimen. To overcome these limitations, Berciaud *et al.*[36] proposed a variant of the thermal lens method, which they dubbed photothermal heterodyne imaging (PHI), which became the most common method for photothermal imaging of single absorbing nano-objects. The PHI method simplifies PIC and avoids its polarization limitations by replacing two-beam polarization interference with an interference between scattering of a single probe beam and a reference which, most conveniently, can be the reflected or transmitted probe beam. The simpler setup and careful optimization of the method led to detection and imaging of single gold nanoparticles of 1.4 nm diameter (Nanogold) with a signal-to-noise ratio of more than 10, an integration time of 10 ms, and shot-noise-limited detection.

In the past two decades, various implementations of photothermal microscopy and spectroscopy have been developed for a wide variety of applications in biology and in material science. For example, photothermal imaging was used to detect tiny nano-objects such as single metal nanoparticles down to 1.4 nm diameter,[21] semiconductor nanocrystals,[36] carbon nanotubes,[37] conjugated polymers,[23] single nonabsorbing proteins,[38] and even single organic dye molecules.[22] Photothermal absorption spectroscopy[28,39] revealed characteristic intrinsic size effects on the gold nanoparticles' surface plasmon. Photothermal correlation spectroscopy[40,41] turned out to be a potential alternative to fluorescence correlation spectroscopy for nonfluorescent labels in biological applications. Similar to fluorescence image correlation spectroscopy,[42] photothermal raster image correlation spectroscopy[43] (PhRICS) promised to be a superior technique for investigating dynamical processes in a living cell. The photothermal signal of a gold nanorod[44] depends on the heating beam's polarization and can be used to study orientational dynamics in soft matter and biological systems. Heber *et al.*[45] used single-particle photothermal deflection microscopy to measure anisotropic thermal transport in the liquid crystal 5CB. Bogart *et al.*[46] demonstrated photothermal imaging of superparamagnetic iron oxide nanoparticles for biomedical applications. Photothermal microscopy also demonstrated label-free imaging in living cells due to absorption of endogenous organelles such as mitochondria,[47−49] lysosomes,[50] hemoglobin in red cells,[48] and melanin[51−53] in cancer cells.

As a nonlinear optical technique, photothermal microscopy offers specific advantages over linear optical methods such as fluorescence. Optical sectioning is the ability of a nonlinear method, such as two-photon-excited fluorescence[54−56] to isolate the signal from a single spot in a 3D specimen, with negligible background from the out-of-focus slices of the specimen. Because the photothermal signal arises from the overlap of heating and probe point-spread functions, it also features optical sectioning.[57,58] Another advantage is the option to fulfill contradictory requirements in an optical experiment by separating these requirements independently on the heating and the probing beam, enabling functionalities that would be out of reach of any linear technique. A case in point is the implementation of IR spectroscopy for chemical characterization in cell biology or material science. Direct IR absorption spectroscopy is limited to a poor spatial resolution by the diffraction limit of the large IR wavelengths and by the poor imaging quality of IR optics. To overcome the poor spatial resolution, Cheng and colleagues[59] have combined IR heating and visible probing to associate the chemical contrast of IR spectroscopy with diffraction-limited imaging in the visible by photothermal microscopy. The spatial resolution was determined by the probe beam, whereas the spectral resolution was provided by the IR beam. Several articles[59−65] reported improvement of spatial resolution using visible light as a probe beam in the so-called mid-IR photothermal microscopy and obtained comparable Fourier transform infrared spectra[66,67] on much smaller samples. Mid-IR photothermal imaging was also combined with Raman spectroscopy to obtain chemical fingerprint Raman spectra with higher spatial resolution.[68] Furthermore, photothermal imaging was implemented into wide-field imaging,[61] which improved the imaging speed and offers the possibility of tracking faster dynamics in biological studies. The photothermal scheme also facilitates fulfillment of

https://dx.doi.org/10.1021/acsnano.0c07638
ACS Nano 2020, 14, 16414−16445

experimental requirements on spectral tunability or controlled polarization by separating them between heating and probe beams, as we will see below. The general photothermal scheme has also been applied to study the extremely complex dynamics of nanobubbles forming around an overheated nanoparticle. The nanobubble formation was usually demonstrated using a pulsed laser[69−71] as a heating beam source. Hou *et al.*[72] demonstrated nanobubble formation and kinetics under continuous wave (CW) laser heating, using another CW laser as the probe. Whereas the standard photothermal techniques use a lock-in amplifier to detect the modulated probe signal, with a lower bound of hundreds of microseconds for the temporal resolution, the direct, lock-in-free detection of the scattered probe signal enables the capture of nanobubble dynamics in the nanosecond regime. Hou *et al.*[72] used a fast oscilloscope connected to a fast photodiode to record the nanobubble's explosive behavior and found that the rise and decay times of the bubble were on the order of a few tens of nanoseconds.

PRINCIPAL MODALITIES, BASIC THEORY OF PHOTOTHERMAL DETECTION, AND ADVANTAGES

Photothermal microscopy, also known as thermal lens microscopy[73] (TLM), detects the small additional divergence of a transmitted probe beam through the heating-induced thermal lens, *i.e.*, the refractive index gradient around a heated nanoparticle due to the embedding medium's change in temperature-dependent refractive index (Figure 1II). An additional contribution may arise from the change of optical properties of the nanoparticle itself with temperature, but as the nanoparticle is assumed to be very small, its contribution will be neglected[74] in the following discussion. Thermal lens microscopy has detected micro- and nanoparticles diffusing in solutions and was employed in numerous applications, specifically in biological systems[73,75,76] and microfluidics.[77−80] The induced thermal lens acts as a concave lens in usual media with negative thermorefractive coefficients ($dn/dT < 0$), and the divergence of the transmitted beam can be measured using a pinhole detector as a decrease in total transmitted intensity.[79] TLM uses coaxial pump and probe beams with a small axial focusing offset to obtain a thermal-lens-induced photothermal signal (with zero offset, the incoming wave is focused on the exact center of the thermal lens, and its convergence is not modified, so that the photothermal signal vanishes). Figure 1I depicts the basic principle of thermal lens microscopy schematically. The pioneering work of Kitamori, Sawada, and co-workers led to numerous applications of the thermal lens microscopy, which are described in detail in several reviews.[77,79,81,82]

Principal Methods. Typically, two different strategies are used for the photothermal imaging of single nanoparticles: (i) photothermal interference contrast imaging[20,83] and (ii) photothermal heterodyne imaging,[24,36] a simpler implementation of thermal lens microscopy. Both of these techniques are pump−probe-based methods. Furthermore, Selmke *et al.*[26] reported a probe-free photothermal detection technique which uses a single laser beam. The basic principles of these techniques are briefly described below.

Photothermal Interference Contrast Method. Pioneers Kitamori and Sawada[34,84] mainly focused on detecting absorption signals of single micro- and nanoparticles diffusing in the solution using the thermal lens spectroscopy. For imaging single immobilized metal nanoparticles, Boyer *et al.*[20]

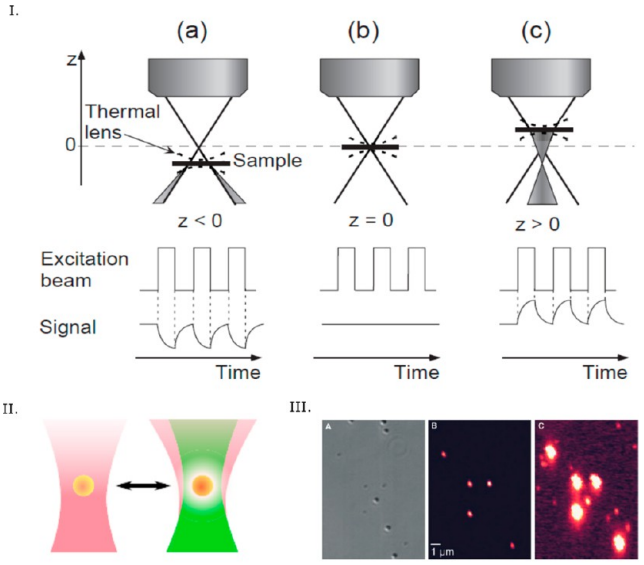

Figure 1. (I) Principle of thermal lens microscopy. The photothermal signal is either positive or negative, depending on the positive or negative offset between the coaxial pump and probe beams, as the thermal lens acts as a diverging or converging lens. The signal vanishes for zero offset. Reprinted with permission from ref 81. Copyright 2000 The Japan Society of Applied Physics. (II) Principle of photothermal microscopy: divergence of the probe beam (purple) induced by the thermal lens (white) around the nanoparticle (yellow) due to the illumination of the heating beam (green). Reprinted from ref 5. Copyright 2019 American Chemical Society. (III) Photothermal microscopy is insensitive to nonabsorbing scatterers such as latex beads. (Left) Differential interference contrast (DIC) image and (middle and right) photothermal image of a sample consisting a mixture of single 300 nm latex beads, single 80 nm gold nanopsheres, and single 10 nm gold nanospheres. In the DIC image, the strong scattering objects are the latex beads, weakly scattering objects are single 80 nm gold nanoparticles, and single 10 nm gold nanoparticles are not visible. In the photothermal image at low excitation power (middle), only single 80 nm gold nanoparticles are visible, and in the photothermal image at high excitation power (right), both types of gold nanoparticles are visible, but the strongly scattering latex beads are not visible. Reprinted with permission from ref 20. Copyright 2002 The American Association for the Advancement of Science.

proposed a sensitive polarization interference method similar to the differential interference contrast method. This method detected the absorption signal by measuring the slight phase change of a probe beam due to the heating of a metal nanoparticle. The schematic of the microscopic setup is shown in Figure 2a. They used a heating laser at 514 nm modulated in the high-frequency range of 100 kHz to 1 MHz using an acousto-optic modulator (AOM). The high-frequency modulation was the key of this method to improve the signal-to-noise by rejecting low-frequency noise. Similar to the DIC method, a linearly (horizontally) polarized probe beam (wavelength of 633 nm) was split into two orthogonally polarized beams by a Wollaston prism rotated at a 45° angle and then focused by a microscope objective on the objective plane. The angular displacement of the two polarized beams (*i.e.*, the two arms of the interferometer) by the Wollaston prism was about 0.1°, which created two diffraction-limited image spots spatially separated by 1.2 μm. The heating beam was then overlapped with one of these two arms using a

https://dx.doi.org/10.1021/acsnano.0c07638
ACS Nano 2020, 14, 16414−16445

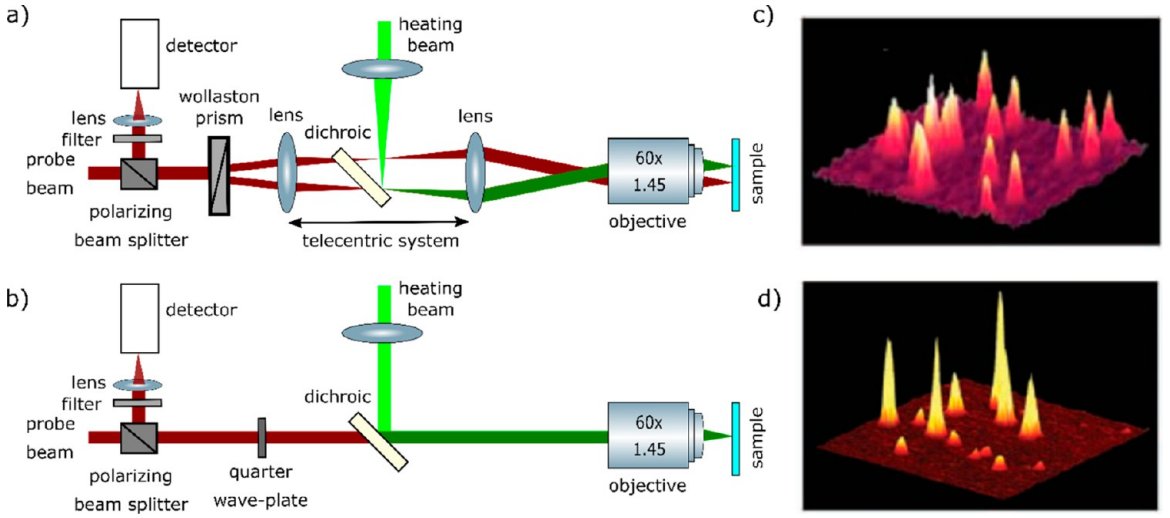

Figure 2. Experimental setup for (a) PIC and (b) PHI. (c) 10 × 10 μm^2 photothermal image of single 5 nm gold nanospheres using the PIC method and (d) 10 × 10 μm^2 photothermal image of single 2 nm (short peaks) and 5 nm (tall peaks) gold nanospheres using the PHI method. Adapted from ref 88. Copyright 2008 American Chemical Society.

telecentric lens system and then focused by the same objective. Therefore, the non-overlapped arm acted as a reference path for the interferometer. Similar to the DIC method, in the detection path, two orthogonally polarized probe beams were recombined at the Wollaston prism, and due to the phase difference of two polarizations, the vertically polarized component of the probe beam was reflected at the polarizing cube. The reflected beam was then sent to a fast photodiode, and the photothermal signal was detected by a lock-in amplifier which demodulated the interference signal at the same modulation frequency as the heating beam.

In this configuration, two key optimizations were very necessary: (i) overlapping the heating beam with the probe beam to maximize the photothermal signal and (ii) avoiding depolarization effects from the optical elements in the setup. The depolarizing effect of a high numerical aperture (NA) microscope objective usually degraded the overlapping between two interferometric paths of the probe beam in the detection and consequently resulted in a lower detection sensitivity. Therefore, this method required high excitation intensity (20 MW/cm^2) of the heating beam to obtain an optimal signal-to-noise ratio (SNR). This high excitation power is not ideal for applications in biological systems. Nevertheless, using this method, the authors were able to image single 5 nm gold nanoparticles[20] with a SNR of more than 10 and even single 2.4 nm gold nanoparticles with a SNR of 2 and an integration time of 10 ms. In addition to the high sensitivity of PIC in detecting single absorbing nano-objects, the method was insensitive to nonabsorbing strong scattering objects such as 300 nm latex beads, as shown in Figure 1III. The reduction of the strong scattering background using photothermal contrast was a benefit for imaging in biological systems. Indeed, using PIC, Cognet *et al.*[83] demonstrated photothermal imaging of single receptor proteins labeled with individual 10 nm gold nanoparticles in the plasma membrane of COS7 cells. The PIC configuration was also later implemented in the thermal lens microscopy for analysis of diffusing molecules in solution[85−87] and was termed DIC-TLM.

Photothermal Heterodyne Imaging. As an alternative to the PIC method, Berciaud *et al.*[36] proposed a simpler and more sensitive implementation of the thermal lens method which they called photothermal heterodyne imaging. This method uses a single probe beam path instead of the two probe beam paths used in PIC. This simplified optical scheme avoids depolarization limitations and residual imbalances between the two arms of the PIC interferometer. In this configuration, the same probe beam or its reflection acts as a reference beam, and the interference occurs between the scattered probe beam and the reference beam, similar to the so-called interferometric scattering (iSCAT) technique.[89] The reference beam can be either the reflected beam coming from the interface between the sample and the coverslip or the transmitted beam. The schematic of the PHI setup is shown in Figure 2b. A heating beam at 532 nm wavelength was modulated using an acousto-optic modulator in the high-frequency range of 100 kHz to 15 MHz. A CW probe beam at 720 nm wavelength was overlapped with the heating beam in the sample using a high NA objective. A combination of a quarter-wave plate and a polarizing beamsplitter was used to collect the scattered signal, which was finally detected by a fast photodiode. The lock-in amplifier detected the modulation of the scattered probe field at the heating beam modulation frequency. Using PHI, Berciaud *et al.*[36] were able to image individual nonfluorescent semiconducting nanocrystals whose absorption showed non-blinking behavior, and they were able to measure the room-temperature absorption spectra of single semiconducting nanocrystals.[90]

Because of its high sensitivity and simplicity, PHI imaging has become the most common method for photothermal imaging of single nanoparticles. PHI imaging[24] has been demonstrated in backward (*i.e.*, reflection) and forward (*i.e.*, transmission) detection modes (see Figure 3I,II). In the forward detection mode, an additional microscope objective was needed to collect the interference signal. Although at higher frequency (>1 MHz) the photothermal signal in both detection modes were found to be similar, at lower frequency, the photothermal signal in the backward detection mode was found to be smaller than that of the forward detection mode (Figure 3III). This difference arises from the size of the modulated thermal lens, which is larger at low modulation frequencies and scatters more strongly in the forward direction

https://dx.doi.org/10.1021/acsnano.0c07638
ACS Nano 2020, 14, 16414−16445

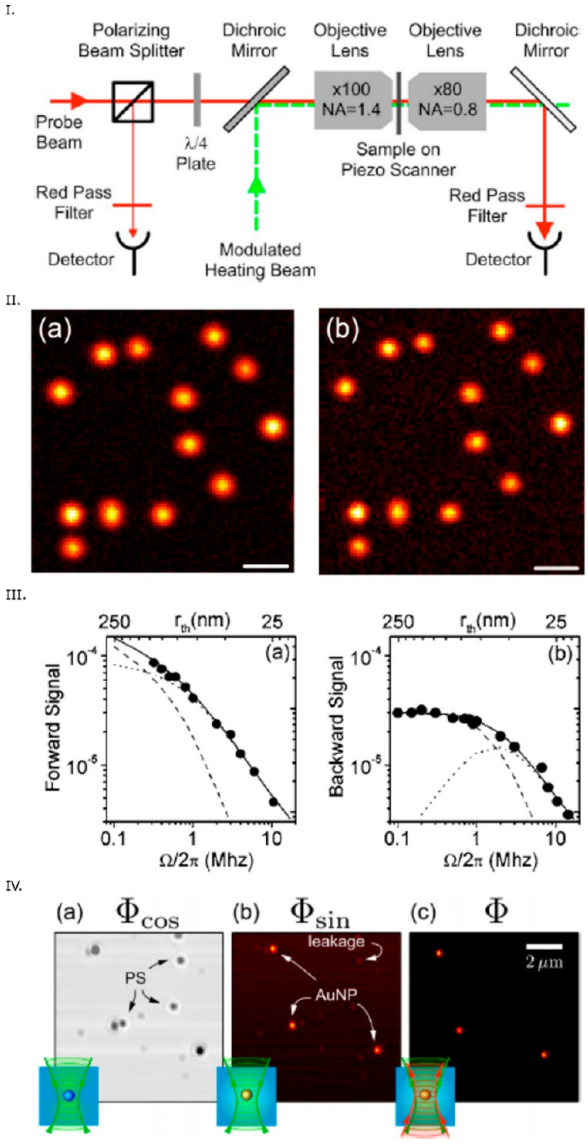

Figure 3. (I) Scheme of a PHI microscope offering both backward and forward configurations. The forward detection mode requires an additional microscope objective. (II) Photothermal image of single 10 nm gold NPs in (a) backward and (b) forward detection modes. Scale bar: 1 μm. In both images, the narrow distribution of photothermal signals confirms the narrow size distribution expected for single nanoparticles. (III) Dependency on modulation frequency of the photothermal signal in (a) forward and (b) backward detection. At higher modulation frequencies, the photothermal signals in both detection modes are similar, whereas at lower frequencies, the photothermal signal is higher in the forward detection mode. Panels (I–III) are reprinted with permission from the ref 24. Copyright 2006 American Physical Society. (IV) Photothermal microscopy of a mixture of single 10 and 30 nm gold NPs and 100 nm polystyrene beads: (a) in-phase and (b) out-of-phase signal using a single laser beam and (c) PHI signal using separate pump and probe beams. In the in-phase image, a constant background and strong scattering by polystyrene beads are visible. In the out-of-phase image, there is a minor leakage from the strongly scattering objects whereas in the photothermal image using two separate laser beams, the signal-to-noise is about 1 order of magnitude better than with a single laser beam. Reprinted with permission from ref 26. Copyright 2014 AIP Publishing.

than in the backward one. Despite having lower signal-to-noise ratio at lower frequency, the backward detection mode is easier to implement and does not require an additional microscope objective.

Photothermal Microscopy Using a Single Laser Beam. Selmke *et al.*[26] demonstrated that photothermal microscopy could be implemented with a single laser beam instead of two separate laser beams in the PHI configuration. The implementation of a single laser has the advantage that it does not require an additional laser and does not depend on careful overlapping pump and probe beams. A single modulated laser beam acted as both pump and probe fields. The interference occurred between the scattered probe field by the thermal lens and the transmitted probe field. The interference signal was detected by a lock-in amplifier. The out-of-phase component of the lock-in signal signified the presence of an absorbing object. Although this method provided a good contrast to absorbing objects among strong scatterers, its signal-to-noise ratio was at least an order of magnitude lower compared to that of the PHI method using two separate beams, as shown in Figure 3IV. The use of a single laser source removes the main advantage of PHI, *i.e.*, the possibility to choose the probe wavelength in a non- or weakly absorbing region of the objects to detect and thereby to reduce photon noise by increasing the excitation power almost arbitrarily.

Basic Theory of Photothermal Detection. In standard photothermal detection, a nano-object is heated with a modulated pump beam. The object acts as a point-like heat source, which generates a modulated refractive index profile in its surroundings. This profile, in turn, scatters the field of a continuous-wave probe beam in a modulated manner, and this modulation is detected with the lock-in amplifier. In the simple theory described hereafter, we consider a spherical object embedded in a homogeneous medium, and we assume its size to be much smaller than the optical wavelength. If the object is illuminated with a heating laser modulated with frequency Ω, the power absorbed by the nanoparticle is modulated as $P_{abs}(1 + \cos(\Omega t))$. P_{abs} is the mean power absorbed by the nanoparticle, $P_{abs} = \sigma_{abs} \times I_{heat}$ (σ_{abs} is the absorption cross section and I_{heat} is the heating laser's mean intensity), and t is the time. The temperature increase due to the heating can be derived using the heat diffusion theory.[91]

$$\Delta T(r, t) = \frac{P_{abs}}{4\pi\kappa r}\left[1 + \exp\left(-\frac{r}{r_{th}}\right)\cos\left(\Omega t - \frac{r}{r_{th}}\right)\right] \quad (1)$$

where $\Delta T(r,t)$ is the temperature increase at a distance r from the particle's center and at time t. r_{th} is the thermal diffusion length, the characteristic decay length of heat waves at frequency Ω, defined as $r_{th} = \sqrt{(2\kappa/C\Omega)}$, where κ is the thermal conductivity and C is the volume-specific heat capacity of the medium. The temperature profile creates a refractive index profile surrounding the nanoparticle as $\Delta n(r,t) = (dn/dT) \times \Delta T(r,t)$, where dn/dT is the thermorefractive coefficient of the medium.

In the past two decades, several theoretical models have been developed to describe the origin of the photothermal signal. A recent article by Selmke *et al.*[92] nicely summarizes reviews of all these theories; we describe some of these hereafter.

Theory of Scattering from a Fluctuating Environment. The theoretical model developed by Berciaud *et al.*[24] was based

https://dx.doi.org/10.1021/acsnano.0c07638
ACS Nano 2020, 14, 16414–16445

on the theory of light scattering from a fluctuating medium. The change of refractive index induces fluctuations of the medium's susceptibility, which is related to its refractive index by $\Delta\chi = 2n(dn/dT)\Delta T$, where n is the unperturbed refractive index. A plane-wave approximation of the probe beam is considered in the focal plane, although the probe beam is highly focused on the nanoparticle using a high NA objective in standard PHI microscopy. In the high-frequency regime, the thermal diffusion length or the size of the thermal lens is much smaller than the diffraction limit of the probe beam, and therefore, the plane-wave approximation is valid. The interaction of the incident probe field with the susceptibility fluctuation of the medium surrounding the nanoparticle gives rise to the local polarization variation $\Delta P(r,t)$:

$$\Delta P(r, t) = \frac{\epsilon_0 \Delta\chi(r, t)}{n^2} E_i(r, t) \tag{2}$$

where $E_i(r,t)$ is the electric field of the incident probe beam. The scattered far-field can be derived using the Hertz potential,[93] which obeys the inhomogeneous wave equation with the local polarization variation as a source term. The details of the theoretical description are given in the article by Berciaud *et al.*[24] In summary, they obtained the following analytical expression of the photothermal signal:

$$P(\Omega) = \eta\sqrt{\alpha} P_{probe}\left(2\pi\sqrt{2}\, n\frac{dn}{dt}\frac{1}{C\lambda^2\omega_0}P_{abs}\right) f(\Omega) \tag{3}$$

where η is the detection efficiency of the optical system, α is the reflection coefficient for the backward detection mode (or the transmission coefficient for the forward detection mode), P_{probe} and λ are the power and the wavelength of the probe beam, respectively, and ω_0 is the probe beam waist or radius. $f(\Omega)$ is a complex function of frequency and is related to the thermal diffusion length and the modulation frequency of the heating beam. At higher frequency, as the thermal diffusion length is smaller than the probe beam size, the function $f(\Omega)$ is inversely proportional to the modulation frequency and thus the photothermal signal decreases as $1/\Omega$.

Equivalent Dipole Theory. Following the above theory, Orrit's group proposed a similar expression[40,94] purely based on the interferometric mechanism of the scattered field by a thermal lens which can be approximated as that of an equivalent dipole. As discussed above, the refractive index of the medium surrounding a nanoparticle is modulated with the modulation frequency of the heating beam. This refractive index profile acts as a thermal nanolens. The probe beam which is used to detect the thermal lens is scattered by the thermal lens. The scattered probe field $E_{scat}(t)$ interferes with the reference probe field E_{ref} (*i.e.*, the reflected probe beam in the backward configuration or the transmitted probe beam in the forward configuration). The detected intensity I_{det} is therefore

$$I_{det} = |E_{ref} + E_{scat}|^2 \tag{4}$$

For a smaller nanoparticle, the field scattered by the nanoparticle is neglected and only the interference term $2Re[E_{ref} \times E_{scat}(t)]$ (modulated at the same frequency as the heating beam) is filtered out by the lock-in amplifier. For a larger nanoparticle, the static field scattered by the nanoparticle may act as an additional reference field. In addition, for larger nanoparticles, the modulated field scattered by the particle itself would interfere with the field scattered by the thermal lens. Considering the nanoparticle as very small, the photothermal signal (S) is proportional to the field scattered by the thermal lens in an effective volume V where the refractive index is modulated. The field scattered by the thermal lens can be approximated as that of an equivalent dipole $|p| \approx 2n\Delta nV|E_{probe}|$, where ΔnV stands for the volume integral of the refractive index profile. The scattered field by the dipole is

$$|E_{scat}| \approx \frac{1}{4\pi\varepsilon_0\omega_0\lambda^2}|p| \tag{5}$$

Thus, the photothermal signal can be written as an optical power

$$S \approx \frac{1}{\pi\omega_0} n\frac{dn}{dt}\frac{1}{C\lambda^2\Omega}\frac{\sigma_{abs}}{A}P_{heat}P_{probe}\Delta t \tag{6}$$

where A is the diffraction-limited area of the heating beam and Δt is the integration time of the lock-in. Note that eq 6 is similar to eq 3, except for eq 3 containing the complex function of frequency $f(\Omega)$, which is proportional to $1/\Omega$ at high frequency. Assuming an ideal detector and shot-noise-limited detection, the signal-to-noise ratio of the photothermal signal can be written as

$$\mathrm{SNR} \approx \frac{1}{\pi\omega_0} n\frac{dn}{dt}\frac{1}{C\lambda^2\Omega}\frac{\sigma_{abs}}{A}\sqrt{\frac{P_{probe}\Delta t}{h\nu}} \tag{7}$$

where $h\nu$ is the photon energy of the probe beam. This analytical form of the photothermal SNR is very useful for optimizing the photothermal signal. The analytical form describes the dependence of the photothermal SNR on the various parameters, and their relationship provides a control to obtain the detection limit of a photothermal microscopy setup. Later in this review, we will describe the practicality of the analytical form which several articles[27,94−96] used for experimental demonstrations, reaching the detection limit and leading to single-molecule imaging,[22] even at a low heating beam intensity.[23]

Nanolens Diffraction Theory. The most accurate theory of the photothermal contrast was developed by Selmke *et al.*[25,97] who considered the focused laser beams (no plane-wave approximation) and predicted the two-lobed (positive and negative) detection volume of the photothermal signal. They considered a steady-state temperature profile $\Delta T(r)$ (for a modulation frequency below 1 MHz, depending on the thermal conductivity and the heat capacity of the liquid medium). The temperature around the heated nanoparticle decays with the inverse distance. This temperature profile would create the refractive index profile $n(r)$ as indicated below:

$$T(r) = T_0 + \Delta T\frac{R}{r} \tag{8}$$

$$n(r) = n_0 + \frac{dn}{dT}\Delta T(r) = n_0 + \Delta n\frac{R}{r} \tag{9}$$

where R is the particle radius, T_0 is the unperturbed ambient temperature, and n_0 is the unperturbed refractive index of the medium. Although the refractive index profile extends to an infinite distance, at $r = 2R$, the refractive index perturbation decays to half of its maximum and acts as a nanoscopic thermal lens. Considering the heating intensity profile at the particle position $I_h(z_p)$, the change of refractive index Δn can be written as follows:

https://dx.doi.org/10.1021/acsnano.0c07638
ACS Nano 2020, 14, 16414−16445

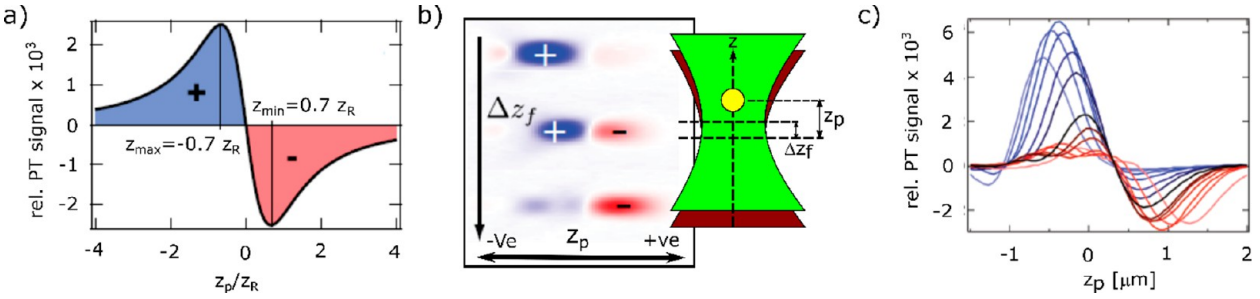

Figure 4. (a) Relative photothermal signal z_p scan predicted by nanolens diffraction theory for an on-axis detection; *i.e.*, the detection angle is close to zero ($\theta = 0$). The laser offset $\Delta z_f = 0$ resulting in a symmetric two-lobed pattern. The radius of the particle is $R = 10$ nm. Adapted with permission from ref 97. Copyright 2012 The Optical Society (OSA). (b) Photothermal signal z_x scan for different Δz_f offsets for a gold nanoparticle with a radius of $R = 30$ nm in a polymer medium (polydimethylsiloxane). Adapted with permission from ref 99. Copyright 2013 Dr. Markus Selmke. (c) Photothermal signal z_p scan for different Δz_f offsets (different colors) for a gold nanoparticle with a radius of $R = 30$ nm in polydimethylsiloxane. Adapted from ref 25. Copyright 2012 American Chemical Society.

$$\Delta n = \frac{\sigma_{abs} I_h(z_p, \Delta z_f)}{4\pi\kappa R}\left(\frac{dn}{dt}\right) = \frac{\sigma_{abs} I_{0,h}}{4\pi\kappa R}\left(\frac{dn}{dt}\right)\frac{1}{1 + \frac{(z_p - \Delta z_f)^2}{z^2_{R,h}}} \tag{10}$$

with

$$I_h(z_p) = \frac{I_{0,h}}{1 + \frac{(z_p - \Delta z_f)^2}{z^2_{R,h}}} \tag{11}$$

where z_p is the particle position relative to the focal plane of the probe beam, Δz_f is the offset of the heating beam relative to the probe beam, $z_{R,h}$ is the Rayleigh distance and $I_{0,h}$ is the peak intensity of the heating beam. In previous theories, a plane-wave approximation was assumed and such an axially dependent intensity profile is an additional feature of this treatment, which made it possible to understand the origin of the photothermal signal more accurately. The probe beam waist at the particle position is $\omega(z_p) = \omega_0[1 + z_p^2/z_R^2]^{1/2}$. Considering an axially symmetric refractive index profile and a steady-state temperature profile, the relative photothermal signal Φ can be derived from the above equation of Δn. The relative photothermal signal is defined as the ratio of the change of intensity in the image plane due to the refractive index profile and the much larger background of the unperturbed field. Note that this relative photothermal signal is independent of probe power. The photothermal signal detected with the numerical aperture of the microscope objective must be integrated over the whole angular detection domain.

$$\Phi(\theta_{min}, \theta_{max}, z_p) = F \times 2\pi \int_{\theta_{min}}^{\theta_{max}} \Phi(\theta, z_p)\sin(\theta)\cos^{-3}(\theta)d\theta \tag{12}$$

where

$$F = \frac{2z_R^2}{\pi\omega_0^2}\left[\exp\left(-\frac{2\tan^2(\theta_{min})z_R^2}{\omega_0^2}\right) - \exp\left(-\frac{2\tan^2(\theta_{max})z_R^2}{\omega_0^2}\right)\right]^{-1} \tag{13}$$

and

$$\Phi(\theta, z_p) = \exp\left(\frac{-\kappa^2\tan^2(\theta)Re(\Omega^{-1})}{2}\right)\left[\exp(2R\Delta n k_0 \arg(\Omega))\left|\Gamma(1 + iR\Delta n k_0)_1 F_1\left(-iR\Delta n k_0, 1, \frac{\kappa^2\tan^2(\theta)}{4\Omega}\right)\right|^2 - 1\right] \tag{14}$$

where ${}_1F_1$ denotes the confluent hypergeometric function of the first kind. The theory predicts that the photothermal focal volume is a two-lobed pattern, including positive and negative detection volumes. The two-lobed pattern depends on the offset between the two beams (Δz_f). The z_p scan shows a dispersion-like behavior indicating that the thermal lens acts as a diverging lens. Figure 4a shows the dispersion behavior predicted by the theory, and Figure 4b,c shows the experimental proof of the theoretical prediction. Selmke *et al.*[25,92,97−100] explored different treatments and found similarities in a common outcome that the photothermal detection volume is dispersion-like. The magnitude and the sign of the photothermal signal depend on the axial shift of the particle position and of the heating beam focus relative to the probe beam focus. We refer to the Ph.D. thesis of Markus Selmke[99] for detailed overview of those theories.

Advantages. One of the major advantages of photothermal microscopy is the possibility to choose a probe wavelength far away from the absorption bands of the object of interest, so that the probe absorption is negligible. The complementarity of the probe and heating beams is a powerful tool, which can be exploited in several ways. An additional degree of freedom is the choice of the heating wavelength. As photothermal contrast is completely different in nature from fluorescence, correlated photothermal and fluorescence microscopy images can be recorded simultaneously and are often complementary.

(1) The poor spatial resolution of the excitation beam of IR or mid-IR spectroscopy can be improved by the implementation of photothermal microscopy.[59] The higher spatial resolution is achieved by the much lower diffraction limit of the visible probe beam.

(2) Circular dichroism is a property of a chiral object, which is defined as the difference between the absorption of left and right circularly polarized light. The polarization state of the

https://dx.doi.org/10.1021/acsnano.0c07638
ACS Nano 2020, 14, 16414−16445

spherical waves in the focal plane is quite complex and difficult to control. However, spatial resolution would be dramatically degraded in a plane wave or with a spherical wave with a very low NA. By separating polarization and resolution requirements on the heating and probe beams, photothermal microscopy combines excellent polarization control with a high spatial resolution.[101]

(3) The detection volume of the photothermal signal is by nature a two-lobed dispersion-like profile with positive and negative signals[25] and can be exploited to study the slow diffusional behavior in the axial direction on a length scale below the diffraction limit. Twin-focus photothermal correlation spectroscopy can be used to measure drift induced by radiation pressure, as demonstrated by Selmke *et al.*[102]

(4) Some endogenous organelles such as mitochondria and lysosomes absorb visible light. Thus, photothermal microscopy enables label-free imaging in living cells, which is a great advantage for understanding complex heterogeneous structure and dynamics in cells.[47]

(5) Single-molecule fluorescence methods are limited to relatively few fluorescent dye molecules with high quantum yields. Photothermal microscopy is a promising technique to detect weakly or nonfluorescent organic and inorganic molecules. Gold nanoparticles, for example, have very low photoluminescence quantum yield but large absorption cross sections and high photostability. Being biocompatible, gold nanoparticles are very useful labels for imaging in biology.

(6) Simultaneous measurements of absorption and luminescence of a single nanoparticle provide a direct measurement of their luminescence quantum yield[103−105] on a single-particle level and allows one to disentangle radiative and nonradiative processes. Correlated microscopy is very useful for the investigation of complex multiphoton energy transfer processes in multichromophoric systems such as conjugated polymers[23] and dye nanoparticles.[104]

DETECTION LIMITS OF PHOTOTHERMAL MICROSCOPY AND SINGLE-MOLECULE SENSITIVITY

Photothermal detection schemes rely on the time-modulated refractive index change of the medium around an absorber heated by a pump laser. Signal contrast is generated by probing this refractive index gradient by another probe laser beam outside the absorption spectrum. The sensitivity of any detection is usually quantified by the signal-to-noise ratio of the method and is given by eq 7 for photothermal microscopy.[94] The photothermal signal strength and SNR depend upon many factors, including heating laser power, probe laser power, integration time, modulation frequency, overlap of the heated region with the probe beam, and thermal conduction properties of the transducing medium,[94] specifically its thermorefractive coefficient (dn/dT).[27,95,96] The SNR can be optimized by careful adjustment of each of the parameters, notably the probe and heating powers, the integration time of the lock-in detector, as well as an informed choice of the transducing medium. Below, we discuss the influence of each of these parameters on photothermal signals.

Heating Source. Most photothermal microscopes use CW lasers for heating. Probing absorption with tunable wavelengths or in unconventional spectral ranges, however, may require pulsed sources. Yorulmaz *et al.*[28] did a comparative study using a CW laser and a pulsed laser as pump beam sources and found no significant difference in either lateral and axial spatial resolution or in signal-to-noise ratio. Figure 5 shows

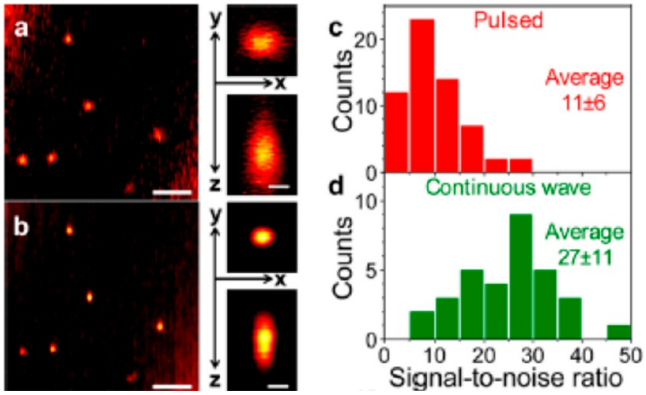

Figure 5. Photothermal microscopy using pulsed and CW lasers as heating beam sources. (a) Photothermal image of 20 nm gold nanospheres using supercontinuum pulsed laser excitation at 532 nm with a heating intensity of 25 kW/cm^2. (b) Same sample area as in (a) but CW laser excitation with a heating intensity of 38 kW/cm^2. Scale bars in both (a) and (b) are 2 μm. Right side of (a) and (b): corresponding lateral and axial profile of photothermal signal of a 20 nm gold nanosphere. Scale bar: 300 nm. Histogram of SNR of photothermal signal of single 20 nm gold nanospheres under (c) pulsed excitation and (d) CW excitation. SNR was normalized by the heating power. Reprinted from ref 28. Copyright 2015 American Chemical Society.

experimental results of single 20 nm gold nanospheres using a supercontinuum pulsed laser (Figure 5a) and using a CW laser (Figure 5b) with the associated photothermal point spread function (PSF) of a single nanoparticle. The larger PSF obtained with the pulsed laser was due to the imperfections of the laser spatial mode (not perfectly TEM_{00}) rather than to pulsed heating. The photothermal SNR using two kinds of excitation is shown in Figure 5c,d. The photothermal SNR using the pulsed laser was about 2.5 times lower than that using a CW laser with a same average power. This reduction in SNR was likely due to the overall reduced heating in 16.67 ns dark periods between pulses of a supercontinuum laser source (Fianium, 60 MHz, 12 ps).

Heating Power. As the photothermal signal arises from the change of refractive index surrounding a nanoparticle via the heat dissipation, the photothermal signal is proportional to the heating intensity. Gaiduk *et al.*[22] observed a linear power dependence for a 20 nm gold nanoparticle, shown in Figure 6d. Boyer *et al.*[21] and Berciaud *et al.*[36] observed similar power dependence for a 5 nm gold nanoparticle up to 20 MW/cm^2. The maximum allowed heating power is usually limited by the photophysical properties of the object of interest, notably optical saturation or bleaching for molecules and reshaping or melting for metal particles. This value is very high for gold nanoparticles. For gold nanospheres, the maximum heating power is essentially limited by the melting of gold.[106,107] The bulk melting temperature of gold is 1300 K. For a 20 nm gold nanosphere, the heating power for melting is about 20 mW in a focused spot and the melting power scales with the inverse square of the particle size. However, for applications in soft matter and in biological systems, the maximum allowed heating power is limited to much lower values by boiling of the surrounding liquids or by thermal damage to the biomolecules, for example, protein denaturation.

Probe Power. The photothermal signal scales linearly with probe power, whereas the SNR scales with its square root (eq 7). Gaiduk *et al.*[22] reported the linear probe power dependence

https://dx.doi.org/10.1021/acsnano.0c07638
ACS Nano 2020, 14, 16414−16445

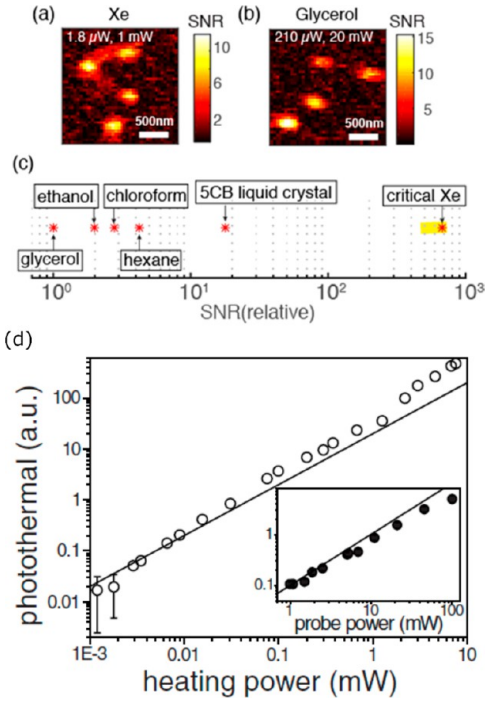

Figure 6. Photothermal images of 5 nm gold nanoparticles in (a) near-critical xenon and (b) glycerol. The heating and probe powers are mentioned. (c) Relative (with regard to glycerol) photothermal signal-to-noise ratio in near-critical xenon (Xe) is compared with other organic solvents and 5CB liquid crystal. The data for the organic solvents are taken from ref 94, and the data for the 5CB liquid crystal taken from refs 27 and 96. Organic solvents such as chloroform, hexane, pentane, and toluene provide a photothermal SNR much higher than that of water or even than that of glycerol because of their low boiling points and the ensuing higher values of their thermorefractive coefficients. The liquid crystal 5CB and critical xenon provide photothermal SNR more than 1 order of magnitude and 2 orders of magnitude, respectively, larger than that of glycerol. (d) Linear power dependence of the photothermal signal with the heating and probe powers. The measurements were performed on a single 20 nm gold nanosphere in glycerol. The solid lines are the linear fits for low powers. The error bars indicate standard deviations. For most data, the error bars are smaller than the symbol size. The linear power dependence of heating and probe beams allows optimization of photothermal signals by tuning the laser powers. The left (a–c) and right (d) figures are adapted with permission from the refs 95 and ref 22, respectively. Copyright 2016 American Chemical Society and copyright 2010 The American Association for the Advancement of Science, respectively.

for 20 nm gold nanoparticles over 2 orders of magnitude in probe power, as shown in Figure 6d. The probe wavelength is typically chosen outside the absorption spectrum or within the far tail end of the spectrum, so that the absorption of the probe beam is very weak relative to that of the heating beam. Therefore, the probe power can be increased considerably, typically to more than 100 times larger than the heating power. The maximum probe power is often limited by the available laser power only and sometimes by the residual absorption of the nanoparticle.

Modulation Frequency of the Heating Laser. When the thermal diffusion length (r_{th}) is larger than the diffraction-limited spot size of the probe beam, the photothermal signal is independent of the modulation frequency. When the thermal diffusion length is smaller than the probe beam spot size, the photothermal signal is inversely proportional to the modulation frequency.[20,36] The thermal diffusion length depends not only on the modulation frequency but also on the thermal conductivity and specific heat of the surrounding medium as $r_{th} = \sqrt{(2\kappa/C\Omega)}$.

Thermal Isolation. The thermal conductivity of a typical organic liquid is smaller than that of the sample substrate, which is typically glass. Therefore, the glass in photothermal measurements can act as a heat sink and reduce the photothermal signal. Gaiduk *et al.*[94] found that addition of a thin (~100 nm) poly(methyl methacrylate) (PMMA) layer on top of the glass enhances the photothermal signal by about a factor of 2.

Integration Time of the Lock-in Amplifier. The photothermal SNR scales as the square root of the lock-in integration time. To improve SNR, the lock-in integration time can be arbitrarily increased unless the objects under study are not photostable. The maximum allowed integration time is only limited by the dwell time and the (photo-) stability of the nano-objects under study.

Thermorefractive Coefficient (d*n*/d*T*). The choice of a proper transduction medium can circumvent the use of high heating powers, which could inflict photoinduced damage. Media with high thermorefractive coefficients will thus extend photothermal detection to species with smaller absorption cross sections and/or lower photodamage thresholds. Gaiduk *et al.*[94] reported a 5-fold increase in SNR using pentane as a medium compared to glycerol for the detection of 20 nm gold nanospheres. The increased sensitivity enabled the detection of dissipated powers as low as 3 nW from 20 nm gold nanospheres using a low heating beam power of 1 μW, with a SNR of 8 and 10 ms integration time.[94] The thermotropic liquid crystal 5CB (4-cyano-4-*n*-pentylbiphenyl) medium was used to enhance photothermal signals due to the large temperature sensitivity of its refractive index. Chang *et al.*[27] imaged 20 nm gold nanoparticles in two different media, 5CB and glycerol, keeping a constant probe power of 4.2 mW and compared the heating powers required to attain a similar SNR (78 ± 19 for 5CB and 86 ± 32 for glycerol). They found an enhancement factor of 20 in the case of 5CB compared to glycerol. Photothermal imaging near the nematic-to-isotropic phase transition temperature (33.3°C) of 5CB showed further enhancement in the SNR due to a steep increase in thermorefractive coefficient (d*n*/d*T*).[27,96] A 40-fold enhancement of SNR for gold nanoparticles was achieved at the transition temperature of 5CB compared to water[96] at the cost of a long equilibration time for the liquid crystal. Monitoring photothermal signals over a range of temperatures also allowed for detection of the phase transition.[96] A comparison of photothermal SNR for different transducing media is presented in Figure 6c. Near the critical point of xenon (T_c = 16.583 °C, P_c = 5.842 MPa), a large SNR enhancement factor of 440 ± 130 was achieved compared to that of glycerol.[95] Gold nanoparticles with 5 nm diameter could be detected with a SNR of 9.4 at only 1.8 μW of heating power and 60 μW of probe power, which is 117 times and 20 times less power, respectively, than that in glycerol (see Figure 6a,b). The large enhancement is due to the extremely large d*n*/d*T* value near the critical point[95] but also to the relatively short relaxation time of the simple atomic fluid xenon compared to the more complex molecular fluid 5CB. It is also important to realize that, in order to take full benefit of the near-critical

https://dx.doi.org/10.1021/acsnano.0c07638
ACS Nano 2020, 14, 16414–16445

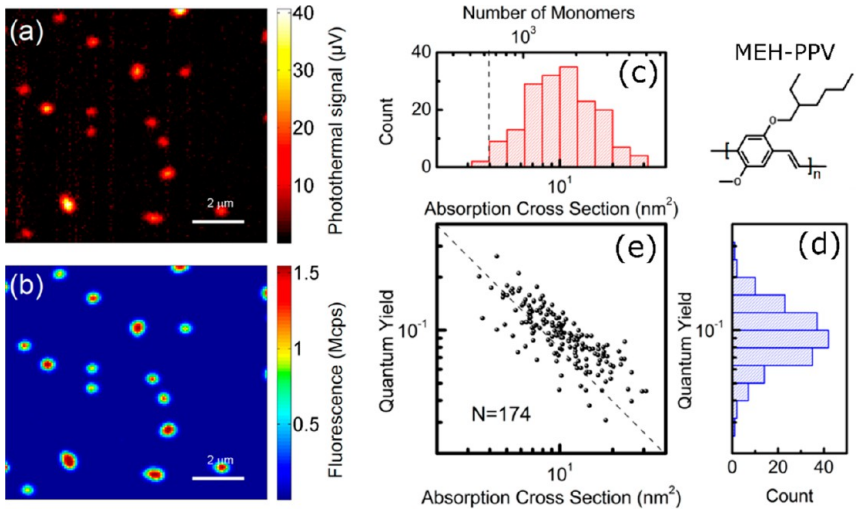

Figure 7. Simultaneous (a) absorption and (b) fluorescence images of single conjugated polymers MEH-PPV embedded in PMMA in near-critical xenon. (c) Histogram of absorption cross section and number of monomers of single MEH-PPV molecules. The dashed line is the photothermal detection limit. (d) Histogram of quantum yields of single MEH-PPV molecules deduced from the simultaneous measurements of fluorescence and photothermal signals of many single MEH-PPV molecules. (e) Correlation plot of quantum yields and absorption cross sections of single MEH-PPV molecules. The dashed line with a slope of −1 indicating the inverse relationship. Adapted from ref 23. Copyright 2017 American Chemical Society.

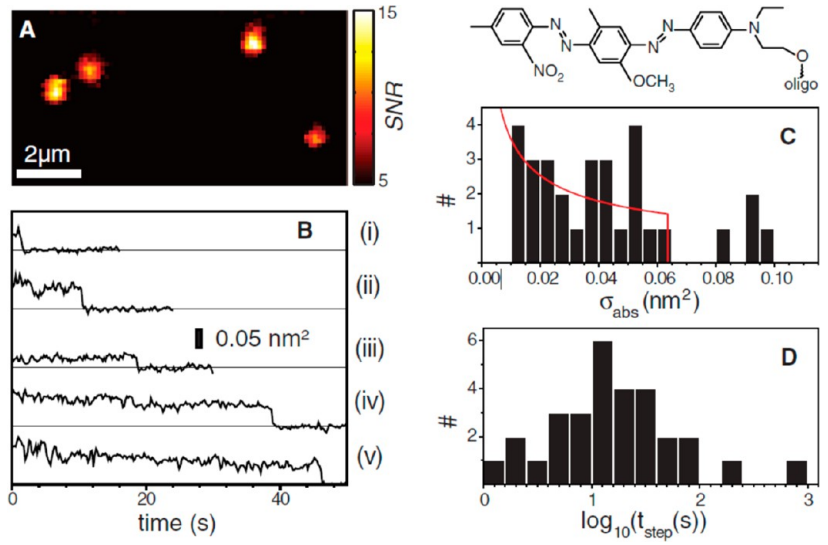

Figure 8. (A) Photothermal image of four constructs (BHQ1-10T-BHQ1) in nitrogen-bubbled glycerol, each consisting of two BHQ1 molecules and one single strand of DNA with 10 thymine (T) bases. (B) Photothermal time traces of single BHQ1-10T-BHQ1 in an aerated environment showing single-step photobleaching. (C) Histogram of the change of absorption cross sections calculated from 30 one-step bleaching events. The average cross section is 0.041 nm². The solid red line represents the distribution of absorption cross sections of single chromophores considering an isotropic distribution of transition dipole moments. Top: Chemical structure of a BHQ1 molecule. (D) Histogram of survival times before single step bleaching in aerated environment. The average survival time is 49 s. Reprinted with permission from ref 22. Copyright 2010 The American Association for the Advancement of Science.

enhancement, the whole thermal lens should be near-critical. This condition can only be realized for weakly absorbing objects, so that the temperature gradient does not bring the surrounding fluid too far away from its critical temperature.

This exceptional improvement in SNR was then exploited to simultaneously measure the photothermal contrast and fluorescence of single conjugated polymer molecules of MEH-PPV (poly[2-methoxy-5-(2-ethylhexyloxy)-1,4-phenylenevinylene]) in a PMMA matrix using near-critical xenon,[23] as shown in Figure 7. The use of low pump and probe laser powers enabled simultaneous absorption and emission measurements which were impossible previously due to very fast photobleaching of MEH-PPV molecules under the high irradiance necessary for measurable heating. The number of monomers and the quantum yield of single polymer chains was determined by estimating the absorption cross section from the photothermal signal. These results displayed an inverse correlation between the quantum yield and the absorption cross section of single MEH-PPV polymer chains, where these quantities were measured simultaneously. The inverse relationship indicates that larger MEH-PPV polymer chains have more fluorescence quenching pathways which lower their fluorescence quantum yield. Further, monitoring photothermal and fluorescence time traces revealed that fluorescence and

https://dx.doi.org/10.1021/acsnano.0c07638
ACS Nano 2020, 14, 16414−16445

absorption of MEH-PPV have different bleaching behaviors. Absorption decays slower than fluorescence with illumination time. This indicates photoinduced quenching processes in conjugated polymers. Simultaneous fluorescence and absorption measurements of single conjugated polymer chains thus provided a detailed insight into energy transfer processes and quenching mechanism in a direct manner, which was mostly unavailable from fluorescence measurements alone.

Single-Molecule Detection. The photothermal detection sensitivity can be optimized to reach the single-molecule detection limit. Gaiduk *et al.*[22] demonstrated photothermal imaging of single photoresistant dye molecules BHQ (black hole quencher). BHQ molecules have very low quantum yield and thus a high nonradiative relaxation rate which produces a strong photothermal signal and a very high optical saturation intensity. The latter property makes it possible to use higher heating powers and to get a better photothermal signal. Single BHQ–DNA constructs (BHQ1-10T-BHQ1) were imaged in glycerol with 514 nm heating and 800 nm probe lasers with SNR ∼ 10 and an integration time per pixel of 300 ms, as shown in Figure 8A. Photothermal time traces of single BHQ1–DNA constructs showed single-step photobleaching, as shown in Figure 8B, signifying that the signal arises from only one molecule. From the single-step photobleachings, the absorption cross sections and the bleaching times are calculated and are shown in Figure 8C,D, respectively. The average bleaching time at the powers used and in an oxygenated environment was found to be 49 s (Figure 8D). The average absorption cross section of a single construct bearing two chromophores was estimated to be approximately 4 Å^2 (shown in Figure 8C), which corresponds to the extinction coefficient and confirms that the signal originates from a single chromophore.

Single-molecule sensitivity at room temperature was also achieved (i) through sensitive monitoring of the absorption by ground-state depletion microscopy[9] and (ii) through monitoring of the extinction by direct transmission measurements without modulation.[14,15] Similar to photothermal microscopy, ground-state depletion microscopy also uses a nonlinear ($\chi^{(3)}$) signal from pump and probe lasers but both are in resonance with energy levels of the absorbing species. The pump laser depletes the ground-state population, resulting in an intensity change of the incident probe beam detected in a transmission geometry, thereby giving rise to the contrast. Single Atto647N dyes were detected with shot-noise-limited sensitivity. Presence of blinking and single-step photobleaching in the simultaneously acquired fluorescence image confirmed the presence of a single molecule. Ground-state depletion is closely related to photothermal imaging: both methods make use of the cross-talk between two beams of different colors and detect a weak probe intensity change under modulation of a pump beam. As ground-state depletion is an electronic effect and involves short-lived states, it can be modulated at higher frequencies than photothermal contrast. In practice, however, it requires pulsed lasers for pump and probe, which are costlier than the CW lasers used in photothermal detection.

Sandoghdar and co-workers[14,15] also detected the absorption of single dye molecules at room temperature, similar to standard bulk extinction measurements. They measured the dip in the transmission of the incident beam passing through the sample by comparing it to a reference beam. The contrast was generated by the difference in intensities of the probe and reference beam owing to the presence or absence of a molecule in the focus while the sample was scanned. The background signal was minimized by complete index matching by a careful choice of substrate and medium and using a balanced photodiode detector. They demonstrated detection of single Atto647N and terrylene diimide dyes embedded in PMMA and covered by a polyvinyl alcohol layer, respectively. This extinction measured through bright-field scattering is very general and is of the iSCAT-type. However, it requires careful subtraction of background and compensation of noise in the detection, and without previous knowledge of the nano-objects under study, it cannot readily distinguish extinction due to absorption from extinction due to scattering.

The three techniques for room-temperature detection of single-molecule's absorption described here were reported independently in the same year, 2010. Although all of these methods showed promising results of single-molecule detection, they require very high laser powers for pump and probe beams, which may lead to photodamage when imaging living cells.

We discuss here some ideas and perspectives to improve photothermal microscopy for low heating or excitation powers. Indeed, using a near-critical fluid such as xenon or CO_2 (which has very similar critical temperature and pressure to Xe) as a transducing medium, one can improve considerably the photothermal signal-to-noise ratio at lower laser powers. However, Xe or CO_2 media are not ideal for biological applications. The main difficulty in photothermal imaging of biological samples arises from the unfortunately weak value of the thermorefractive coefficient of water at room temperature ($dn/dT \sim 9 \times 10^{-5}$). This low value is related to the density maximum of water at 4 °C. Moreover, the heating power must be kept very low, so that living cells and biological materials are not damaged by the increase in temperature. Looking at eq 7, there are not many probe parameters to optimize for cellular imaging. Photothermally active probes should be weakly or nonfluorescent, thus presenting low luminescence yields, and they should be highly photostable and their absorption cross section should be as high as possible. Noble metal nanoparticles have very high absorption cross section and very weak quantum yield. Among metal nanoparticles, gold nanoparticles are considered to be biocompatible particularly at low concentrations; however, some studies report toxicity of gold nanoparticles.[108,109] We envisage that smaller gold nanoparticles (below 5 nm in size) would be more biocompatible due to their diffusion ability through the membrane and, with the right functionalization, probably with PEG or polyelectrolyte ligands[108,110] instead of CTAB or citrate ligands.

The absorption cross section of a nanoabsorber can be improved beyond that of single organic dye molecules in extended π-conjugated systems (as proposed in ref 111) consisting of several chromophores, such as organic nanoparticles[104] or conjugated polymers,[23] which can be as small as few nanometers in their compact conformation. The absorption cross section might also be enhanced using plasmon enhancement,[111] for example, in the hot spot between two nanoparticles. However, such constructs are usually much larger than large single molecules.

PHOTOTHERMAL CORRELATION SPECTROSCOPY AND SINGLE-PARTICLE ABSORPTION SPECTROSCOPY

Photothermal Correlation Spectroscopy. Correlation spectroscopy is based on the detection of fluctuations of an

https://dx.doi.org/10.1021/acsnano.0c07638
ACS Nano 2020, 14, 16414–16445

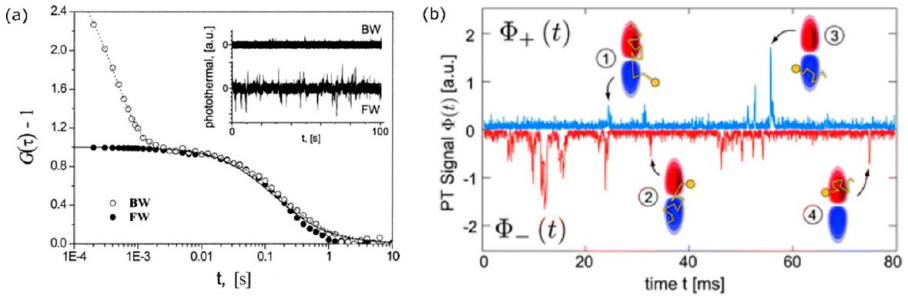

Figure 9. (a) Photothermal correlation spectroscopy of 80 nm gold nanoparticles in 1:1 water/glycerol mixture. A comparison between the forward (FW) and backward (BW) detection modes: compared to the forward detection mode, an additional fast component appears in the backward detection mode. The fast component arises from the frequent changes of phase of the signal due to random variations of the distance between the scattering thermal lens and the reflection on the liquid−glass interface taken as reference. The inset shows the photothermal time traces in both detection modes. In the forward detection modes, negative signals arise in addition to positive signals. Adapted from ref 40. Copyright 2009 American Chemical Society. (b) Photothermal time traces of twin-focus photothermal correlation spectroscopy of diffusing gold nanoparticles. The positive and negative photothermal signals come from positive and negative parts of the phase-sensitive photothermal detection volume. Measurements were performed in the forward detection mode. Adapted with permission from ref 102. Copyright 2013 RSC Publishing.

emitter's fluorescence signal, usually from organic dyes, inside the fluorescence detection volume of the laser focus, and is called fluorescence correlation spectroscopy (FCS). FCS has provided an enormous wealth of information regarding molecular photophysics and dynamics in various environments.[112] However, FCS is limited to highly fluorescent molecules. The photothermal detection of gold nanoparticles[20,36] has allowed correlation spectroscopy to be carried out by monitoring fluctuations of absorption signals.[40,41,102,113]

Paulo *et al.*[40] studied photothermal correlation spectroscopy of gold nanoparticles diffusing in solution in two different detection geometries: (a) forward and (b) backward detection modes and found distinctive features in their correlation curves, as shown in Figure 9a. In the backward mode, the phase mismatch between the scattered and reflected reference fields contributes an additional short component in the correlation curve, which is not present in the forward detection mode, for which the forward scattered field is always in phase with the transmitted reference field. The backward detection mode was useful to study diffusion in confined spaces in the length scale of a half-wavelength. These authors also studied the diffusion of bacteriophage viruses labeled with streptavidin-coated 20 nm gold nanoparticles. The measurements revealed clear differences in the diffusion times of free nanoparticles and those of labeled nanoparticles, thus revealing the potentiality of photothermal correlation spectroscopy. Lounis and co-workers[113] employed similar photothermal correlation spectroscopy to evaluate the hydrodynamic radius of gold nanoparticle−protein conjugates. They also demonstrated the insensitivity of photothermal correlation spectroscopy toward scattering background by performing measurements in the presence of strongly scattering latex beads with minimal effect on the correlation curves.[113] The effect of the temperature increase on the Brownian motion of the particle diffusion was also elucidated by varying the heating laser power.[41] The diffusion time showed a gradual decrease with increasing heating laser power due to decrease in local viscosity around the particle. Selmke *et al.*[102] developed twin-focus photothermal correlation spectroscopy based on their findings of the thermal lensing effect, which creates a dispersive signal along the optical axis separating a positive and negative photothermal focal volume.[25] Similar to the backward-scattering geometry discussed previously, the twin detection lobes give very good axial sensitivity, enabling measurements of the motion perpendicular to the focal plane at subdiffraction length scales. The dynamical processes within the detection volume, their time scales, and velocities could be extracted from the autocorrelation and cross-correlation of the signals from the two opposite detection lobes. Whenever a particle moves from one lobe to the other, there is a switch in the sign of the photothermal signal as shown in Figure 9b, the cross-correlation of which allows precise determination of particle's movement direction. Velocities of gold nanoparticles down to 10 nm ms^{-1} were detected, which was far superior in resolution to fluorescence correlation spectroscopy techniques.[102]

Single-Particle Absorption Spectroscopy. Extinction arises from the addition of absorption and scattering, which can be very strong for metal nanoparticles. Access to pure absorption spectra, free from contributions from scattering provides valuable insight into the optical properties of single nanoparticles. This information is very important for many applications. Photothermal imaging can be performed with tunable continuous wave[37,39,90] or pulsed[28,114−116] heating sources. Spectral scanning of the heating source provides the spectra of pure absorption of single nanoparticles.

Lounis and co-workers employed a CW-tunable dye laser and a Ti:sapphire laser as heating beams in their photothermal heterodyne imaging technique to record pure absorption spectra of gold nanoparticles,[39] of CdSe/ZnS semiconductor nanocrystals,[90] and of single-walled carbon nanotubes (SWNTs),[37] albeit in a relatively narrow spectral range. The absorption spectra of gold nanoparticles with various sizes (5−33 nm) clearly showed that the surface plasmon resonance (SPR) blue shifts with decreasing size, which matches well with predictions of the Mie theory,[39] as shown in Figure 10a. This shift was accompanied by concomitant spectral broadening with decreasing particle size, as shown in Figure 10b. This trend stems from contributions from both the interband transition of gold and the increase in electron-surface scattering as the size decreases, which favors loss of coherence of the collective oscillations of the electrons. A decrease in plasmon dephasing time from 5.9 fs was found for 33 nm nanoparticles down to 4.1 fs for 5 nm nanoparticles which, though larger than those calculated from ensemble measurements, clearly shows the intrinsic size effect on spectral

https://dx.doi.org/10.1021/acsnano.0c07638
ACS Nano 2020, 14, 16414−16445

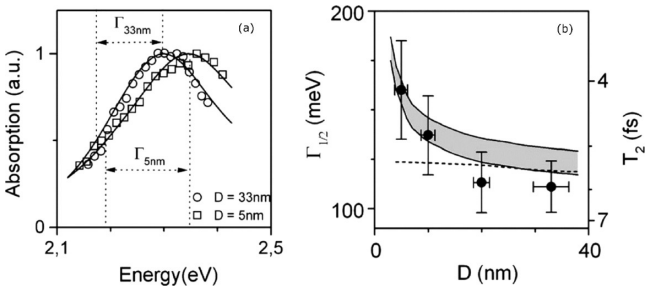

Figure 10. (a) Photothermal absorption spectra of single 5 and 33 nm gold nanoparticles. The full width at half-maximum (Γ) is shown in the inset. The solid lines are simulations using the Mie theory considering a size-dependent modification for the bulk dielectric constant of gold. (b) Size-dependent surface plasmon width. The solid circles with error bars are experimental data. The dashed and solid lines are simulations of the Mie theory without and with considering size-dependent corrections, respectively. The gray area accounts for the uncertainties in the bulk dielectric function of gold given in ref 117. Adapted with permission from ref 118. Copyright 2006 Royal Society of Chemistry.

features. Dispersions in SPR energy were attributed to a slight ellipticity of the nanoparticles which were oriented randomly with respect to the polarization axis of the linearly polarized excitation laser.[39]

CdSe/Zns semiconductor nanocrystals were also detected at room temperature using PHI utilizing their nonradiative Auger relaxation processes to heat up the medium.[90] Photothermal images of single nanocrystals showed the complete absence of the blinking, which characterizes the emission of single semiconductor nanocrystals. This makes photothermal tracking of such nanoparticles more viable for imaging applications due to the larger stability of their absorption. Single-particle absorption spectra were recorded at high CW excitation, which showed an absorption blue-shifted from luminescence, with peaks at 2.16 and 2.17 eV corresponding to biexciton and trion formation. The homogeneous line widths of the absorption spectra, similar to the luminescence spectra, were found to be narrower than their ensemble measurements.[90] Absorption spectra of metallic and semiconductor SWNTs were also studied by means of PHI and compared to single-particle luminescence spectra of the same particles, revealing intrinsic optical properties[37] All of these studies were limited by the narrow spectral range of the excitation source.

Link and co-workers[28] developed a broadband spectroscopic technique for measuring pure absorption spectra by replacing the fixed wavelength narrow band laser with a tunable white-light heating beam in a typical photothermal setup, as shown in Figure 11a,b. This covered the visible and near-infrared spectral region, thus enabling observation of multiple spectral features of absorbing metal nanoparticles. Absorption spectra were measured by selecting single wavelengths from the white-light laser by an acousto-optic tunable filter. They also incorporated a simple internal calibration strategy (Figure 11c–e) to get rid of chromatic aberration and any discrepancies in power and obtained absorption spectra of gold nanoparticles and gold nanorods with excellent agreement with finite-difference time domain (FDTD) simulated spectra. Measurement of this nonradiative spectral feature enabled monitoring of the blue shift of the absorption spectra that is predicted by the numerical simulations. The amount of shift increased with decreasing aspect ratio of gold nanorods due to intrinsic damping by interband transitions, thus creating larger mismatch between scattering and absorption maxima. The difference in line shape of gold nanorods was also evident, where the transverse plasmon mode is clearly visible in the absorption spectra in contrast to the scattering spectra where it is very weak or not present at all.[28]

Further, photothermal absorption of single hybrid bimetallic nanostructures such as platinum (Pt)-decorated gold nanorods showed spectral broadening and red-shifted resonances compared to those with bare gold nanorods.[115] This revealed that the line shape broadening of the extinction of such structures in ensemble measurements is not solely due to

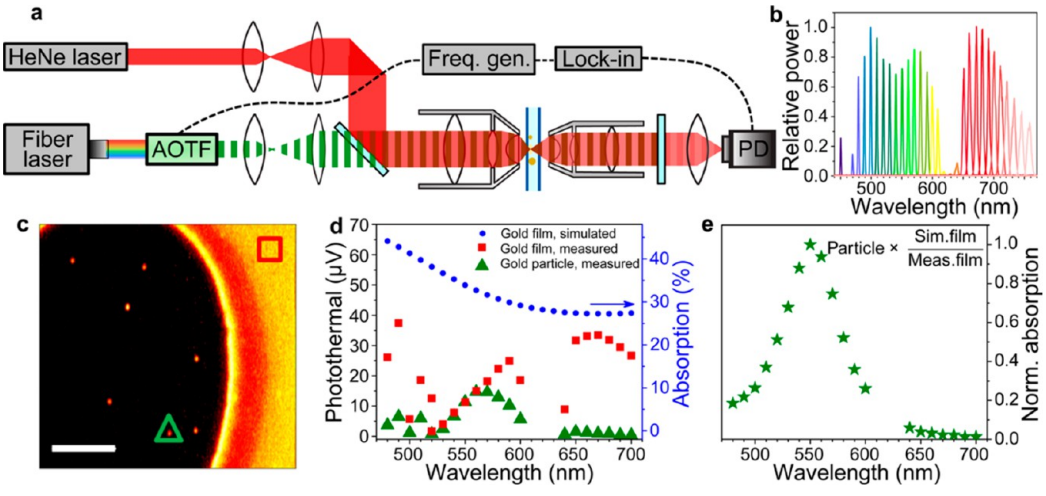

Figure 11. (a) Schematic of photothermal microscopy in the forward detection mode (transmission mode). For broadband spectroscopy, a broadband fiber laser source equipped with acousto-optic-tunable filter (AOTF) was used. (b) Relative laser powers at different wavelengths selected by the AOTF. (c) Photothermal image of 50 nm gold nanoparticles (round spots) and of a 15 nm thick gold film (uniform signal area in the right side). (d) Photothermal signal *vs* wavelength for a single gold nanoparticle (green solid triangles, marked also in (c)), thin gold film (red solid squares, marked also in (c)), and the theoretical prediction (blue solid circles) using FDTD simulation. (e) Corrected absorption spectra of the same gold nanoparticle as in (d). The correction is done by normalizing with the ratio of simulated and measured absorption spectra of the thin gold film. Adapted from ref 28. Copyright 2015 American Chemical Society.

https://dx.doi.org/10.1021/acsnano.0c07638
ACS Nano 2020, 14, 16414–16445

particle heterogeneity but also to intrinsic damping caused by the Pt coating. FDTD simulations confirmed that line shape changes after Pt deposition result from coupling between Au and Pt in the hybrid nanostructure.[115] Photothermal imaging and spectroscopy coupled with dark-field scattering has also been used to distinguish radiative and nonradiative properties of individual Fano clusters. Yorulmaz *et al.*[116] studied the absorption spectrum of individual gold plasmonic nanoparticle decamers, prepared by electron beam lithography. Each decamer consists of a central disk surrounded by nine smaller disks, as shown in Figure 12. Unlike scattering spectra, which

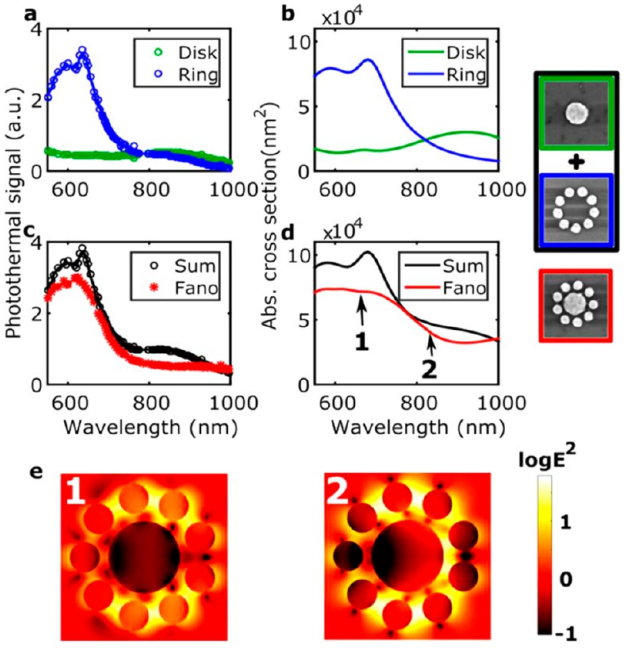

Figure 12. (a) Absorption spectra measured experimentally of a single central disk (green) and of a single outer ring (blue). Simulated absorption spectra are shown in (b). (c) Sum (black) of the spectra measured for the central disk and the outer ring compared to the absorption spectrum measured for a single Fano cluster (red). Simulated spectra are shown in (d). SEM images of the nanostructures with corresponding line colors of the spectra in (a–d). The size of each SEM image is 500 nm × 500 nm. (e) Electric field intensity maps of a single Fano cluster calculated at positions 1 (left) and 2 (right) as marked in (d) corresponding to the blue Fano peak and the Fano dip, respectively. Reprinted from ref 116. Copyright 2016 American Chemical Society.

had an asymmetric line shape due to Fano resonances, absorption spectra showed only a symmetric line shape. This difference between the absorption and scattering spectra was predicted theoretically, but observed experimentally thanks to photothermal microscopy. Measuring the absorption spectra of constituent components' outer rings of smaller disk and central larger disk revealed that the absorption spectra of the Fano cluster is largely dominated by the signal from the outer ring.[116]

We discuss here some perspectives to photothermal correlation spectroscopy and single-particle absorption spectroscopy. Dual-focus fluorescence correlation spectroscopy (2fFCS) was shown to be superior to single-focus fluorescence correlation spectroscopy for a quantitative determination of diffusion coefficients. Indeed, 2fFCS removes such artifacts of FCS as optical saturation, refractive index variations, and focus distortions due to index mismatch between the medium and immersion oil.[119] In standard FCS, the quantitative determination of diffusion coefficient is difficult because the detection volume depends on experimental conditions such as solvent refractive index. To measure the diffusion coefficient quantitatively, an external ruler is needed. In 2fFCS, two overlapping laser foci with precisely known and fixed distance between them allow the quantitative determination of the diffusion coefficient by measuring the autocorrelation of fluorescence signals of each detection volume and also the cross-correlation of fluorescence signals from the two detection volumes. Twin-focus photothermal correlation spectroscopy brings similar advantages in addition to unlimited measurement time. Photothermal interference contrast (PIC) microscopy can also be configured for dual-focus photothermal correlation spectroscopy. In PIC, when the heating beam is positioned exactly in the middle of the two spots of the probe beam separated by the distance of 1.2 μm, the photothermal detection focal volume is two-lobed dispersion-like with positive and negative signals.[20] Thus, a photothermal signal would change sign when a nanoparticle diffuses from one detection volume to other one. Similar to twin-focus photothermal correlation spectroscopy, the cross-correlation of signals arising from the two detection volumes would provide information about diffusion coefficients. However, this will allow to measure diffusion beyond the diffraction limit and thus very slow diffusion.

Although photothermal absorption spectroscopy was applied to single semiconducting nanocrystals, it required high excitation laser intensities at which semiconducting nanocrystals stopped fluorescing. Simultaneous measurement of absorption and fluorescence spectra is important for understanding the energy transfer processes in single-photon emitting nanocrystals. A similar restriction also exists for multichromophoric systems such as conjugated polymers, where investigations of radiative and nonradiative energy transfer processes between different chromophores foster a better understanding of their interactions. Conjugated polymers show conformation-dependent optical properties depending on the intra- and interchromophoric interactions. Simultaneous measurements[23] of absorption and fluorescence spectra of such complex systems would allow a direct investigation of intra- and intermolecular interactions.

MID-IR PHOTOTHERMAL IMAGING, SUPER-RESOLUTION PHOTOTHERMAL IMAGING, AND WIDE-FIELD PHOTOTHERMAL MICROSCOPY

Mid-IR Photothermal Imaging. In this section, we focus on recent advances in mid-IR photothermal microscopy. IR spectroscopy provides a characteristic fingerprint for identifying and characterizing chemical specimens. However, far-field imaging in the IR is hampered by its poor spatial resolution. With diffraction-limited imaging, the best spatial resolution of IR imaging would be several microns, which is too coarse for applications in nanoscience and in biology. In photothermal microscopy, the PSF is the product of the PSFs of the heating and of the probe beam, neglecting the spread of the modulated temperature profile, which can be made very small at high modulation frequencies. Therefore, even for a very broad heating beam, the PSF may be diffraction-limited by the probe beam wavelength. The probe wavelength is conveniently chosen in the visible, far from any absorption band of the sample. Mid-IR photothermal microscopy takes benefit from

https://dx.doi.org/10.1021/acsnano.0c07638
ACS Nano 2020, 14, 16414–16445

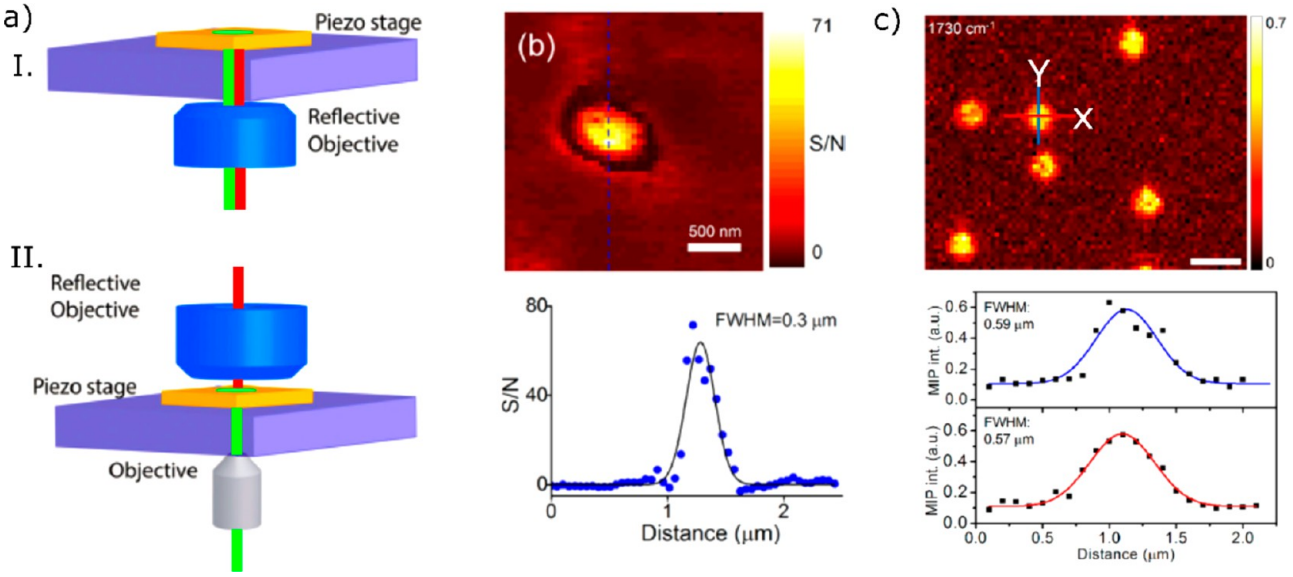

Figure 13. Co-propagating (I) and counter-propagating (II) configurations of mid-IR photothermal microscopy. In the co-propagating scheme, the pump beam (red) and the probe beam (green) propagate in the same direction, whereas the pump and probe beams counter-propagate in the counter-propagation scheme. Adapted with permission from ref 120. Copyright 2020 Royal Society of Chemistry. (b) Mid-IR photothermal imaging of a 100 nm polystyrene bead (top) and the line profile (bottom) along the dashed line shown at the top. The full width at half-maximum (fwhm) is 300 nm. Adapted from ref 62. Copyright 2017 American Chemical Society. (c) Mid-IR photothermal imaging of 500 nm PMMA beads (top) and horizontal (red) and vertical (blue) line profiles (bottom). The fwhm along *X* and *Y* directions were 590 and 570 nm, respectively. The deconvolution of the image spot with the particle size resulted in a fwhm of about 290 nm. Scale bar: 1 μm. Adapted with from ref 68. Copyright 2019 American Chemical Society.

the spectral resolution of the mid-IR and of the spatial resolution in the visible region. Depending on the wavelength of the probe and the focusing objective, the spatial resolution obtained is well below 1 μm, representing a considerable improvement on direct IR microscopy. Mid-IR photothermal microscopy can be implemented in two configurations—co-propagating and counter-propagating, as shown in Figure 13a. In the co-propagating configuration, both pump and probe beams propagate in the same direction along the same path, whereas they propagate in opposite directions in the counter-propagating configuration. Although the co-propagating configuration has the advantage of requiring a single microscope objective, this configuration is limited to the use of a reflective objective whose maximum NA can reach up to 0.8 only (usual refractive objectives cannot be used for mid-IR light). In addition, IR refractive objectives usually suffer from severe chromatic aberrations. In the counter-propagating configuration, the detection path is separated from the excitation path and thus, the choice of microscope objective for detection is independent of that for excitation. In the detection, a high NA (up to NA of 1.5) refractive objective can be used, which is also advantageous for avoiding chromatic aberrations. Thus, a spatial resolution for the counter-propagating configuration better than that of the co-propagating one is obtained.

Lee *et al.*[65] reported mid-IR photothermal imaging under the very general term "nonlinear IR microscopy". They used ∼1 μm size water droplets dispersed in balsam oil to demonstrate the spatial resolution improvement with a modulating mid-IR pump beam and a CW probe beam at 786 nm. They achieved a spatial resolution of 1.1 μm which was close to the diffraction limit of the probe beam (∼λ/2NA, with NA = 0.55). This was a more than 3-fold improvement upon the diffraction-limited spatial resolution of the mid-IR beam (λ = 3.5 μm, NA = 0.5). Cheng's group[63] demonstrated mid-IR photothermal imaging with a spatial resolution of 650 nm using co-propagating configuration with a detection objective NA of 0.65 and a probe wavelength of 785 nm. Mid-IR photothermal imaging came into the limelight when Hartland's group[62] demonstrated IR imaging of a 100 nm polystyrene bead with a spatial resolution of 300 nm (as shown in Figure 13b), a 1 order of magnitude improvement upon the diffraction limit of the mid-IR beam. They took advantage of the counter-propagating configuration with a high NA refractive objective (NA = 0.9) and a probe beam at 532 nm. In a more recent paper, Li *et al.*[68] demonstrated mid-IR photothermal imaging of 500 nm PMMA beads with a spatial resolution of 290 nm, after deconvolution of an image spot size of 590 nm with the particle size, as displayed in Figure 13c. They used a probe beam of wavelength 532 nm and a high NA refractive objective (NA = 1.2). This is an improvement by about a factor two compared to their previous measurements on 500 nm PMMA beads using a 785 nm probe beam and a dark-field condenser with a maximum NA of 0.5. Mid-IR photothermal imaging has shown tremendous potential for applications in imaging biological systems. One of these applications is the ability to do depth-resolved imaging in a PC-3 prostate cancer cell, as demonstrated by Zhang *et al.*[59]

Bai *et al.*[61] recently demonstrated mid-IR wide-field photothermal imaging in contrast to the above-mentioned scanning-based methods. They set up a virtual lock-in camera, *i.e.*, a camera whose frame rates were synchronized with the pump and probe beam pulses so that the temporal resolution of the photothermal signal was determined by the probe pulse width. They could image a wide-field area of about 100 × 100 μm^2 with a frame rate of 1250 frames/s and a signal-to-noise ratio of about 2. The diffraction-limited spatial resolution was about 510 nm. It is worth discussing the time response briefly

https://dx.doi.org/10.1021/acsnano.0c07638
ACS Nano 2020, 14, 16414−16445

here. Usual scanning-based lock-in photothermal methods use high modulation frequencies, typically around 1 MHz. Standard cameras are not fast enough to capture image changes at such a high frequencies. To detect photothermal signals, Cheng's group[61,121] used pulsed pump and probe lasers whose pulses were synchronized and delivered heating and probe pulses with precise control of the time delay. Hot and cold images were recorded by summing eight sequences of probe pulses, alternately with and without heating. The difference of the two images recorded at the camera rate of 1250 frame/s provided the photothermal image. Slowly varying drifts and noises were subtracted, in effect producing a virtual lock-in detection for the wide-field image. The heating pulse triggered a MCT (HgCdTe) detector, which triggered the probe pulse. The heating beam was modulated by a chopper, and the camera acquired the images. The time delays between the pump and probe pulses were controlled electronically and the camera allowed a frequency division to obtain certain frame rates, for example, 1250 frame/s rates (f/8) from a 20 kHz trigger frequency. Similar work was reported independently and simultaneously by the Ideguchi group,[122,123] and a detailed comparative discussion has appeared in a recent paper from the Cheng group.[121] The schematic of the experimental setup and the principle of the virtual lock-in detection are shown in Figure 14a,b. The above-mentioned wide-field photothermal microscopy used pulsed pump and probe beams, however the same technique could also be realized with modulated CW pump and probe lasers.

Super-resolution Photothermal Microscopy. In conventional photothermal microscopy, imaging beyond the diffraction limit is possible thanks to the nonlinearity of the photothermal signal[124] not only because of the reduced PSF[94] but also owing to nonlinearities in the medium's response to heating. In particular, nanobubble formation around an overheated nano-object at elevated heating powers presents a threshold in heating power, *i.e.*, a very nonlinear behavior. Super-resolution images can be obtained by subtracting a linear PT signal from the nonlinear PT signal. The nonlinear signal increases with the nanobubble size, which varies nonlinearly with heating power. At low heating power, the photothermal signal depends almost linearly on the laser power until the boiling threshold is reached. For a Gaussian heating beam profile, the maximum power is in the center of the beam. Thus, if the heating power at the center of the beam just exceeds the boiling threshold for a given nanoparticle, moving the particle a fraction of the PSF away from the center will suppress the bubble signal. The bubble signal therefore appears on a much reduced area around the maximum. The spatial resolution is thus enhanced beyond the diffraction limit, as schematically demonstrated in Figure 15. Nedosekin *et al.*[124] demonstrated nonlinear photothermal image of a cluster of 90 nm gold nanospheres with a spatial resolution down to 50 nm, as shown in Figure 15e. However, the size dispersity of gold nanoparticles leads to a strong variation in threshold when moving from particle to particle. Moreover, the use of high laser powers in the nonlinear microscopy is a strong limitation for applications to biological samples, even though most of the heating remains localized very close to the particle. Similar to photothermal therapy,[125−127] nonlinear photothermal microscopy through bubble formation can be applied to the cancer treatment through damage induced by the localized heating and by the localized mechanical disruption occurring upon nanobubble formation and collapse.[69]

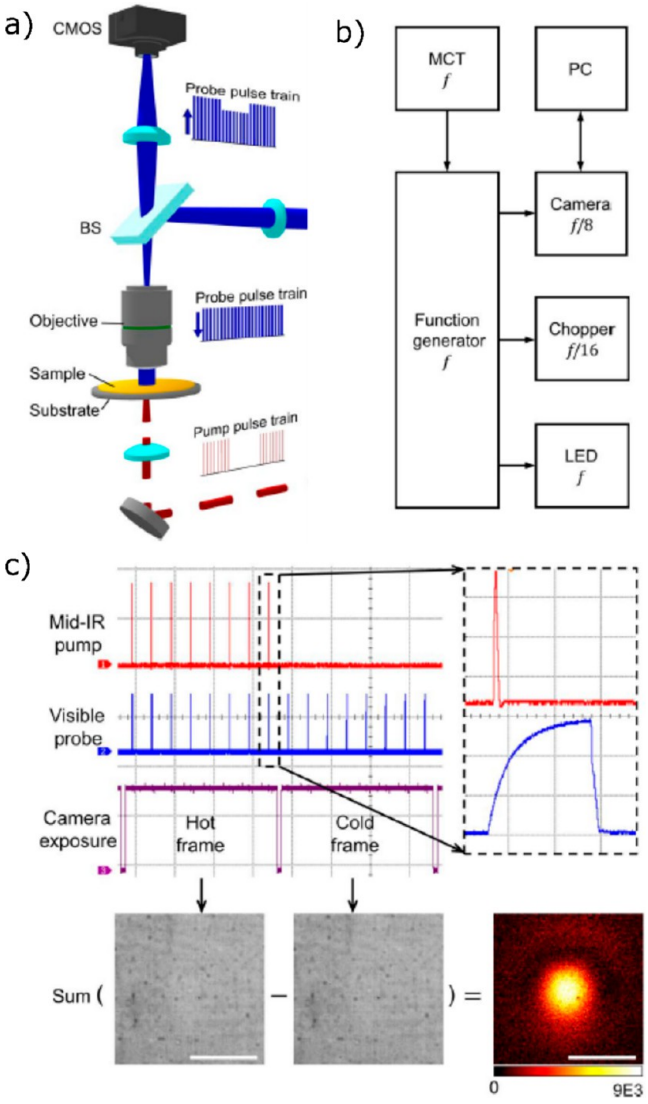

Figure 14. (a) Schematic representation of the wide-field photothermal setup using the virtual lock-in camera. Pump (red) and probe (blue) pulses propagate in a counter-propagating way. (b) Block diagram showing triggering controls in the virtual lock-in detection. (c) Pump (red) and probe (blue) pulses and camera exposure (purple) with zoomed-in part of the pump and probe pulses (each division of the grid is 100 μs in left non-zoomed-in part and 500 ns in the right-zoomed-in part). Bottom: Image subtraction of the cold frame from the hot frame to obtain a photothermal image. Scale bars: 40 μm. Adapted with permission from ref 61. Copyright 2019 American Association for the Advancement of Science.

A nonlinear photothermal microscope was based on the detection of the photothermal signal at twice the modulation frequency f of the heating beam. This method improved the spatial resolution beyond the diffraction limit, as reported by Kobayashi's group.[128−130] The nonlinear signal, however, was significantly lower (a few tens of times lower) than the standard PHI signal. To obtain a good signal-to-noise ratio, a high excitation power was required, which is a serious disadvantage for cell imaging.

Wide-Field Photothermal Microscopy. Some 10 years ago already, Absil *et al.*[131] proposed a heterodyne holographic method for wide-field photothermal imaging at a camera rate of 16 Hz and with an integration time of 5 s. They obtained

https://dx.doi.org/10.1021/acsnano.0c07638
ACS Nano 2020, 14, 16414−16445

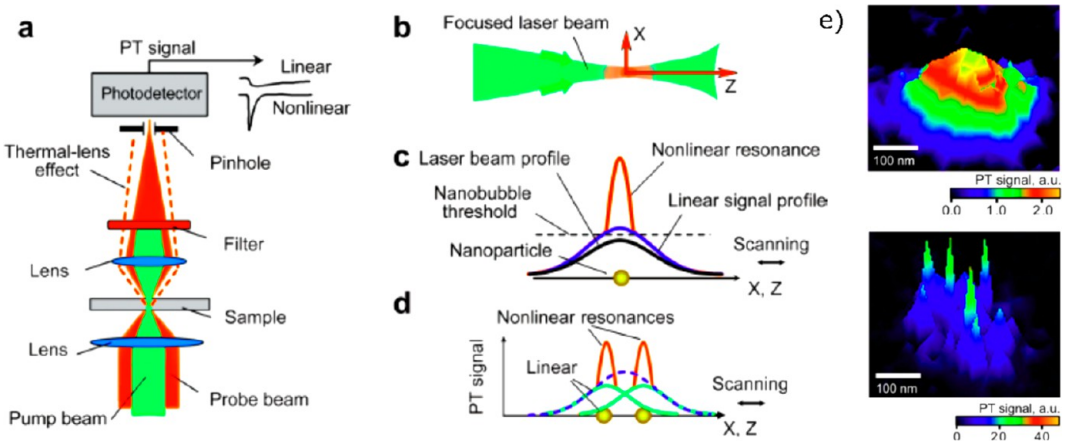

Figure 15. (a) General scheme for nonlinear super-resolution photothermal microscopy. (b) Scheme of a focused beam. (c) Scheme showing nonlinear signal amplification when the particle is placed at the center of the heating laser spot. (d) Separation of the nonlinear signals from two nanoparticles separated by a distance smaller than the diffraction limit of a Gaussian beam (the dashed blue line represents the sum of linear signals from two nanoparticles). (e) Linear (top) and nonlinear (bottom) photothermal images of a cluster containing several 90 nm gold nanospheres. Adapted with permission from ref 124. Copyright 2014 John Wiley and Sons.

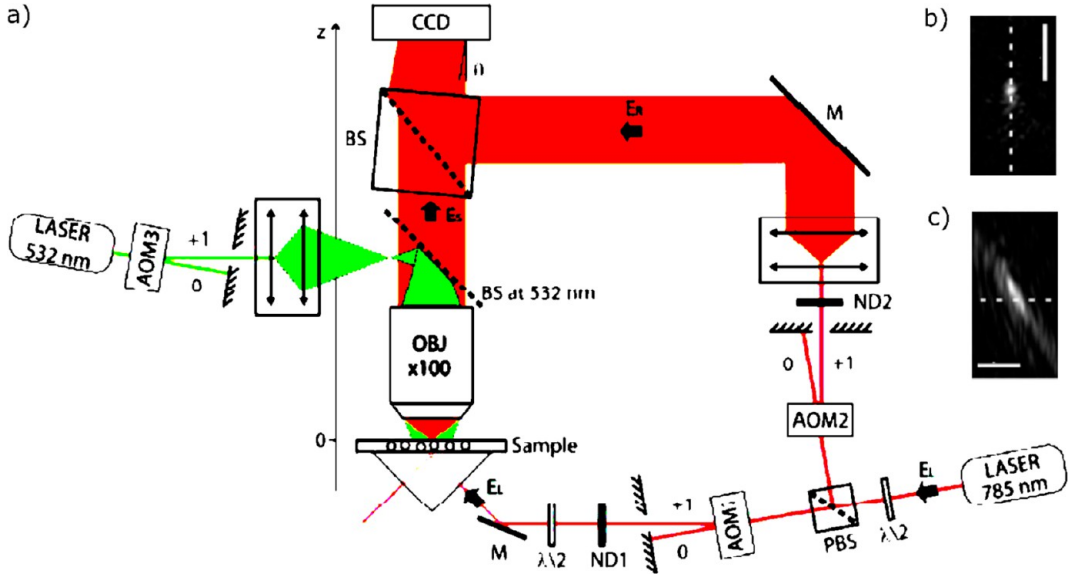

Figure 16. (a) Schematic of the experimental setup for the photothermal heterodyne holography method. (b) Photothermal holography image of a 10 nm gold nanosphere in the $x-y$ plane. (c) Reconstruction of the same hologram as in (b) along the same dotted line in the $x-z$ plane. Scale bars in (b) and (c) are both 5 μm. Adapted with permission from ref 131. Copyright 2010 The Optical Society (OSA).

images of single 10 nm gold nanoparticles with a good signal-to-noise ratio. This holographic setup is schematically shown in Figure 16a. A probe beam was split into a reference part and an illumination part similar to other interferometric configurations. These two beams were modulated with two AOMs at two different frequencies, F_{AOM1} and F_{AOM2}, both close to 80 MHz. The illumination part of the beam was sent around a nanoparticle in a total internal reflection geometry. The light scattered by the particle was collected by means of a microscope objective and sent to a camera where the reference part of the probe beam was tilted by 1° to interfere with the scattered beam. The interference beat frequency was therefore $\Delta F = F_{AOM1} - F_{AOM2}$ and was low enough to be synchronized with the comparatively low frame rate of the camera. The holography setup measured the interference fringes at a particular frequency F_{inv} such that $F_{inv} = \Delta F + F_{cam}/k$, where F_{cam} is the camera frame rate and k is an integer ($k = 4$ in the present case). The heating beam was modulated with another AOM at a frequency F_{AOM3} synchronized with the frequency F_{inv}. This holography method was able to reconstruct three-dimensional images from the two-dimensional holography image. The three-dimensional holography image of a single 10 nm gold nanosphere is shown in Figure 16b,c. The holographic method required several AOMs for modulating the laser beams, and in addition, it needed very high laser power for obtaining an image with a good contrast. High excitation power limits the utilizations of the technique. Another disadvantage of this method is the low modulation frequency, which fails to filter out the strong components of the $1/f$ noise at low frequencies.

Turko *et al.*[132] presented wide-field photothermal imaging of gold nanoparticles at video rate (30 Hz) using wide-field interferometric phase microscopy. Instead of a scanning method, they used a camera as a detector for the wide-field

https://dx.doi.org/10.1021/acsnano.0c07638
ACS Nano 2020, 14, 16414−16445

imaging in which the camera frame rate was synchronized with the heating beam modulation, and subsequently, the Fourier analysis of the heating-induced phase shift produced the photothermal image. The imaging speed, however, was limited by the camera frame rate. Lasser's group (Pache *et al.*[133]) demonstrated fast three-dimensional wide-field photothermal imaging in living cells using photothermal optical lock-in optical coherence microscopy (POLI-OCM). They were able to image single 6 nm gold nanopsheres in a living HeLa cell.

Wide-field photothermal imaging would be a considerable improvement on scanning-based confocal imaging in several ways. The rate of acquisition of large images would be enhanced by 1−3 orders of magnitude, thereby making simultaneous imaging of many particles possible. As a consequence, wide-field photothermal imaging would enable fast tracking of several single particles or molecules to obtain time-dependent correlations on their movements and dynamical processes. Such information is crucial to understanding interactions and collective effects in complex systems such as living cells. An example of simultaneous spatial and temporal correlations is provided by the spatial and temporal heterogeneities found in supercooled liquids near the glass transition temperature.[134,135] Previous work based on molecular fluorescence,[136] however, was limited by fluorescence bleaching, which creates artifacts in the correlation analysis. Wide-field photothermal microscopy could be used to investigate complex glassy dynamics using metallic nanoparticles as probes, giving access to unlimited measurement times.[134]

The current demonstrations of wide-field photothermal detection lag far behind the sensitivity and SNR of confocal measurements. The most likely explanation is their low modulation frequency, limited by camera video rates, which makes these measurements prone to strong components of the $1/f$ noise. Therefore, there is still a need for further developments of wide-field photothermal microscopy with 100 kHz to 10 MHz modulation frequencies. The sensitivity and modulation rate of wide-field photothermal imaging will certainly be improved by advanced ultrafast cameras,[137] which allow very fast imaging speed of greater than 10^5 frame/s. Recently, innovative approaches toward a lock-in camera were proposed, based on advanced camera technology[138] or based on fast optical modulation of the polarization.[139] Lock-in cameras are based on the principle of each pixel demodulating the modulated signal similar to the lock-in amplifier. Therefore, lock-in cameras produce instantaneously amplitude and phase images. Panigrahi *et al.*[139] proposed a polarization-based demodulation technique to obtain amplitude and phase information on a high-frequency (tens of kHz) modulated signal from a single acquisition of a camera image. The use of an electro-optic modulator and polarizing optical elements in a proper configuration creates four quadrature channels in a single recorded frame by an ordinary camera, and the careful image subtraction of these channels produces the final amplitude image.

Super-resolution microscopy[140,141] based on localizations of single-molecule fluorescence has shown great promise in biological applications. The basic principle is based on switching a fluorescence signal on and off and localizing the position by fitting with a Gaussian function when the fluorescence is on. Among various single-molecule fluorescence localization methods, we envisage that the idea of PAINT[142] (point accumulation for imaging in nanoscale topography) or DNA-PAINT[143−145] can be implemented in photothermal microscopy to obtain super-resolution images. In PAINT, diffusing fluorescent molecules stochastically interacts with the sample (binding and unbinding), which results in switching the fluorescence signal on and off. For implementation of PAINT in photothermal microscopy, one needs to choose gold nanoparticles labeled with specific ligands, instead of fluorescent molecules (the absorption cross sections of gold nanoparticles are few orders of magnitude higher than those of typical fluorescent molecules). Similar to PAINT, stochastic interaction of diffusing gold nanoparticles to the target sample would result in switching the photothermal signal on and off. The localization of gold nanoparticles by the Gaussian fit would produce the super-resolution image. Although the localization accuracy would be limited by the larger size of gold nanoparticles, the major advantage of gold nanoparticles compared to fluorescent molecules is their high photostability. Super-resolution photothermal microscopy based on PAINT would not require an excitation power as high as that required for super-resolution based on nanobubble formation as discussed above. Thus, a photothermal PAINT method would be ideal for super-resolution imaging of biological systems.

APPLICATIONS IN IMAGING AND TRACKING IN BIOLOGICAL SYSTEMS

Optical microscopy, being the least invasive of imaging methods, is the most commonly used method for visualization and investigation of structure and dynamics in living cells and tissues, from single biomolecules to cell organelles. Fluorescence microscopy until now was the most widely used technique in biological imaging. It often utilizes Stokes-shifted emission from organic dyes or from autofluorescent proteins bound to the target of interest. Such fluorescence signals can easily be separated from the scattering background and thus give access to single-molecule sensitivity. However, this method is limited to fluorescent labels and it suffers from the low photostability of most fluorophores, whose blinking and bleaching limit time resolution and monitoring over long acquisition times.

Because it does not rely on fluorescence, photothermal microscopy enables the visualization of absorbing objects such as metallic nanoparticles, weakly or nonfluorescent chromophores, and endogenous biological components in living cells. For example, a variety of endogenous chromoproteins are good optical absorbers and non- or weakly fluorescent and would provide label-free imaging contrast in biological samples. Since the report on photothermal imaging of absorbing metal nanoparticles[20] in 2002, photothermal microscopy was extended to a plethora of biological specimens. These include cytochromes in mitochondria,[47,146] hemoglobin in red blood cells in blood vessels,[48] melanin in skin cancer,[50,128] and brain imaging.[147,148] Biological specimens have also been stained and imaged by means of small (∼5−10 nm) gold nanoparticles as photothermal contrast agents due to their large absorption cross section, stability, and exceptional heating capabilities.[83,149−152] Gold nanoparticles have a very low luminescence quantum yield and thereby most of the energy absorbed upon photoexcitation is released as heat in the surroundings, giving stable photothermal signal over long periods of time. Hereafter, we discuss various applications of photothermal microscopy in biology, covering both the label-free and gold-nanoparticle-tagged systems.

https://dx.doi.org/10.1021/acsnano.0c07638
ACS Nano 2020, 14, 16414−16445

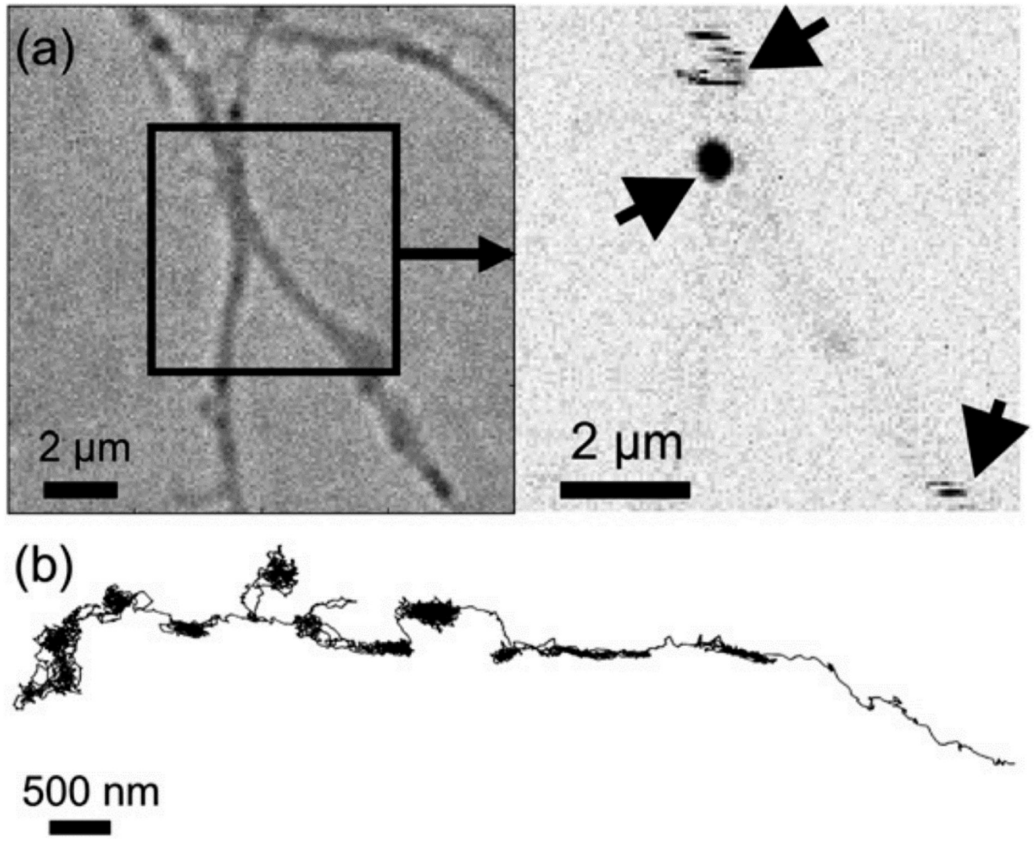

Figure 17. (a) White-light image (left) and photothermal image (right) of a live neuron labeled with gold nanoparticles marked with arrows. A photothermal image of gold nanoparticles shows a nice alignment with the white-light image of the live neuron. The photothermal image shows both solid and stripe patterns. The solid pattern is due to slow, confined diffusion, whereas the striped pattern is due to fast diffusion of the nanoparticle. (b) Trajectory of a 5 nm gold nanoparticle in a live neuron recorded at a video rate, showing the heterogeneity in its diffusion. The particle's movement alternates between slow and fast diffusion. Reprinted with permission from ref 149. Copyright 2006 Elsevier.

Lounis's group extensively studied various biological systems *via* photothermal microscopy using gold nanoparticles as labels. They specifically tagged mGlurR5-myc membrane proteins in COS7 cell using secondary immunostaining *via* anti-IgG 10 nm gold antibodies of membrane protein primarily labeled with antimyc antibodies tagged with Alexa568 dyes.[83] They used photothermal interference contrast microscopy to image single membrane proteins. This modality circumvented major drawbacks of fluorescence detection schemes, such as autofluorescence and scattering from the cellular environment, because the PIC method is sensitive to absorbing objects only. This labeling strategy also enabled the parallel acquisition of scanning fluorescence and PIC images. By a similar labeling method earlier, AMPA receptors tagged with 5 nm gold nanoparticles were tracked on the plasma membrane of live neurons at video rates for long periods of time[149] as shown in Figure 17. In this study, the laser intensities ranged from 200 to 400 kW/cm^2, which is larger than, but comparable to, the intensities used in fluorescence imaging. AMPA receptors were found to reside in diverse environments where they alternate between free and confined diffusion states (Figure 17b). Due to the millisecond integration time, moving receptors appear as stripes in the raster scan image, whereas the immobilized ones appear as diffraction-limited spots (Figure 17a).

The PHI technique was also used to track cellular uptake and movement of 10 nm gold nanoparticles coated with a mixture of 1-mercaptoundecane sulfonic acid and 1-octanethiol inside complex cellular media.[150] The PHI images showed that the majority of the particles reside in the free cytosol space in the central part of the cell surrounding the nucleus. Further, by measuring the photothermal signal fluctuations due to the transit of particles in a fixed laser focal volume, the cytosol viscosity was measured and found to be $\sim 2 \times 10^{-2}$ Pa·s, which is 20 times larger than that of water. PHI microscopy was utilized to visualize and track effector proteins, whose dynamics are pivotal for intercellular communication. Tracking effector protein fibroblast growth factor 2 (FGF2) molecules labeled with gold nanoparticles revealed heterogeneous binding sites of HS (heparan sulfate) chains and heterogeneous movements of individual FGF2 in the pericellular matrix of a living cell.[152] This study revealed that the HS binding sites form local networks that confine the FGF2 leading to slower movement. These networks form paths that allow translocation over long distances, up to several micrometers.

Ultrasmall gold nanoparticles, 5 nm in diameter, being immune to photobleaching and being good photothermal contrast agents, were functionalized with small camelid antibodies, which have a very high binding affinity for green fluorescent proteins (GFPs). These particles are near to ideal probes to track such proteins. This probe was utilized to label surface and intercellular GFP proteins in highly crowded spaces such as adhesion sites and cytoskeletal structures both *in vitro* and in live cells.[151] The PHI image and epi-fluorescence images of GFP exhibited excellent colocalization,

https://dx.doi.org/10.1021/acsnano.0c07638
ACS Nano 2020, 14, 16414−16445

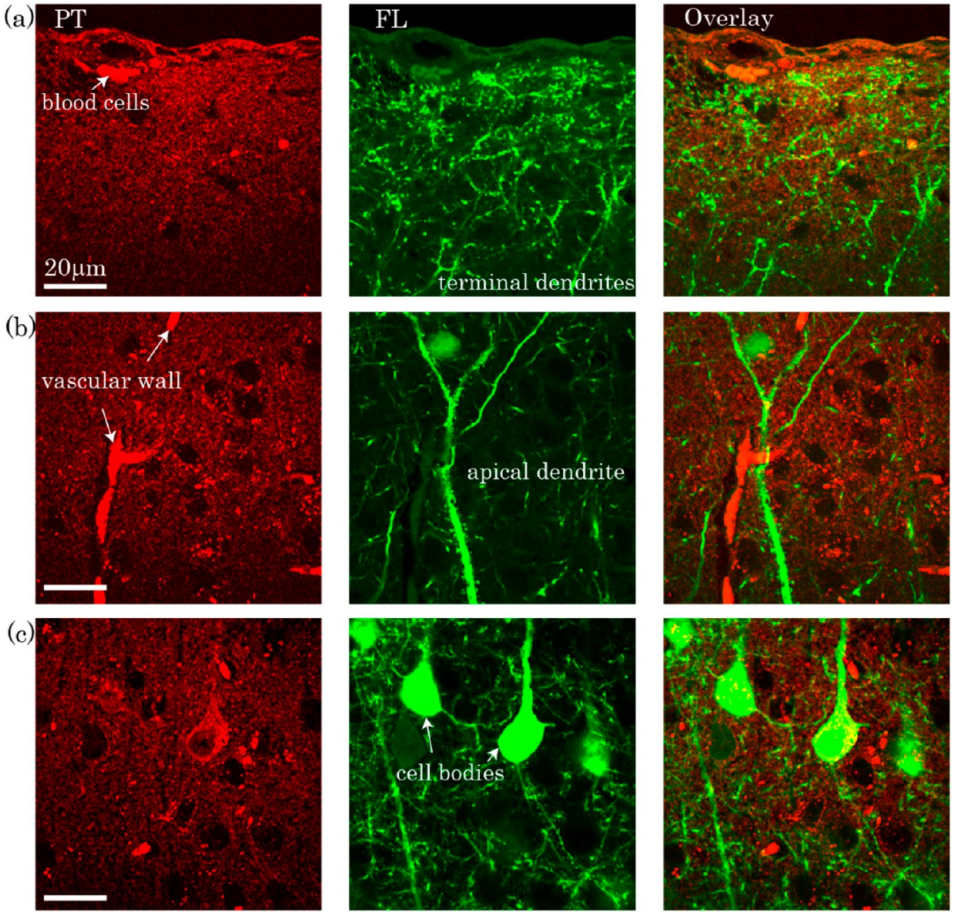

Figure 18. Combined photothermal (left), fluorescence (center) images, and their overlays (right) of different layers of mouse brain cortex at (a) dendrite terminals, (b) dendrite, and (c) blood cells. Both photothermal and fluorescence images represent neurons expressing yellow fluorescent proteins (YFP). Photothermal signals show more distinct structures and organizations producing strong photothermal signal at the red blood cells and vessels probably because they include heme proteins. A Y-shaped vessel is observed in the photothermal image shown in (b) possible due to red blood cells fragmenting and stacking inside the vessels. The pump and probe beam powers were 0.5 and 4 mW, respectively. The image acquisition time was 6 s for an area of 500 × 500 pixels. Reprinted with permission from ref 148. Copyright 2016 The Optical Society (OSA).

which was an indication of the probe's robust specificity in such complex biological systems.

Photothermal microscopy enabled direct imaging of endogenous chromophores without any labels, thereby mitigating any influence an external label could have on the target of interest. Photothermal microscopy was used to image mitochondria, which play a central role in cellular metabolism.[47,146] The origin of the photothermal signal was mainly attributed to visible light absorption by cytochrome *c*, a heme present in mitochondria.[146] Another study showed that cytochrome *c* was not the only source of photothermal signal. Rather, the absorption stems from an ensemble of proteins present near the mitochondrial membrane.[47] Photothermal images showed homogeneous signals with spatial resolution better than that of fluorescence images, where large signal heterogeneity was observed due to variations in dye labeling specificity.

Label-free 3D imaging of biological samples has also been conducted by photothermal microscopy.[50,53,59,148,153] Lu *et al.*[48] used two-photon nonlinear excitation pump to image heme proteins with 3D sectioning in live cells. Compared to one-photon excitation, the heating gradient is much more concentrated along the *z*-axis, which enhances the read-out signal of the probe beam. Miyazaki *et al.*[154] used dual-pump lasers to image mouse melanoma tissue in 3D with subdiffraction spatial resolution. The speed of image acquisition was improved using a laser scanning technique instead of a sample scanning method. Piezo-stage scanning requires longer integration times, usually 1 to 10 ms per pixel, which limits live tracking of fast diffusing objects. Using scanning mirrors, the pixel dwell time was reduced to up to 80 μs, enabling recording of a 500 × 500 pixel image in 20 s which otherwise took tens of minutes.[148] These authors used this fast technique for 3D imaging of mouse brain cortex for detecting endogenous nonfluorescent chromophores in blood cells and lipofuscin in lysosomes and lipid structures (Figure 18). Further, dual wavelength photothermal imaging was used to differentiate endogenous chromophores based on their differential absorption coefficient by spectral unmixing. The dynamics of lysosomes and mitochondria interaction was studied, revealing that lysosomes move around the mitochondrial network with evidence that it was regulated by protein motors.[50]

Zhang *et al.*[59] used a mid-infrared laser as pump to selectively excite vibrational states of the endogenous chromophores and probed the refractive index gradient with a visible laser, achieving unparalleled chemical contrast and submicrometer spatial resolution in IR imaging. They

https://dx.doi.org/10.1021/acsnano.0c07638
ACS Nano 2020, 14, 16414−16445

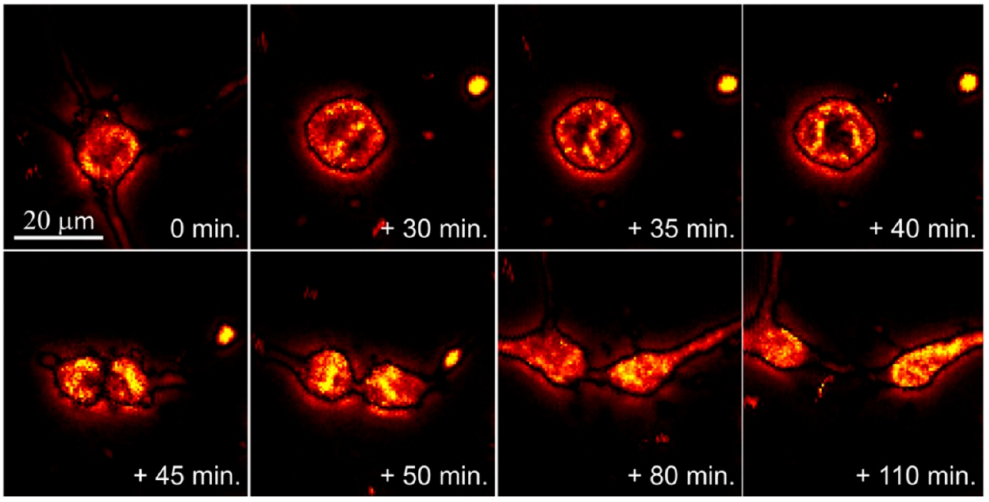

Figure 19. Time-lapse visualization of cell division of oligodendrocytes in the course of about 2 h, representing different phases of cell division: normal (at 0 min), metaphase (at +30 min) and cytokinesis (at +50 min). The change of the contrast between images is due to the change of proteins localization during the cell replication. Reprinted from ref 147. Copyright 2019 American Chemical Society.

monitored lipid droplets in a PC-3 prostate cancer cell in 3D by selectively exciting C═O bond vibrations at 1750 cm^{-1}. They carried out *in vivo* imaging of biomolecules in *C. elegans* and also monitored the diffusion of drug molecules inside living cancer cells. Lim *et al.*[147] used mid-IR photothermal microscopy to monitor the cytoplasmic protein distribution during the entire life cycle of oligodendrocytes, providing information about cell dynamics. Axonal transport through cytoskeletal filaments was also monitored without any exogenous label. Thus, photothermal microscopy provides an excellent platform for truly noninvasive monitoring of biophysical processes in biological media. Figure 19 shows time-lapse images of cell division of individual oligodendrocyte cells over about 2 h without any cell damage, highlighting the label-free imaging ability of mid-IR photothermal microscopy for studying cellular dynamics. The photothermal imaging shows highly contrasted images due to the distribution of protein concentrations inside the cell, and thus mid-IR photothermal imaging provides important information about spatiotemporal dynamics of cell division.

In spite of its numerous applications in biological imaging, photothermal microscopy is still unable to image particles below 5 nm with sufficient sensitivity in cellular environments, due to the poor thermorefractive behavior of water. The sensitivity enhancement of photothermal microscopy by organic liquids and supercritical fluids, which has found applications in nanomaterial science, is difficult to apply to biological specimens. Techniques developed for electron microscopy of biological samples and soft matter,[155−158] however, could be applied to isolate the biological sample from the detector fluid. There is certainly a need for improving the method toward imaging of smaller gold nanoparticles in living cells. Labeling of smaller-sized probes is essential for cellular imaging so that the probe does not alter the intrinsic properties of a target biomolecule too strongly. Although photothermal microscopy has reached single-molecule sensitivity, these experiments cannot be easily transposed to biological conditions because they require very high excitation powers which would damage living cells. Photodamage can be turned into a benefit for imaging during photothermal therapy, in which light is used to damage cancer cells. Additionally, absorbing probes such as organic and inorganic nanoparticles, or intrinsic absorbers such as melanin could provide a better alternative than single-molecule absorption. Some organic molecular probes such as croconaine dyes show high photostability and highly efficient photothermal heating.[159]

A crucial advantage for the development of single-molecule fluorescence microscopy was its wide-field imaging modality made possible by fast and sensitive cameras. Despite early demonstrations of wide-field photothermal microscopy, the SNR in these demonstrations has not been high enough to offset the advantages of fluorescence microscopy, despite its many limitations and drawbacks. Therefore, a sensitive wide-field photothermal method would considerably improve the prospects of this method for biological applications.

Just as fluorescence microscopy benefits from the many colors of dyes, multicolor photothermal imaging[52,148,160] would enable simultaneous imaging of different endogenous components inside a cell, either with proper labels or label-free. Gold nanorods with various sizes and aspect ratios can be tuned over a broad range of colors far from the absorption of cellular components, thereby enabling true multicolor biological photothermal imaging.[160,161]

PHOTOTHERMAL DETECTION OF CIRCULAR DICHROISM

In this section, we highlight the application of photothermal imaging in the field of circular dichroism spectroscopy. Circular dichroism is an effect found in chiral materials and molecules which lack mirror symmetry. It is the difference of absorption between right- and left-circularly polarized light. Circularly polarized light being itself chiral, left-handed circular polarized (LCP) and right-handed circular polarized (RCP) waves interact differently with a chiral material. The major challenge behind measuring chirality is the weakness of interactions between light and a chiral molecule in the visible range, which is due to the small size of the molecule compared to the helical pitch of circularly polarized light.[162] To enhance this weak interaction, several approaches were proposed using special geometries of plasmonic[162] or dielectric[163] nanostructures that can increase the helicity of light beyond that of a plane wave. These nanostructures are supposed to amplify the

https://dx.doi.org/10.1021/acsnano.0c07638
ACS Nano 2020, 14, 16414−16445

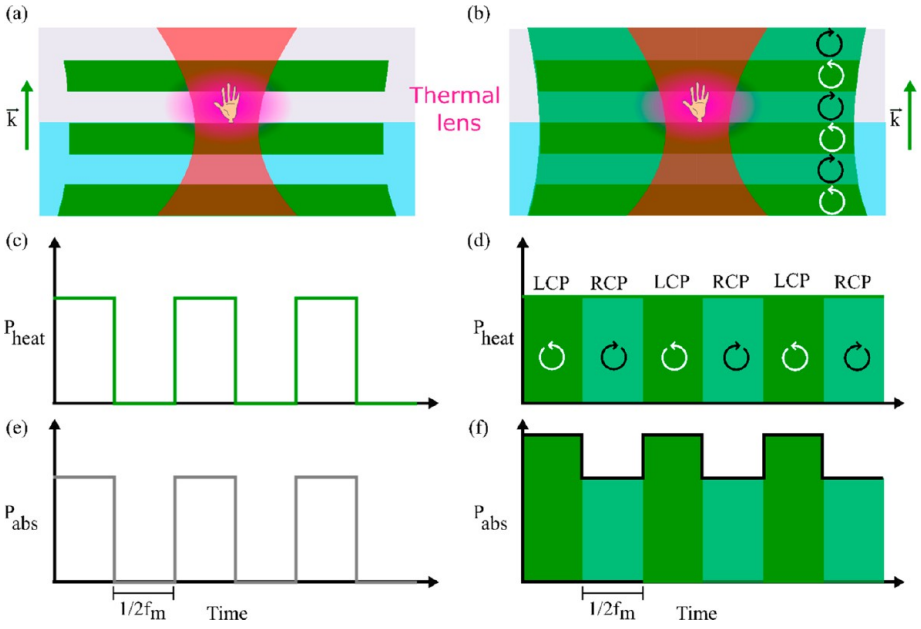

Figure 20. Schematic of "normal" photothermal (left) and photothermal circular dichroism (right) concept. (a) Scheme of the photothermal detection of a chiral structure (illustrated as a hand) with the wide-field heating. The heating beam (green) is Koehler illuminated, and the probe beam (red) is focused to the diffraction limit. The intensity of the heating beam is modulated between on- and off-states at a frequency f_m. The heat released by the heated nanostructure to the environment creates a thermal lens (in purple) around the nanostructure. The wavevector direction (k) for both beams is shown. (b) Scheme for photothermal circular dichroism with modulation of the polarization state of the heating beam between left and right circularly polarized light (dark and light green, respectively). (c) Time evolution of the modulation of the heating power for the "normal" photothermal microscopy, following the intensity modulation pattern at f_m. (d) Time evolution of the heating power of the modulated polarized beams for the photothermal circular dichroism microscopy. In this case, the heating power remains constant and only the polarization state changes. (e) Time evolution of the absorbed power by the nanostructure for the "normal" photothermal case. (f) Time evolution of the absorbed power by the nanostructure for the photothermal circular dichroism case. As the nanostructure is chiral, the absorbed powers for LCP and RCP are different. Reprinted from ref 101. Copyright 2019 American Chemical Society.

interaction of light and chiral molecules such that the differential absorption rate increases.[162−164] Another approach uses the coupling of achiral plasmonic structures with chiral molecules to create a chiral coupled plasmonic system *via* Coulomb interactions.[165,166] Plasmonic fields are expected to enhance the chiral response at the plasmonic resonance. These approaches are intrinsically limited to the plasmonic spectral bandwidth, depending on the geometry of the structures used. Thus, there is a need for a more sensitive approach in the entire spectral range and one that does not require nanofabrication. Recent experimental work shows that circular dichroism can be measured using photothermal microscopy, and that the so-called photothermal circular dichroism (PT CD) is an alternative method to investigate single absorbing chiral particles[101,167] with the potential to improve the sensitivity of existing techniques by at least 1 order of magnitude.[101]

To detect the weak differential absorption of light against noise, most of the established techniques use fast polarization modulators such as electro-optic modulator (EOM)[168] and photoelastic modulator (PEM).[169] These modulators periodically change the polarization of the probe light and thereby shift the differential absorption signal's frequency to the range 10−100 kHz. A lock-in amplifier can then extract the signal with excellent noise rejection. The major challenge in these experiments is the rejection of artifacts due to depolarization in the sample itself but also in all optical components placed between modulator and detector.[170−174] Modern CD spectrometers analyze the light transmitted by the sample and use a dual modulation scheme,[175,176] where the sample is placed between two polarization modulators operated at different frequencies. However, this method has several limitations and drawbacks. First, it lacks spatial resolution. When focused with a high NA objective, polarized light shows a complex polarization distribution in the focus, which is very sensitive to tiny defects and misalignments. Second, conventional CD spectrometers, being based on transmission or reflection instead of absorption, are sensitive not only to absorption but also to birefringence. Artifacts[177] induced by linear birefringence are well-known in CD spectrometry. Another consequence of a transmission-based approach is that multiple scattering through the medium, usually a cuvette with several millimeters of optical path, causes partial depolarization of the transmitted light and therefore gives rise to artifacts, as well.[167]

As recently shown, CD can be measured and quantified with polarization-modulated photothermal measurements (PT CD) more sensitively than with previous methods.[178] PT CD, being a pump−probe method, has the advantage of having the high spatial resolution of its tightly focused probe beam, while providing a good polarization control of the heating beam because of its wide-field profile. Another benefit is that any PT CD microscope can be easily switched to a normal PT microscope allowing the measurement of the absorption cross section and therefore directly provides a quantitative value for the differential CD absorption cross section. Unlike the transmission-based methods, it directly measures absorption and is therefore not limited by the effects of birefringence and depolarization. Although insensitivity to birefringence is a great

https://dx.doi.org/10.1021/acsnano.0c07638
ACS Nano 2020, 14, 16414−16445

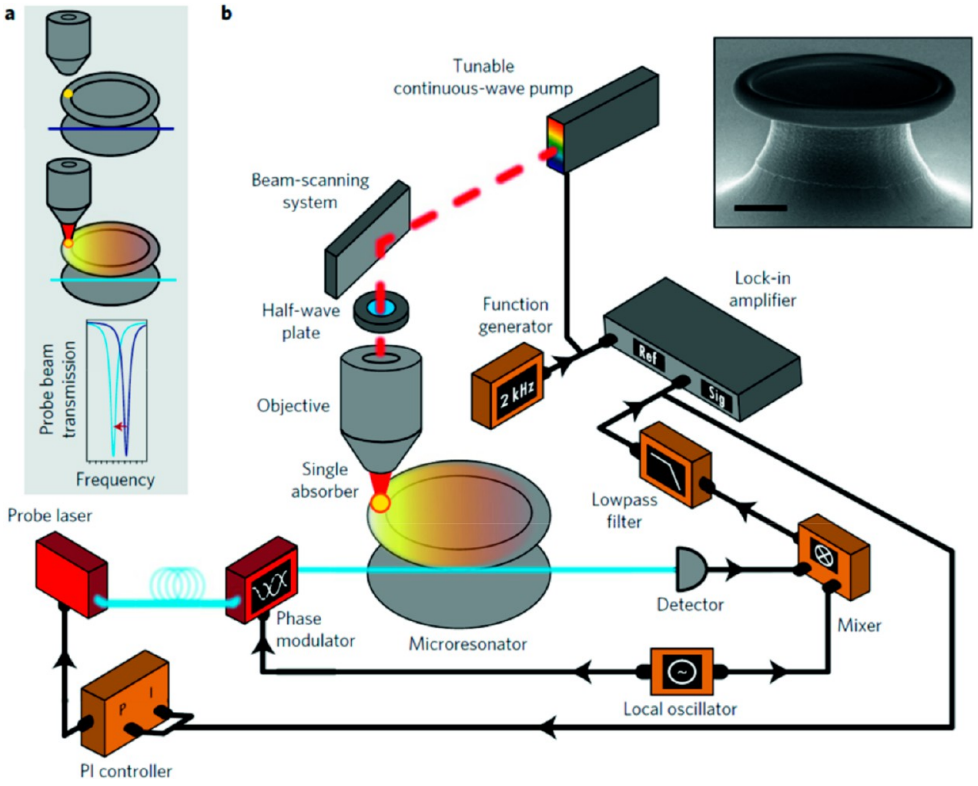

Figure 21. Transducers for localized photothermal spectroscopy: optical transducer based on WGM resonators. Adapted with permission from ref 200. Copyright 2016 Springer Nature. Panel (a) illustrates the shift of the Lorentzian-shaped fiber transmission spectrum of a WGM upon switching of the probe beam and the consequent heating of the resonators material *via* absorption by the analyte. Panel (b) depicts the optical setup and the pump−probe scheme utilizing double modulation. The top inset shows a SEM micrograph of a microtoroidal resonator (scale bar 10 μm).

advantage for samples where polarization is hard to control, it obviously comes at the cost that pure birefringent effects cannot be measured by this method: absorption is needed.

Figure 20 shows a schematic comparison of "normal" photothermal microscopy that measures absorption and PT CD microscopy that is sensitive to the differential absorption of left-handed and right-handed circularly polarized light. In the scheme in Figure 20, an EOM is used instead of a PEM because it is able to perform a square wave modulation that avoids creation of linear polarization states, as proposed in refs 179 and 180, and therefore is supposedly blind to linear dichroism. However, the technique in principle also works with sinusoidal modulation and therefore can be implemented in CD microscopes equipped with PEM modulators. The basic principle is that the polarization modulation of the heating beam will lead to a differential absorption of left and right circular polarized light by a chiral nano-object. Compared to the "normal" photothermal method, it is not the intensity modulation of the heating beam but the polarization-dependent absorption of the molecule or particle that generates a modulation of the absorbed power by the nanoparticle and thus a time-dependent photothermal response. Due to the modulation of polarization at high frequency, shot-noise-limited detection of photothermal CD can be achieved. As a proof of principle of the method, Spaeth *et al.*[101] measured circular dichroism signals of single metallic chiral plasmonic nanostructures with a signal-to-noise ratio of more than 40 with only 30 ms integration time. The high sensitivity of the method promises widespread application toward detecting very weak CD signals of chiral materials down to numbers of molecules much smaller than in conventional CD measurements. Although the method was demonstrated in a reflection-based geometry, PT CD can also be implemented in a transmission configuration. The transmission geometry requires an additional microscope objective, but it allows independent control of the excitation and detection paths. In addition, the forward (or transmission) detection mode presents a higher photothermal sensitivity at low modulation frequencies, below 1 MHz, compared to the backward (or reflection) detection mode.

The major benefits of PT CD, its diffraction-limited spatial resolution and its superior sensitivity, promise to enable CD studies of much smaller numbers of chiral molecules such as proteins or other biomolecules. However, most biomolecules absorb in the UV range rather than in the visible range. The photothermal CD microscope demonstrated by Spaeth *et al.*[101] needs to be upgraded for use in the UV wavelength range.[181] Being a pump−probe-based technique, PT CD will still allow high spatial resolution without the need of special UV optics. A potential alternative for measuring CD in the UV is to transfer chirality of molecules from the UV range to the visible range using plasmonic nanostructures as demonstrated by Maoz *et al.*[165] This approach requires plasmonic enhancement to detect weak CD signals of chiral molecules. However, the plasmonic enhancement is limited to a small spectral range and therefore, this technique cannot provide a full CD spectrum. Most of the knowledge gained in the field of polarization−modulation CD spectroscopy could also be applied to improve artifact subtraction.[177] It is important to emphasize that photothermal CD naturally is blind to birefringence and depolarization

https://dx.doi.org/10.1021/acsnano.0c07638
ACS Nano 2020, 14, 16414−16445

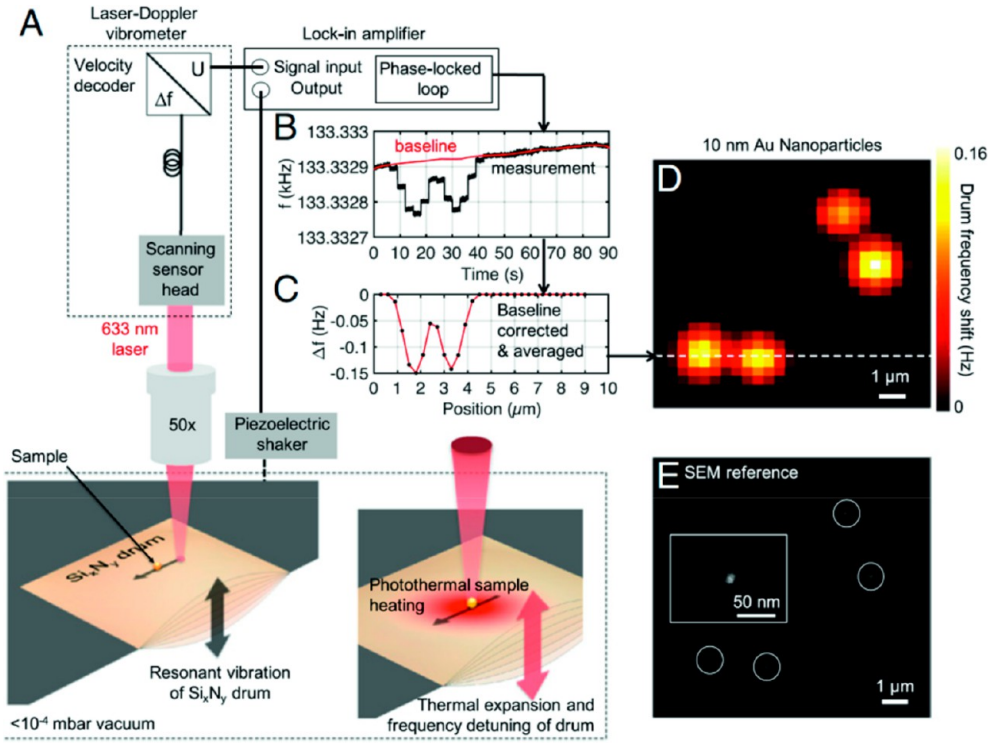

Figure 22. Transducers for localized photothermal spectroscopy: nanomechanical transducer based on a nanodrum resonator. Adapted with permission under a creative commons CC BY-NC-ND license from ref 218. Copyright 2018 PNAS. Panel (A) depicts the experimental setup and the principle of detection is illustrated in the subpanel at the bottom left. It depicts a line scan over a 10 nm diameter gold nanoparticle. The recorded signal and its processing are shown in panels (B) and (C). Panel (D) shows a 2D scan of 10 nm gold nanoparticles alongside the reference micrograph 2E with a higher-resolution image as the inset.

effects of the sample, provided the polarization of the heating beam is well-controlled. Furthermore, PT CD can easily be combined with other methods[162,163,165] of detecting CD to even further increase its sensitivity. Thanks to its superior sensitivity and spatial resolution, PT CD could help measure the CD spectrum of very small numbers of molecules, perhaps even of single molecules. Another promising field of application of PT CD is vibrational CD, which sensitively reports on the secondary structure of proteins.[182] Combining mid-IR heating with the superior spatial resolution of a visible probe beam[59] would open vibrational CD at the submicron scale.

PHOTOTHERMAL DETECTION WITH TEMPERATURE-SENSITIVE DEVICES

The systems described here utilize additional temperature-sensitive transducer mechanisms which amplify minute photothermally induced temperature changes of their physical properties. Typically, these devices exhibit resonant modes with high-quality factors. These narrow resonances allow for the accurate measurement of resonance frequency shifts associated with the photothermally induced changes.

Optical Transducers. Whispering gallery mode (WGM) resonators are a special family of optical cavities which can exhibit high *Q*-factors[183] in excess of 10^9 and small device footprints typically well below 0.1 mm^2. These resonators were used for a broad range of applications[5,184−188] including the detection of single molecules[189−193] and the generation of frequency combs.[194−196] For sensing applications, WGM resonator-type sensors usually rely on observation of WGM frequency shifts, and the refractive response outweighs the thermorefractive response for small analytes such as protein molecules.[197] Refractive shifts are proportional to the polarizability of the analyte[198] at a given wavelength, as a consequence of the discrimination between analyte species of similar mass and composition can usually only be achieved by utilizing analyte-specific chemical receptors. This limits the number of analyte species that can be investigated with a single device. Therefore, obtaining additional analyte information *via* spectroscopy is highly desirable. Goldsmith's group has recently demonstrated photothermal spectroscopy and localization of single gold nanoparticles using microtoroids. These resonators were specifically fabricated for the purpose of minimizing unwanted absorption[199] and were paired with a thoroughly optimized pump−probe double modulation scheme[200] (Figure 21b). The nanoparticles were deposited on the resonator where the absorption of a probe light heats the resonator's material. This locally alters the refractive index and consequently shifts the resonance frequency of the WGM whenever the pump beam with a tunable wavelength hits a particle's location (Figure 21a). These resonance frequency shifts are detected with an additional probe laser far detuned (1.55 μm) with respect the nanoparticles' absorption lines. Absorption spectra obtained using this modality exhibit narrow Fano patterns[200,201] atop the bare nanoparticle absorption spectra. The Fano-patterns are the result of coupling between the low-*Q* LSPR of the nanoparticles and the high-*Q* resonance of a WGM, and their individual shapes are characteristic for the detuning between both resonances frequencies. Heylman *et al.*[200] reported that their method is capable of detecting thermal powers of 20 pW exceeding the requirements for the photothermal detection of single dye molecules (15 nW[22]) by

https://dx.doi.org/10.1021/acsnano.0c07638
ACS Nano 2020, 14, 16414−16445

3 orders of magnitude. However, no such detection has been demonstrated so far. Nonetheless, the fabrication of microtoroids with better photothermal properties promises even higher sensitivities.[202] One shortcoming of the microtoroid resonator geometry is its restricted compatibility for measurements in solution.[203] Here different resonator geometries, which confine the solvent on the resonators inside, such as microbubble resonators[203] were identified as promising candidates for future WGM-based photothermal spectroscopic studies. Well-controlled droplet resonators[204] might offer another possible route in addition to the currently investigated geometries, naturally coming with its own set of challenges. WGM-based photothermal spectroscopy is a promising, although technically very demanding, future candidate for the recognition and identification of single analytes on the single-molecule level.

Mechanical Transducers. Early mechanical transducers used as probes for photothermal absorption were based on the heat-induced bending of bimetal cantilevers probed *via* deflection of a laser beam and had fundamental limits of heat power sensitivity in the order of 10 pW.[205,206] For measurements, usually a thin film of absorbent material is deposited on top of the cantilever. This method of photothermal spectroscopy was used for a range of investigations encompassing, for example, the detection of dangerous chemicals[207−210] and biomolecules[211] as well as the study of thin polymer films.[212,213] However, cantilever deflection is limited by thermomechanical noise and prone to external vibration sources.[214] In comparison, photothermal probing of mechanical string resonators offer several advantages. With this type of mechanical resonators, photothermal spectroscopy is performed *via* the robust measurement of resonance frequency shifts—typically probed *via* a laser Doppler vibrometer—which comes with the added advantage of lower thermal dissipation as the bimetal coatings are not required. These strings are typically made from silicon nitride and resemble guitar strings spanned over a gap under tension.[215] With these string resonators, photothermal spectroscopy on single analyte nanoparticles[216] was achieved with detection limits for thermal powers in the range of 10 pW.[214] Together with probe beam scanning the nanostring transducers also allow for the localization and mapping of nanoparticle and nanostructures.[217] Chien *et al.* have recently demonstrated that silicon nitride membrane nanomechanical drums can be utilized as transducers for probing and localizing single-molecule absorption.[218] Absorption of light by single gold nanoparticles and molecules heats the nanomechanical drum. The consequent thermal expansion of the drum reduces the tensile stress and alters the drum's resonance frequency. These frequency shifts are measured utilizing a laser Doppler vibrometer (Figure 22). This configuration allows to probe absorbed power with a sensitivity of 16 fW/Hz$^{1/2}$ at room temperature and yields a signal-to-noise ratio larger than 70 for a single Atto633 fluorophore with an integration time of 40 ms. Chien *et al.* also recently demonstrated photothermal detection of subnanometer beam displacements using a trampoline resonator.[219] Localized photothermal spectroscopy paired with mechanical transducers is an extremely sensitive and powerful tool, however, operation of these transducers faces certain experimental restrictions as they require low-pressure environments and so far exclude probing of samples in solution.

CONCLUSION AND OUTLOOK

In this review, we have discussed the recent developments of photothermal microscopy, the origin of the signal, and its applications in nanomaterial science and biology. Since its report[20] on imaging single metal nanoparticles in 2002, the technique has evolved in various ways.

(1) Photothermal heterodyne imaging achieved shot-noise-limited detection of single absorbing nanoparticles or molecules without any background from strong scatterers in the object's environment. This gives the technique a high potential for applications in cells and tissues.

(2) The method's sensitivity was improved by several orders of magnitude compared to its report in 2002, mainly by optimizing the thermorefractive coefficient (dn/dT) of the medium, for example by means of pentane, or of a liquid crystal (5CB), or of a near-critical fluid (Xe or CO_2). With near-critical enhancement, single molecules could be imaged at low excitation powers at which the probability of photobleaching was reduced.

(3) Photothermal imaging has shown great promise in detecting weakly or nonfluorescent molecular probes which are more resistant to photobleaching at higher excitation powers because of their very fast nonradiative rates. There are large numbers of such molecules, among which some are highly photostable. Such molecules could be alternative molecular probes for biological applications, which would be small in size and highly photostable.

(4) Gold nanoparticles being highly photostable and biocompatible became ideal probes for cellular imaging and photothermal microscopy, as demonstrated with biomolecules labeled with gold nanoparticles down to 5 nm in size. Photothermal microscopy has also shown its capability of performing label-free imaging in a living cell as some endogeneous organelles absorb visible light.

(5) The super-resolution behavior of the mid-IR photothermal microscopy is of great advantage for the chemical characterization of specimens, particularly for biological applications.Mid-IR photothermal imaging based on vibrational absorption provides chemical contrast in cellular imaging, by not only allowing label-free imaging but also by characterizing individual cellular elements through their IR fingerprints while keeping the spatial resolution an order of magnitude better than that of a standard IR microscope.

(6) Very recently, photothermal circular dichroism microscopy was developed to detect tiny circular dichroism signals of single chiral nano-objects. This was previously only possible using nonabsorption based methods. PT CD microscopy provides CD signals of chiral objects in a direct and reliable manner. The polarization state of a focused beam is quite complex whereas the plane wave diminishes the spatial resolution. PT CD microscopy overcame both limitations using heating beam illumination at a low NA but with a focused probe beam.

Although photothermal microscopy has had a significant impact in material science and biology, much work is still needed to broaden its field of application. Here are some outlooks:

(1) In terms of theory, photothermal microscopy in its backward detection mode (*i.e.*, reflection mode) is not well-understood. The reference beam in this configuration is not well-defined and the reflected profile is quite complex. The reference beam could be the reflection from the substrate and

https://dx.doi.org/10.1021/acsnano.0c07638
ACS Nano 2020, 14, 16414−16445

oil (or air) interface and the direct scattering by the particle itself for larger nanoparticles. A better theoretical understanding would certainly help in exploring the technique's improvement in detection sensitivity.

(2) More studies are needed to explore many available weakly or nonfluorescent molecular probes which produce stronger photothermal signals due to their fast nonradiative rates as demonstrated by BHQ dye molecules and croconaine dyes. These molecular probes are also highly resistant to photobleaching and thus allow using higher excitation powers to obtain a better signal-to-noise. Suitable molecular probes must be designed and functionalized to enable photothermal single-molecule imaging in biological systems.

(3) Critical xenon as a transducing medium enhances the photothermal SNR by 2 orders of magnitude compared to commonly used organic liquids. This detection scheme has allowed to image single semiconducting polymer chains and to understand better their complex photophysics. We foresee that further studies of this kind will allow a better understanding of the optical properties of many other multichromophoric systems and of semiconducting nanocrystals. Instead of xenon, one can use critical CO_2 which is cheaper and whose critical temperature is slightly higher than room temperature.

(4) Most photothermal imaging was performed by means of scanning confocal microscopes, which limits imaging speed and applications to a broader class of systems. Wide-field photothermal microscopy is certainly in the development phase and it is a safe bet that modern ultrafast cameras and lock-in cameras will help in building simple wide-field photothermal microscopes in next few years.

(5) Photothermal super-resolution microscopy also enters a development phase. Super-resolution based on nanobubble formation surrounding an overheated nanoparticle has already achieved beyond diffraction-limit resolution, despite foreseeable difficulties in applications to biological samples. The PAINT super-resolution method appears to be immediately applicable for localization using photothermal contrast.

(6) A very recently developed photothermal circular dichroism microscope will be used to explore single chiral systems such as protein molecules. The technique has yet to be adapted for the detection of chirality in the UV range of amino-acid absorption. Another promising field is photothermal vibrational CD in the mid-IR.

(7) Photothermal microscopy can also be used to study chemical reactions[220,221] assuming sufficient local refractive index change near a plasmonic particle due to the chemical reaction, which would shift the surface plasmon and thus the photothermal signal.

In this review, we have discussed the principles of photothermal microscopy, a technique that lends optical contrast to optical absorption. In many cases, we have seen how the absorption information can complement, and sometimes supersede the more traditional modalities of fluorescence or Raman scattering. Although most recent developments of optical microscopy, in particular single-molecule measurements and super-resolution, are based on fluorescence, nonfluorescent optical detection techniques are appearing and attract more and more attention. Among those, photothermal microscopy has the advantages of being easy to implement and of being nearly insensitive to scattering of the sample, as long as it does not hamper light propagation significantly. Although it is far less sensitive than fluorescence, photothermal microscopy can image tiny metal nanoparticles, down to a size of 1.4 nm, not much bigger than single organic dye molecules. Imaging such molecular-sized probes without bleaching or blinking is a promising asset in the study of biological systems. Yet, despite spectacular recent progress in photothermal microsocopy, relatively few researchers are currently using and developing the technique. We hope that this article, by reviewing the main past results of this technique, by highlighting its exciting perspectives in wide-field imaging, super-resolution microscopy, and chemically sensitive imaging in the mid-IR will make photothermal microscopy accessible and attractive to a broader community of researchers.

AUTHOR INFORMATION

Corresponding Authors

Michel Orrit − *Huygens–Kamerlingh Onnes Laboratory, Leiden University, 2300 RA Leiden, The Netherlands;* orcid.org/0000-0002-3607-3426; Email: orrit@physics.leidenuniv.nl

Saumyakanti Khatua − *Chemistry Discipline, Indian Institute of Technology Gandhinagar, Gujrat 382355, India;* orcid.org/0000-0002-8088-2132; Email: khatuask@iitgn.ac.in

Authors

Subhasis Adhikari − *Huygens–Kamerlingh Onnes Laboratory, Leiden University, 2300 RA Leiden, The Netherlands;* orcid.org/0000-0002-0914-433X

Patrick Spaeth − *Huygens–Kamerlingh Onnes Laboratory, Leiden University, 2300 RA Leiden, The Netherlands*

Ashish Kar − *Chemistry Discipline, Indian Institute of Technology Gandhinagar, Gujrat 382355, India*

Martin Dieter Baaske − *Huygens–Kamerlingh Onnes Laboratory, Leiden University, 2300 RA Leiden, The Netherlands;* orcid.org/0000-0003-2384-7557

Complete contact information is available at: https://pubs.acs.org/10.1021/acsnano.0c07638

Notes

The authors declare no competing financial interest.

ACKNOWLEDGMENTS

S.A., P.S., and M.O. acknowledge The Netherlands Organisation for Scientific Research (NWO/OCW), as part of the Open Technology Program (OTP, Project No. 16008). S.K. acknowledges financial support from Science and Engineering Research Board, India (project: EMR/2015/0013) and the Department of Science and Technology, India (SR/NM/NS-65/2016).

VOCABULARY

Photothermal microscopy, a microscopic technique to detect absorption signals by measuring the change of the scattering intensity of a probe beam induced by the thermal lens surrounding a nanoobject heated by a pump beam. It is often applied to study of single nanoparticles and single molecules

Photothermal correlation spectroscopy, a spectroscopic method to measure diffusion coefficient/hydrodynamic radius of a nanoobject by calculating auto/cross- correlations of photothermal signals arising from a diffusing object through the confocal volume

https://dx.doi.org/10.1021/acsnano.0c07638
ACS Nano 2020, 14, 16414−16445

Mid-infrared photothermal microscopy, a photothermal technique which uses a mid-IR laser as the heating beam and a visible laser as the probe beam. It has the advantage of providing vibrational chemical contrast

Thermal lens, a refractive index profile due to the thermal gradient surrounding a heated nanoparticle, which acts as a nanolens

Circular dichroism, a property of a chiral object, consisting of the differential absorption of the left- and right-circularly polarized light

REFERENCES

(1) Moerner, W. E.; Orrit, M. Illuminating Single Molecules in Condensed Matter. *Science* **1999**, *283*, 1670−1676.

(2) Moerner, W. E.; Shechtman, Y.; Wang, Q. Single-Molecule Spectroscopy and Imaging over the Decades. *Faraday Discuss.* **2015**, *184*, 9−36.

(3) Moerner, W. E.; Kador, L. Optical Detection and Spectroscopy of Single Molecules in a Solid. *Phys. Rev. Lett.* **1989**, *62*, 2535−2538.

(4) Orrit, M.; Bernard, J. Single Pentacene Molecules Detected by Fluorescence Excitation in a *p* -Terphenyl Crystal. *Phys. Rev. Lett.* **1990**, *65*, 2716−2719.

(5) Jollans, T.; Baaske, M. D.; Orrit, M. Nonfluorescent Optical Probing of Single Molecules and Nanoparticles. *J. Phys. Chem. C* **2019**, *123*, 14107−14117.

(6) Arbouet, A.; Christofilos, D.; Del Fatti, N.; Vallée, F.; Huntzinger, J. R.; Arnaud, L.; Billaud, P.; Broyer, M. Direct Measurement of the Single-Metal-Cluster Optical Absorption. *Phys. Rev. Lett.* **2004**, *93*, 127401.

(7) Billaud, P.; Huntzinger, J.-R.; Cottancin, E.; Lermé, J.; Pellarin, M.; Arnaud, L.; Broyer, M.; Del Fatti, N.; Vallée, F. Optical Extinction Spectroscopy of Single Silver Nanoparticles. *Eur. Phys. J. D* **2007**, *43*, 271−274.

(8) Muskens, O. L.; Bachelier, G.; Fatti, N. D.; Vallée, F.; Brioude, A.; Jiang, X.; Pileni, M.-P. Quantitative Absorption Spectroscopy of a Single Gold Nanorod. *J. Phys. Chem. C* **2008**, *112*, 8917−8921.

(9) Chong, S.; Min, W.; Xie, X. S. Ground-State Depletion Microscopy: Detection Sensitivity of Single-Molecule Optical Absorption at Room Temperature. *J. Phys. Chem. Lett.* **2010**, *1*, 3316−3322.

(10) Taylor, R. W.; Sandoghdar, V. Interferometric Scattering Microscopy: Seeing Single Nanoparticles and Molecules *via* Rayleigh Scattering. *Nano Lett.* **2019**, *19*, 4827−4835.

(11) Lindfors, K.; Kalkbrenner, T.; Stoller, P.; Sandoghdar, V. Detection and Spectroscopy of Gold Nanoparticles Using Supercontinuum White Light Confocal Microscopy. *Phys. Rev. Lett.* **2004**, *93*, 037401.

(12) Ignatovich, F. V.; Novotny, L. Real-Time and Background-Free Detection of Nanoscale Particles. *Phys. Rev. Lett.* **2006**, *96*, 013901.

(13) Jacobsen, V.; Stoller, P.; Brunner, C.; Vogel, V.; Sandoghdar, V. Interferometric Optical Detection and Tracking of Very Small Gold Nanoparticles at a Water-Glass Interface. *Opt. Express* **2006**, *14*, 405−414.

(14) Kukura, P.; Celebrano, M.; Renn, A.; Sandoghdar, V. Single-Molecule Sensitivity in Optical Absorption at Room Temperature. *J. Phys. Chem. Lett.* **2010**, *1*, 3323−3327.

(15) Celebrano, M.; Kukura, P.; Renn, A.; Sandoghdar, V. Single-Molecule Imaging by Optical Absorption. *Nat. Photonics* **2011**, *5*, 95−98.

(16) Kukura, P.; Celebrano, M.; Renn, A.; Sandoghdar, V. Imaging a Single Quantum Dot When It Is Dark. *Nano Lett.* **2009**, *9*, 926−929.

(17) Horak, E. H.; Rea, M. T.; Heylman, K. D.; Gelbwaser-Klimovsky, D.; Saikin, S. K.; Thompson, B. J.; Kohler, D. D.; Knapper, K. A.; Wei, W.; Pan, F.; Gopalan, P.; Wright, J. C.; Aspuru-Guzik, A.; Goldsmith, R. H. Exploring Electronic Structure and Order in Polymers *via* Single-Particle Microresonator Spectroscopy. *Nano Lett.* **2018**, *18*, 1600−1607.

(18) Heylman, K. D.; Knapper, K. A.; Goldsmith, R. H. Photothermal Microscopy of Nonluminescent Single Particles Enabled by Optical Microresonators. *J. Phys. Chem. Lett.* **2014**, *5*, 1917−1923.

(19) Knapper, K. A.; Pan, F.; Rea, M. T.; Horak, E. H.; Rogers, J. D.; Goldsmith, R. H. Single-Particle Photothermal Imaging *via* Inverted Excitation through High-Q All-Glass Toroidal Microresonators. *Opt. Express* **2018**, *26*, 25020−25030.

(20) Boyer, D.; Tamarat, P.; Maali, A.; Lounis, B.; Orrit, M. Photothermal Imaging of Nanometer-Sized Metal Particles Among Scatterers. *Science* **2002**, *297*, 1160−1163.

(21) Boyer, D.; Tamarat, P.; Maali, A.; Orrit, M.; Lounis, B. Imaging Single Metal Nanoparticles in Scattering Media by Photothermal Interference Contrast. *Phys. E* **2003**, *17*, 537−540.

(22) Gaiduk, A.; Yorulmaz, M.; Ruijgrok, P. V.; Orrit, M. Room-Temperature Detection of a Single Molecule's Absorption by Photothermal Contrast. *Science* **2010**, *330*, 353−356.

(23) Hou, L.; Adhikari, S.; Tian, Y.; Scheblykin, I. G.; Orrit, M. Absorption and Quantum Yield of Single Conjugated Polymer Poly[2-Methoxy-5-(2-Ethylhexyloxy)-1,4-Phenylenevinylene] (MEH-PPV) Molecules. *Nano Lett.* **2017**, *17*, 1575−1581.

(24) Berciaud, S.; Lasne, D.; Blab, G. A.; Cognet, L.; Lounis, B. Photothermal Heterodyne Imaging of Individual Metallic Nanoparticles: Theory *versus* Experiment. *Phys. Rev. B: Condens. Matter Mater. Phys.* **2006**, *73*, 045424.

(25) Selmke, M.; Braun, M.; Cichos, F. Photothermal Single-Particle Microscopy: Detection of a Nanolens. *ACS Nano* **2012**, *6*, 2741−2749.

(26) Selmke, M.; Heber, A.; Braun, M.; Cichos, F. Photothermal Single Particle Microscopy Using a Single Laser Beam. *Appl. Phys. Lett.* **2014**, *105*, 013511.

(27) Chang, W.-S.; Link, S. Enhancing the Sensitivity of Single-Particle Photothermal Imaging with Thermotropic Liquid Crystals. *J. Phys. Chem. Lett.* **2012**, *3*, 1393−1399.

(28) Yorulmaz, M.; Nizzero, S.; Hoggard, A.; Wang, L.-Y.; Cai, Y.-Y.; Su, M.-N.; Chang, W.-S.; Link, S. Single-Particle Absorption Spectroscopy by Photothermal Contrast. *Nano Lett.* **2015**, *15*, 3041−3047.

(29) Bialkowski, S. E.; Astrath, N. G. C.; Proskurnin, M. A. *Photothermal Spectroscopy Methods*, 2nd ed.; Wiley: Hoboken, NJ, 2020.

(30) Chien, M.-H.; Schmid, S. Nanoelectromechanical Photothermal Polarization Microscopy with 3 Å Localization Precision. *J. Appl. Phys.* **2020**, *128*, 134501.

(31) Katzenmeyer, A. M.; Holland, G.; Kjoller, K.; Centrone, A. Absorption Spectroscopy and Imaging from the Visible through Mid-Infrared with 20 Nm Resolution. *Anal. Chem.* **2015**, *87*, 3154−3159.

(32) Shen, Y. R. *The Principles of Nonlinear Optics*; Wiley: New York, 2020.

(33) Harada, M.; Iwamoto, K.; Kitamori, T.; Sawada, T. Photothermal Microscopy with Excitation and Probe Beams Coaxial under the Microscope and Its Application to Microparticle Analysis. *Anal. Chem.* **1993**, *65*, 2938−2940.

(34) Mawatari, K.; Kitamori, T.; Sawada, T. Individual Detection of Single-Nanometer-Sized Particles in Liquid by Photothermal Microscope. *Anal. Chem.* **1998**, *70*, 5037−5041.

(35) Tokeshi, M.; Uchida, M.; Hibara, A.; Sawada, T.; Kitamori, T. Determination of Subyoctomole Amounts of Nonfluorescent Molecules Using a Thermal Lens Microscope: Subsingle-Molecule Determination. *Anal. Chem.* **2001**, *73*, 2112−2116.

(36) Berciaud, S.; Cognet, L.; Blab, G. A.; Lounis, B. Photothermal Heterodyne Imaging of Individual Nonfluorescent Nanoclusters and Nanocrystals. *Phys. Rev. Lett.* **2004**, *93*, 257402.

(37) Berciaud, S.; Cognet, L.; Poulin, P.; Weisman, R. B.; Lounis, B. Absorption Spectroscopy of Individual Single-Walled Carbon Nanotubes. *Nano Lett.* **2007**, *7*, 1203−1207.

(38) Zijlstra, P.; Paulo, P. M. R.; Orrit, M. Optical Detection of Single Non-Absorbing Molecules Using the Surface Plasmon Resonance of a Gold Nanorod. *Nat. Nanotechnol.* **2012**, *7*, 379−382.

https://dx.doi.org/10.1021/acsnano.0c07638
ACS Nano 2020, 14, 16414−16445

(39) Berciaud, S.; Cognet, L.; Tamarat, P.; Lounis, B. Observation of Intrinsic Size Effects in the Optical Response of Individual Gold Nanoparticles. *Nano Lett.* **2005**, *5*, 515−518.
(40) Paulo, P. M. R.; Gaiduk, A.; Kulzer, F.; Krens, S. F. G.; Spaink, H. P.; Schmidt, T.; Orrit, M. Photothermal Correlation Spectroscopy of Gold Nanoparticles in Solution. *J. Phys. Chem. C* **2009**, *113*, 11451−11457.
(41) Radünz, R.; Rings, D.; Kroy, K.; Cichos, F. Hot Brownian Particles and Photothermal Correlation Spectroscopy. *J. Phys. Chem. A* **2009**, *113*, 1674−1677.
(42) Digman, M. A.; Brown, C. M.; Sengupta, P.; Wiseman, P. W.; Horwitz, A. R.; Gratton, E. Measuring Fast Dynamics in Solutions and Cells with a Laser Scanning Microscope. *Biophys. J.* **2005**, *89*, 1317−1327.
(43) Nieves, D. J.; Li, Y.; Fernig, D. G.; Lévy, R. Photothermal Raster Image Correlation Spectroscopy of Gold Nanoparticles in Solution and on Live Cells. *R. Soc. Open Sci.* **2015**, *2*, 140454.
(44) Chang, W.-S.; Ha, J. W.; Slaughter, L. S.; Link, S. Plasmonic Nanorod Absorbers as Orientation Sensors. *Proc. Natl. Acad. Sci. U. S. A.* **2010**, *107*, 2781−2786.
(45) Heber, A.; Selmke, M.; Cichos, F. Thermal Diffusivities Studied by Single-Particle Photothermal Deflection Microscopy. *ACS Photonics* **2017**, *4*, 681−687.
(46) Bogart, L. K.; Taylor, A.; Cesbron, Y.; Murray, P.; Lévy, R. Photothermal Microscopy of the Core of Dextran-Coated Iron Oxide Nanoparticles During Cell Uptake. *ACS Nano* **2012**, *6*, 5961−5971.
(47) Lasne, D.; Blab, G. A.; De Giorgi, F.; Ichas, F.; Lounis, B.; Cognet, L. Label-Free Optical Imaging of Mitochondria in Live Cells. *Opt. Express* **2007**, *15*, 14184−14193.
(48) Lu, S.; Min, W.; Chong, S.; Holtom, G. R.; Xie, X. S. Label-Free Imaging of Heme Proteins with Two-Photon Excited Photothermal Lens Microscopy. *Appl. Phys. Lett.* **2010**, *96*, 113701.
(49) Tomimatsu, T.; Miyazaki, J.; Kano, Y.; Kobayashi, T. Photothermal Imaging of Skeletal Muscle Mitochondria. *Biomed. Opt. Express* **2017**, *8*, 2965−2975.
(50) Miyazaki, J.; Toumon, Y. Label-Free Dynamic Imaging of Mitochondria and Lysosomes within Living Cells *via* Simultaneous Dual-Pump Photothermal Microscopy. *Biomed. Opt. Express* **2019**, *10*, 5852−5861.
(51) Miyazaki, J.; Tsurui, H.; Kobayashi, T. Reduction of Distortion in Photothermal Microscopy and Its Application to the High-Resolution Three-Dimensional Imaging of Nonfluorescent Tissues. *Biomed. Opt. Express* **2015**, *6*, 3217−3224.
(52) Nedosekin, D. A.; Galanzha, E. I.; Ayyadevara, S.; Shmookler Reis, R. J.; Zharov, V. P. Photothermal Confocal Spectromicroscopy of Multiple Cellular Chromophores and Fluorophores. *Biophys. J.* **2012**, *102*, 672−681.
(53) He, J.; Wang, N.; Tsurui, H.; Kato, M.; Iida, M.; Kobayashi, T. Noninvasive, Label-Free, Three-Dimensional Imaging of Melanoma with Confocal Photothermal Microscopy: Differentiate Malignant Melanoma from Benign Tumor Tissue. *Sci. Rep.* **2016**, *6*, 30209.
(54) Gu, M.; Sheppard, C. J. R. Comparison of Three-Dimensional Imaging Properties between Two-Photon and Single-Photon Fluorescence Microscopy. *J. Microsc.* **1995**, *177*, 128−137.
(55) Denk, W.; Strickler, J. H.; Webb, W. W. Two-Photon Laser Scanning Fluorescence Microscopy. *Science* **1990**, *248*, 73−76.
(56) So, P. T. C.; Dong, C. Y.; Masters, B. R.; Berland, K. M. Two-Photon Excitation Fluorescence Microscopy. *Annu. Rev. Biomed. Eng.* **2000**, *2*, 399−429.
(57) Sheppard, C. J. R.; Gu, M. Optical Sectioning in Confocal Microscopes with Annular Pupil. *Opt. Sect. Confocal Microsc. Annu. Pupil* **1991**, *86*, 169−172.
(58) Conchello, J.-A.; Lichtman, J. W. Optical Sectioning Microscopy. *Nat. Methods* **2005**, *2*, 920−931.
(59) Zhang, D.; Li, C.; Zhang, C.; Slipchenko, M. N.; Eakins, G.; Cheng, J.-X. Depth-Resolved Mid-Infrared Photothermal Imaging of Living Cells and Organisms with Submicrometer Spatial Resolution. *Sci. Adv.* **2016**, *2*, No. e1600521.
(60) Aleshire, K.; Pavlovetc, I. M.; Collette, R.; Kong, X.-T.; Rack, P. D.; Zhang, S.; Masiello, D. J.; Camden, J. P.; Hartland, G. V.; Kuno, M. Far-Field Midinfrared Superresolution Imaging and Spectroscopy of Single High Aspect Ratio Gold Nanowires. *Proc. Natl. Acad. Sci. U. S. A.* **2020**, *117*, 2288−2293.
(61) Bai, Y.; Zhang, D.; Lan, L.; Huang, Y.; Maize, K.; Shakouri, A.; Cheng, J.-X. Ultrafast Chemical Imaging by Widefield Photothermal Sensing of Infrared Absorption. *Sci. Adv.* **2019**, *5*, No. eaav7127.
(62) Li, Z.; Aleshire, K.; Kuno, M.; Hartland, G. V. Super-Resolution Far-Field Infrared Imaging by Photothermal Heterodyne Imaging. *J. Phys. Chem. B* **2017**, *121*, 8838−8846.
(63) Li, C.; Zhang, D.; Slipchenko, M. N.; Cheng, J.-X. Mid-Infrared Photothermal Imaging of Active Pharmaceutical Ingredients at Submicrometer Spatial Resolution. *Anal. Chem.* **2017**, *89*, 4863−4867.
(64) Bai, Y.; Zhang, D.; Li, C.; Liu, C.; Cheng, J.-X. Bond-Selective Imaging of Cells by Mid-Infrared Photothermal Microscopy in High Wavenumber Region. *J. Phys. Chem. B* **2017**, *121*, 10249−10255.
(65) Lee, E. S.; Lee, J. Y. Nonlinear Optical Infrared Microscopy with Chemical Specificity. *Appl. Phys. Lett.* **2009**, *94*, 261101.
(66) Mërtiri, A.; Jeys, T.; Liberman, V.; Hong, M. K.; Mertz, J.; Altug, H.; Erramilli, S. Mid-Infrared Photothermal Heterodyne Spectroscopy in a Liquid Crystal Using a Quantum Cascade Laser. *Appl. Phys. Lett.* **2012**, *101*, 044101.
(67) Totachawattana, A.; Liu, H.; Mertiri, A.; Hong, M. K.; Erramilli, S.; Sander, M. Y. Vibrational Mid-Infrared Photothermal Spectroscopy Using a Fiber Laser Probe: Asymptotic Limit in Signal-to-Baseline Contrast. *Opt. Lett.* **2016**, *41*, 179−182.
(68) Li, X.; Zhang, D.; Bai, Y.; Wang, W.; Liang, J.; Cheng, J.-X. Fingerprinting a Living Cell by Raman Integrated Mid-Infrared Photothermal Microscopy. *Anal. Chem.* **2019**, *91*, 10750−10756.
(69) Lapotko, D. O.; Zharov, V. P. Spectral Evaluation of Laser-Induced Cell Damage with Photothermal Microscopy. *Lasers Surg. Med.* **2005**, *36*, 22−30.
(70) Lapotko, D.; Shnip, A.; Lukianova, E. Photothermal Responses of Individual Cells. *J. Biomed. Opt.* **2005**, *10*, 014006.
(71) Lapotko, D. Optical Excitation and Detection of Vapor Bubbles around Plasmonic Nanoparticles. *Opt. Express* **2009**, *17*, 2538−2556.
(72) Hou, L.; Yorulmaz, M.; Verhart, N. R.; Orrit, M. Explosive Formation and Dynamics of Vapor Nanobubbles around a Continuously Heated Gold Nanosphere. *New J. Phys.* **2015**, *17*, 013050.
(73) Harada, M.; Shibata, M.; Kitamori, T.; Sawada, T. Application of Coaxial Beam Photothermal Microscopy to the Analysis of a Single Biological Cell in Water. *Anal. Chim. Acta* **1995**, *299*, 343−347.
(74) Brusnichkin, A. V.; Nedosekin, D. A.; Proskurnin, M. A.; Zharov, V. P. Photothermal Lens Detection of Gold Nanoparticles: Theory and Experiments. *Appl. Spectrosc.* **2007**, *61*, 1191−1201.
(75) Harada, M.; Shibata, M.; Kitamori, T.; Sawada, T. Sub-Attomole Molecule Detection in a Single Biological Cell *in-Vitro* by Thermal Lens Microscopy. *Anal. Sci.* **1999**, *15*, 647−650.
(76) Kimura, H.; Sekiguchi, K.; Kitamori, T.; Sawada, T.; Mukaida, M. Assay of Spherical Cell Surface Molecules by Thermal Lens Microscopy and Its Application to Blood Cell Substances. *Anal. Chem.* **2001**, *73*, 4333−4337.
(77) Kitamori, T. Thermal Lens Microscope and Microchip Chemistry. *Bull. Chem. Soc. Jpn.* **2019**, *92*, 469−473.
(78) Le, T. H. H.; Mawatari, K.; Shimizu, H.; Kitamori, T. Detection of Zeptomole Quantities of Nonfluorescent Molecules in a 10^1 Nm Nanochannel by Thermal Lens Microscopy. *Analyst* **2014**, *139*, 2721−2725.
(79) Cassano, C. L.; Mawatari, K.; Kitamori, T.; Fan, Z. H. Thermal Lens Microscopy as a Detector in Microdevices. *Electrophoresis* **2014**, *35*, 2279−2291.
(80) Smirnova, A.; Proskurnin, M. A.; Mawatari, K.; Kitamori, T. Desktop Near-Field Thermal-Lens Microscope for Thermo-Optical Detection in Microfluidics. *Electrophoresis* **2012**, *33*, 2748−2751.
(81) Uchiyama, K.; Hibara, A.; Kimura, H.; Sawada, T.; Kitamori, T. Thermal Lens Microscope. *Jpn. J. Appl. Phys.* **2000**, *39*, 5316.

https://dx.doi.org/10.1021/acsnano.0c07638
ACS Nano 2020, 14, 16414−16445

(82) Kitamori, T.; Tokeshi, M.; Hibara, A.; Sato, K. Peer Reviewed: Thermal Lens Microscopy and Microchip Chemistry. *Anal. Chem.* **2004**, *76*, 52A−60A.
(83) Cognet, L.; Tardin, C.; Boyer, D.; Choquet, D.; Tamarat, P.; Lounis, B. Single Metallic Nanoparticle Imaging for Protein Detection in Cells. *Proc. Natl. Acad. Sci. U. S. A.* **2003**, *100*, 11350−11355.
(84) Tokeshi, M.; Uchida, M.; Uchiyama, K.; Sawada, T.; Kitamori, T. Single- and Countable-Molecule Detection of Non-Fluorescent Molecules in Liquid Phase. *J. Lumin.* **1999**, *83*−*84*, 261−264.
(85) Shimizu, H.; Mawatari, K.; Kitamori, T. Development of a Differential Interference Contrast Thermal Lens Microscope for Sensitive Individual Nanoparticle Detection in Liquid. *Anal. Chem.* **2009**, *81*, 9802−9806.
(86) Shimizu, H.; Mawatari, K.; Kitamori, T. Sensitive Determination of Concentration of Nonfluorescent Species in an Extended-Nano Channel by Differential Interference Contrast Thermal Lens Microscope. *Anal. Chem.* **2010**, *82*, 7479−7484.
(87) Shimizu, H.; Mawatari, K.; Kitamori, T. Detection of Nonfluorescent Molecules Using Differential Interference Contrast Thermal Lens Microscope for Extended Nanochannel Chromatography. *J. Sep. Sci.* **2011**, *34*, 2920−2924.
(88) Cognet, L.; Berciaud, S.; Lasne, D.; Lounis, B. Photothermal Methods for Single Nonluminescent Nano-Objects. *Anal. Chem.* **2008**, *80*, 2288−2294.
(89) Taylor, R. W.; Sandoghdar, V. Interferometric Scattering Microscopy: Seeing Single Nanoparticles and Molecules *via* Rayleigh Scattering. *Nano Lett.* **2019**, *19*, 4827−4835.
(90) Berciaud, S.; Cognet, L.; Lounis, B. Photothermal Absorption Spectroscopy of Individual Semiconductor Nanocrystals. *Nano Lett.* **2005**, *5*, 2160−2163.
(91) Carslaw, H. S.; Jaeger, J. C. *Conduction of Heat in Solids*; Clarendon Press: Oxford, UK, 1959.
(92) Selmke, M.; Cichos, F. The Physics of the Photothermal Detection of Single Absorbing Nano-Objects: A Review. *arXiv: 1510.08669v1*; https://arxiv.org/abs/1510.08669, 2018.
(93) Nisbet, A.; Whittaker, E. T. Hertzian Electromagnetic Potentials and Associated Gauge Transformations. *Proc. R. Soc. London Ser. Math. Phys. Sci.* **1955**, *231*, 250−263.
(94) Gaiduk, A.; Ruijgrok, P. V.; Yorulmaz, M.; Orrit, M. Detection Limits in Photothermal Microscopy. *Chem. Sci.* **2010**, *1*, 343−350.
(95) Ding, T. X.; Hou, L.; van der Meer, H.; Alivisatos, A. P.; Orrit, M. Hundreds-Fold Sensitivity Enhancement of Photothermal Microscopy in Near-Critical Xenon. *J. Phys. Chem. Lett.* **2016**, *7*, 2524−2529.
(96) Parra-Vasquez, A. N. G.; Oudjedi, L.; Cognet, L.; Lounis, B. Nanoscale Thermotropic Phase Transitions Enhancing Photothermal Microscopy Signals. *J. Phys. Chem. Lett.* **2012**, *3*, 1400−1403.
(97) Selmke, M.; Braun, M.; Cichos, F. Nano-Lens Diffraction around a Single Heated Nano Particle. *Opt. Express* **2012**, *20*, 8055−8070.
(98) Selmke, M.; Braun, M.; Cichos, F. Gaussian Beam Photothermal Single Particle Microscopy. *J. Opt. Soc. Am. A* **2012**, *29*, 2237−2241.
(99) Selmke, M. Photothermal Single Particle Detection in Theory & Experiments. Ph.D. Thesis, University of Leipzig, Leipzig, Germany, 2013.
(100) Selmke, M.; Cichos, F. Photothermal Single Particle Rutherford Scattering Microscopy. *Phys. Rev. Lett.* **2013**, *110*, 103901.
(101) Spaeth, P.; Adhikari, S.; Le, L.; Jollans, T.; Pud, S.; Albrecht, W.; Bauer, T.; Caldarola, M.; Kuipers, L.; Orrit, M. Circular Dichroism Measurement of Single Metal Nanoparticles Using Photothermal Imaging. *Nano Lett.* **2019**, *19*, 8934−8940.
(102) Selmke, M.; Schachoff, R.; Braun, M.; Cichos, F. Twin-Focus Photothermal Correlation Spectroscopy. *RSC Adv.* **2013**, *3*, 394−400.
(103) Gaiduk, A.; Yorulmaz, M.; Orrit, M. Correlated Absorption and Photoluminescence of Single Gold Nanoparticles. *ChemPhysChem* **2011**, *12*, 1536−1541.
(104) Gaiduk, A.; Yorulmaz, M.; Ishow, E.; Orrit, M. Absorption, Luminescence, and Sizing of Organic Dye Nanoparticles and of Patterns Formed Upon Dewetting. *ChemPhysChem* **2012**, *13*, 946−951.
(105) Yorulmaz, M.; Khatua, S.; Zijlstra, P.; Gaiduk, A.; Orrit, M. Luminescence Quantum Yield of Single Gold Nanorods. *Nano Lett.* **2012**, *12*, 4385−4391.
(106) Inasawa, S.; Sugiyama, M.; Yamaguchi, Y. Laser-Induced Shape Transformation of Gold Nanoparticles below the Melting Point: The Effect of Surface Melting. *J. Phys. Chem. B* **2005**, *109*, 3104−3111.
(107) Plech, A.; Kotaidis, V.; Grésillon, S.; Dahmen, C.; von Plessen, G. Laser-Induced Heating and Melting of Gold Nanoparticles Studied by Time-Resolved X-Ray Scattering. *Phys. Rev. B: Condens. Matter Mater. Phys.* **2004**, *70*, 195423.
(108) Alkilany, A. M.; Murphy, C. J. Toxicity and Cellular Uptake of Gold Nanoparticles: What We Have Learned so Far? *J. Nanopart. Res.* **2010**, *12*, 2313−2333.
(109) Jia, Y.-P.; Ma, B.-Y.; Wei, X.-W.; Qian, Z.-Y. The *in Vitro* and *in Vivo* Toxicity of Gold Nanoparticles. *Chin. Chem. Lett.* **2017**, *28*, 691−702.
(110) Pissuwan, D.; Niidome, T. Polyelectrolyte-Coated Gold Nanorods and Their Biomedical Applications. *Nanoscale* **2015**, *7*, 59−65.
(111) Basché, T. Photothermal Contrast Reaches Single-Molecule Sensitivity. *Angew. Chem., Int. Ed.* **2011**, *50*, 3602−3604.
(112) Elson, E. L. Fluorescence Correlation Spectroscopy: Past, Present, Future. *Biophys. J.* **2011**, *101*, 2855−2870.
(113) Octeau, V.; Cognet, L.; Duchesne, L.; Lasne, D.; Schaeffer, N.; Fernig, D. G.; Lounis, B. Photothermal Absorption Correlation Spectroscopy. *ACS Nano* **2009**, *3*, 345−350.
(114) Joplin, A.; Chang, W.-S.; Link, S. Imaging and Spectroscopy of Single Metal Nanostructure Absorption. *Langmuir* **2018**, *34*, 3775−3786.
(115) Joplin, A.; Hosseini Jebeli, S. A.; Sung, E.; Diemler, N.; Straney, P. J.; Yorulmaz, M.; Chang, W.-S.; Millstone, J. E.; Link, S. Correlated Absorption and Scattering Spectroscopy of Individual Platinum-Decorated Gold Nanorods Reveals Strong Excitation Enhancement in the Nonplasmonic Metal. *ACS Nano* **2017**, *11*, 12346−12357.
(116) Yorulmaz, M.; Hoggard, A.; Zhao, H.; Wen, F.; Chang, W.-S.; Halas, N. J.; Nordlander, P.; Link, S. Absorption Spectroscopy of an Individual Fano Cluster. *Nano Lett.* **2016**, *16*, 6497−6503.
(117) Johnson, P. B.; Christy, R. W. Optical Constants of the Noble Metals. *Phys. Rev. B* **1972**, *6*, 4370−4379.
(118) van Dijk, M. A.; Tchebotareva, A. L.; Orrit, M.; Lippitz, M.; Berciaud, S.; Lasne, D.; Cognet, L.; Lounis, B. Absorption and Scattering Microscopy of Single Metal Nanoparticles. *Phys. Chem. Chem. Phys.* **2006**, *8*, 3486−3495.
(119) Müller, C. B.; Eckert, T.; Loman, A.; Enderlein, J.; Richtering, W. Dual-Focus Fluorescence Correlation Spectroscopy: A Robust Tool for Studying Molecular Crowding. *Soft Matter* **2009**, *5*, 1358−1366.
(120) Pavlovetc, I. M.; Aleshire, K.; Hartland, G. V.; Kuno, M. Approaches to Mid-Infrared, Super-Resolution Imaging and Spectroscopy. *Phys. Chem. Chem. Phys.* **2020**, *22*, 4313−4325.
(121) Zhang, D.; Lan, L.; Bai, Y.; Majeed, H.; Kandel, M. E.; Popescu, G.; Cheng, J.-X. Bond-Selective Transient Phase Imaging *via* Sensing of the Infrared Photothermal Effect. *Light: Sci. Appl.* **2019**, *8*, 116.
(122) Toda, K.; Tamamitsu, M.; Nagashima, Y.; Horisaki, R.; Ideguchi, T. Molecular Contrast on Phase-Contrast Microscope. *Sci. Rep.* **2019**, *9*, 9957.
(123) Tamamitsu, M.; Toda, K.; Horisaki, R.; Ideguchi, T. Quantitative Phase Imaging with Molecular Vibrational Sensitivity. *Opt. Lett.* **2019**, *44*, 3729−3732.
(124) Nedosekin, D. A.; Galanzha, E. I.; Dervishi, E.; Biris, A. S.; Zharov, V. P. Super-Resolution Nonlinear Photothermal Microscopy. *Small* **2014**, *10*, 135−142.

https://dx.doi.org/10.1021/acsnano.0c07638
ACS Nano 2020, 14, 16414−16445

(125) Huang, X.; Jain, P. K.; El-Sayed, I. H.; El-Sayed, M. A. Plasmonic Photothermal Therapy (PPTT) Using Gold Nanoparticles. *Lasers Med. Sci.* **2008**, *23*, 217.
(126) Huang, X.; El-Sayed, I. H.; Qian, W.; El-Sayed, M. A. Cancer Cell Imaging and Photothermal Therapy in the Near-Infrared Region by Using Gold Nanorods. *J. Am. Chem. Soc.* **2006**, *128*, 2115−2120.
(127) Gobin, A. M.; Lee, M. H.; Halas, N. J.; James, W. D.; Drezek, R. A.; West, J. L. Near-Infrared Resonant Nanoshells for Combined Optical Imaging and Photothermal Cancer Therapy. *Nano Lett.* **2007**, *7*, 1929−1934.
(128) He, J.; Miyazaki, J.; Wang, N.; Tsurui, H.; Kobayashi, T. Label-Free Imaging of Melanoma with Nonlinear Photothermal Microscopy. *Opt. Lett.* **2015**, *40*, 1141−1144.
(129) He, J.; Miyazaki, J.; Wang, N.; Tsurui, H.; Kobayashi, T. Biological Imaging with Nonlinear Photothermal Microscopy Using a Compact Supercontinuum Fiber Laser Source. *Opt. Express* **2015**, *23*, 9762−9771.
(130) Nakata, K.; Tsurui, H.; Kobayashi, T. Further Resolution Enhancement of High-Sensitivity Laser Scanning Photothermal Microscopy Applied to Mouse Endogenous. *J. Appl. Phys.* **2016**, *120*, 214901.
(131) Absil, E.; Tessier, G.; Gross, M.; Atlan, M.; Warnasooriya, N.; Suck, S.; Coppey-Moisan, M.; Fournier, D. Photothermal Heterodyne Holography of Gold Nanoparticles. *Opt. Express* **2010**, *18*, 780−786.
(132) Turko, N. A.; Peled, A.; Shaked, N. T. Wide-Field Interferometric Phase Microscopy with Molecular Specificity Using Plasmonic Nanoparticles. *J. Biomed. Opt.* **2013**, *18*, 111414.
(133) Pache, C.; Bocchio, N. L.; Bouwens, A.; Villiger, M.; Berclaz, C.; Goulley, J.; Gibson, M. I.; Santschi, C.; Lasser, T. Fast Three-Dimensional Imaging of Gold Nanoparticles in Living Cells with Photothermal Optical Lock-in Optical Coherence Microscopy. *Opt. Express* **2012**, *20*, 21385−21399.
(134) Yuan, H.; Khatua, S.; Zijlstra, P.; Orrit, M. Individual Gold Nanorods Report on Dynamical Heterogeneity in Supercooled Glycerol. *Faraday Discuss.* **2014**, *167*, 515−527.
(135) Zondervan, R.; Xia, T.; van der Meer, H.; Storm, C.; Kulzer, F.; van Saarloos, W.; Orrit, M. Soft Glassy Rheology of Supercooled Molecular Liquids. *Proc. Natl. Acad. Sci. U. S. A.* **2008**, *105*, 4993−4998.
(136) Adhikari, S.; Selmke, M.; Cichos, F. Temperature Dependent Single Molecule Rotational Dynamics in PMA. *Phys. Chem. Chem. Phys.* **2011**, *13*, 1849−1856.
(137) Zaytsev, M. E.; Lajoinie, G.; Wang, Y.; Lohse, D.; Zandvliet, H. J. W.; Zhang, X. Plasmonic Bubbles in N-Alkanes. *J. Phys. Chem. C* **2018**, *122*, 28375−28381.
(138) Liu, Y.; Ma, C.; Shen, Y.; Wang, L. V. Bit-Efficient, Sub-Millisecond Wavefront Measurement Using a Lock-in Camera for Time-Reversal Based Optical Focusing inside Scattering Media. *Opt. Lett.* **2016**, *41*, 1321.
(139) Panigrahi, S.; Fade, J.; Agaisse, R.; Ramachandran, H.; Alouini, M. An All-Optical Technique Enables Instantaneous Single-Shot Demodulation of Images at High Frequency. *Nat. Commun.* **2020**, *11*, 549.
(140) Rust, M. J.; Bates, M.; Zhuang, X. Sub-Diffraction-Limit Imaging by Stochastic Optical Reconstruction Microscopy (STORM). *Nat. Methods* **2006**, *3*, 793−796.
(141) Betzig, E.; Patterson, G. H.; Sougrat, R.; Lindwasser, O. W.; Olenych, S.; Bonifacino, J. S.; Davidson, M. W.; Lippincott-Schwartz, J.; Hess, H. F. Imaging Intracellular Fluorescent Proteins at Nanometer Resolution. *Science* **2006**, *313*, 1642−1645.
(142) Sharonov, A.; Hochstrasser, R. M. Wide-Field Subdiffraction Imaging by Accumulated Binding of Diffusing Probes. *Proc. Natl. Acad. Sci. U. S. A.* **2006**, *103*, 18911−18916.
(143) Jungmann, R.; Steinhauer, C.; Scheible, M.; Kuzyk, A.; Tinnefeld, P.; Simmel, F. C. Single-Molecule Kinetics and Super-Resolution Microscopy by Fluorescence Imaging of Transient Binding on DNA Origami. *Nano Lett.* **2010**, *10*, 4756−4761.
(144) Jungmann, R.; Avendaño, M. S.; Woehrstein, J. B.; Dai, M.; Shih, W. M.; Yin, P. Multiplexed 3D Cellular Super-Resolution Imaging with DNA-PAINT and Exchange-PAINT. *Nat. Methods* **2014**, *11*, 313−318.
(145) Schnitzbauer, J.; Strauss, M. T.; Schlichthaerle, T.; Schueder, F.; Jungmann, R. Super-Resolution Microscopy with DNA-PAINT. *Nat. Protoc.* **2017**, *12*, 1198−1228.
(146) Brusnichkin, A. V.; Nedosekin, D. A.; Galanzha, E. I.; Vladimirov, Y. A.; Shevtsova, E. F.; Proskurnin, M. A.; Zharov, V. P. Ultrasensitive Label-Free Photothermal Imaging, Spectral Identification, and Quantification of Cytochrome c in Mitochondria, Live Cells, and Solutions. *J. Biophotonics* **2010**, *3*, 791−806.
(147) Lim, J. M.; Park, C.; Park, J.-S.; Kim, C.; Chon, B.; Cho, M. Cytoplasmic Protein Imaging with Mid-Infrared Photothermal Microscopy: Cellular Dynamics of Live Neurons and Oligodendrocytes. *J. Phys. Chem. Lett.* **2019**, *10*, 2857−2861.
(148) Miyazaki, J.; Iida, T.; Tanaka, S.; Hayashi-Takagi, A.; Kasai, H.; Okabe, S.; Kobayashi, T. Fast 3D Visualization of Endogenous Brain Signals with High-Sensitivity Laser Scanning Photothermal Microscopy. *Biomed. Opt. Express* **2016**, *7*, 1702−1710.
(149) Lasne, D.; Blab, G. A.; Berciaud, S.; Heine, M.; Groc, L.; Choquet, D.; Cognet, L.; Lounis, B. Single Nanoparticle Photothermal Tracking (SNaPT) of 5-Nm Gold Beads in Live Cells. *Biophys. J.* **2006**, *91*, 4598−4604.
(150) Leduc, C.; Jung, J.-M.; Carney, R. R.; Stellacci, F.; Lounis, B. Direct Investigation of Intracellular Presence of Gold Nanoparticles *via* Photothermal Heterodyne Imaging. *ACS Nano* **2011**, *5*, 2587−2592.
(151) Leduc, C.; Si, S.; Gautier, J.; Soto-Ribeiro, M.; Wehrle-Haller, B.; Gautreau, A.; Giannone, G.; Cognet, L.; Lounis, B. A Highly Specific Gold Nanoprobe for Live-Cell Single-Molecule Imaging. *Nano Lett.* **2013**, *13*, 1489−1494.
(152) Duchesne, L.; Octeau, V.; Bearon, R. N.; Beckett, A.; Prior, I. A.; Lounis, B.; Fernig, D. G. Transport of Fibroblast Growth Factor 2 in the Pericellular Matrix Is Controlled by the Spatial Distribution of Its Binding Sites in Heparan Sulfate. *PLoS Biol.* **2012**, *10*, No. e1001361.
(153) Miyazaki, J.; Tsurui, H.; Kawasumi, K.; Kobayashi, T. Optimal Detection Angle in Sub-Diffraction Resolution Photothermal Microscopy: Application for High Sensitivity Imaging of Biological Tissues. *Opt. Express* **2014**, *22*, 18833−18842.
(154) Miyazaki, J.; Tsurui, H.; Kawasumi, K.; Kobayashi, T. Simultaneous Dual-Wavelength Imaging of Nonfluorescent Tissues with 3D Subdiffraction Photothermal Microscopy. *Opt. Express* **2015**, *23*, 3647.
(155) Yu, X.-Y. *In Situ, in Vivo*, and *in Operando* Imaging and Spectroscopy of Liquids Using Microfluidics in Vacuum. *J. Vac. Sci. Technol., A* **2020**, *38*, 040804.
(156) Ross, F. M. Opportunities and Challenges in Liquid Cell Electron Microscopy. *Science* **2015**, *350*, aaa9886.
(157) Chen, Q.; Smith, J. M.; Park, J.; Kim, K.; Ho, D.; Rasool, H. I.; Zettl, A.; Alivisatos, A. P. 3D Motion of DNA-Au Nanoconjugates in Graphene Liquid Cell Electron Microscopy. *Nano Lett.* **2013**, *13*, 4556−4561.
(158) Scotuzzi, M.; Kuipers, J.; Wensveen, D. I.; de Boer, P.; Hagen, K. C W.; Hoogenboom, J. P.; Giepmans, B. N. G. Multi-Color Electron Microscopy by Element-Guided Identification of Cells, Organelles and Molecules. *Sci. Rep.* **2017**, *7*, 45970.
(159) Spence, G. T.; Hartland, G. V.; Smith, B. D. Activated Photothermal Heating Using Croconaine Dyes. *Chem. Sci.* **2013**, *4*, 4240−4244.
(160) Shibu, E. S.; Varkentina, N.; Cognet, L.; Lounis, B. Small Gold Nanorods with Tunable Absorption for Photothermal Microscopy in Cells. *Adv. Sci.* **2017**, *4*, 1600280.
(161) Vermeulen, P.; Cognet, L.; Lounis, B. Photothermal Microscopy: Optical Detection of Small Absorbers in Scattering Environments. *J. Microsc.* **2014**, *254*, 115−121.
(162) Tang, Y.; Cohen, A. E. Optical Chirality and Its Interaction with Matter. *Phys. Rev. Lett.* **2010**, *104*, 163901.

https://dx.doi.org/10.1021/acsnano.0c07638
ACS Nano 2020, 14, 16414−16445

(163) Hu, J.; Lawrence, M.; Dionne, J. A. High Quality Factor Dielectric Metasurfaces for Ultraviolet Circular Dichroism Spectroscopy. *ACS Photonics* **2020**, *7*, 36−42.
(164) Hendry, E.; Carpy, T.; Johnston, J.; Popland, M.; Mikhaylovskiy, R. V.; Lapthorn, A. J.; Kelly, S. M.; Barron, L. D.; Gadegaard, N.; Kadodwala, M. Ultrasensitive Detection and Characterization of Biomolecules Using Superchiral Fields. *Nat. Nanotechnol.* **2010**, *5*, 783−787.
(165) Maoz, B. M.; Chaikin, Y.; Tesler, A. B.; Bar Elli, O.; Fan, Z.; Govorov, A. O.; Markovich, G. Amplification of Chiroptical Activity of Chiral Biomolecules by Surface Plasmons. *Nano Lett.* **2013**, *13*, 1203−1209.
(166) Govorov, A. O.; Fan, Z.; Hernandez, P.; Slocik, J. M.; Naik, R. R. Theory of Circular Dichroism of Nanomaterials Comprising Chiral Molecules and Nanocrystals: Plasmon Enhancement, Dipole Interactions, and Dielectric Effects. *Nano Lett.* **2010**, *10*, 1374−1382.
(167) Rafiei Miandashti, A.; Khosravi Khorashad, L.; Kordesch, M. E.; Govorov, A. O.; Richardson, H. H. Experimental and Theoretical Observation of Photothermal Chirality in Gold Nanoparticle Helicoids. *ACS Nano* **2020**, *14*, 4188−4195.
(168) Tran, C. D.; Xu, M. Ultrasensitive Thermal Lens-Circular Dichroism Spectropolarimeter for Small-Volume Samples. *Rev. Sci. Instrum.* **1989**, *60*, 3207−3211.
(169) Schellman, J.; Jensen, H. P. Optical Spectroscopy of Oriented Molecules. *Chem. Rev.* **1987**, *87*, 1359−1399.
(170) Cheng, J. C.; Nafie, L. A.; Stephens, P. J. Polarization Scrambling Using a Photoelastic Modulator: Application to Circular Dichroism Measurement. *J. Opt. Soc. Am.* **1975**, *65*, 1031−1035.
(171) Malon, P.; Keiderling, T. A. A Solution to the Artifact Problem in Fourier Transform Vibrational Circular Dichroism. *Appl. Spectrosc.* **1988**, *42*, 32−38.
(172) Shindo, Y. On the Problems of CD Spectropolarimeter (IV) Artifacts Due to the Light Scattering by Small Particles. *Appl. Spectrosc.* **1985**, *39*, 713−715.
(173) Shindo, Y.; Nakagawa, M.; Ohmi, Y. On the Problems of CD Spectropolarimeters. II: Artifacts in CD Spectrometers. *Appl. Spectrosc.* **1985**, *39*, 860−868.
(174) Shindo, Y.; Nakagawa, M. Circular Dichroism Measurements. I. Calibration of a Circular Dichroism Spectrometer. *Rev. Sci. Instrum.* **1985**, *56*, 32−39.
(175) Jellison, G. E.; Modine, F. A. Two-Modulator Generalized Ellipsometry: Experiment and Calibration. *Appl. Opt.* **1997**, *36*, 8184−8189.
(176) Freedman, T. B.; Cao, X.; Dukor, R. K.; Nafie, L. A. Absolute Configuration Determination of Chiral Molecules in the Solution State Using Vibrational Circular Dichroism. *Chirality* **2003**, *15*, 743−758.
(177) Nafie, L. A. Dual Polarization Modulation: A Real-Time, Spectral-Multiplex Separation of Circular Dichroism from Linear Birefringence Spectral Intensities. *Appl. Spectrosc.* **2000**, *54*, 1634−1645.
(178) Vinegrad, E.; Vestler, D.; Ben-Moshe, A.; Barnea, A. R.; Markovich, G.; Cheshnovsky, O. Circular Dichroism of Single Particles. *ACS Photonics* **2018**, *5*, 2151−2159.
(179) Yamauchi, M.; Mawatari, K.; Hibara, A.; Tokeshi, M.; Kitamori, T. Circular Dichroism Thermal Lens Microscope for Sensitive Chiral Analysis on Microchip. *Anal. Chem.* **2006**, *78*, 2646−2650.
(180) Narushima, T.; Okamoto, H. Circular Dichroism Microscopy Free from Commingling Linear Dichroism *via* Discretely Modulated Circular Polarization. *Sci. Rep.* **2016**, *6*, 35731.
(181) Mawatari, K.; Kubota, S.; Kitamori, T. Circular Dichroism Thermal Lens Microscope in the UV Wavelength Region (UV-CD-TLM) for Chiral Analysis on a Microchip. *Anal. Bioanal. Chem.* **2008**, *391*, 2521−2526.
(182) Keiderling, T. A. Protein and Peptide Secondary Structure and Conformational Determination with Vibrational Circular Dichroism. *Curr. Opin. Chem. Biol.* **2002**, *6*, 682−688.
(183) Gorodetsky, M. L.; Savchenkov, A. A.; Ilchenko, V. S. Ultimate Q of Optical Microsphere Resonators. *Opt. Lett.* **1996**, *21*, 453−455.
(184) Baaske, M.; Vollmer, F. Optical Resonator Biosensors: Molecular Diagnostic and Nanoparticle Detection on an Integrated Platform. *ChemPhysChem* **2012**, *13*, 427−436.
(185) Foreman, M. R.; Swaim, J. D.; Vollmer, F. Whispering Gallery Mode Sensors. *Adv. Opt. Photonics* **2015**, *7*, 168−240.
(186) Kim, E.; Baaske, M. D.; Vollmer, F. Towards Next-Generation Label-Free Biosensors: Recent Advances in Whispering Gallery Mode Sensors. *Lab Chip* **2017**, *17*, 1190−1205.
(187) Jiang, X.; Yang, L. Optothermal Dynamics in Whispering-Gallery Microresonators. *Light: Sci. Appl.* **2020**, *9*, 24.
(188) Jiang, X.; Qavi, A. J.; Huang, S. H.; Yang, L. Whispering-Gallery Sensors. *Matter* **2020**, *3*, 371−392.
(189) Dantham, V. R.; Holler, S.; Barbre, C.; Keng, D.; Kolchenko, V.; Arnold, S. Label-Free Detection of Single Protein Using a Nanoplasmonic-Photonic Hybrid Microcavity. *Nano Lett.* **2013**, *13*, 3347−3351.
(190) Baaske, M. D.; Foreman, M. R.; Vollmer, F. Single-Molecule Nucleic Acid Interactions Monitored on a Label-Free Microcavity Biosensor Platform. *Nat. Nanotechnol.* **2014**, *9*, 933−939.
(191) Baaske, M. D.; Vollmer, F. Optical Observation of Single Atomic Ions Interacting with Plasmonic Nanorods in Aqueous Solution. *Nat. Photonics* **2016**, *10*, 733−739.
(192) Kim, E.; Baaske, M. D.; Vollmer, F. *In Situ* Observation of Single-Molecule Surface Reactions from Low to High Affinities. *Adv. Mater.* **2016**, *28*, 9941−9948.
(193) Kim, E.; Baaske, M. D.; Schuldes, I.; Wilsch, P. S.; Vollmer, F. Label-Free Optical Detection of Single Enzyme-Reactant Reactions and Associated Conformational Changes. *Sci. Adv.* **2017**, *3*, No. e1603044.
(194) Savchenkov, A. A.; Matsko, A. B.; Ilchenko, V. S.; Solomatine, I.; Seidel, D.; Maleki, L. Tunable Optical Frequency Comb with a Crystalline Whispering Gallery Mode Resonator. *Phys. Rev. Lett.* **2008**, *101*, 093902.
(195) Rueda, A.; Sedlmeir, F.; Kumari, M.; Leuchs, G.; Schwefel, H. G. L. Resonant Electro-Optic Frequency Comb. *Nature* **2019**, *568*, 378−381.
(196) Shen, B.; Chang, L.; Liu, J.; Wang, H.; Yang, Q.-F.; Xiang, C.; Wang, R. N.; He, J.; Liu, T.; Xie, W.; Guo, J.; Kinghorn, D.; Wu, L.; Ji, Q.-X.; Kippenberg, T. J.; Vahala, K.; Bowers, J. E. Integrated Turnkey Soliton Microcombs. *Nature* **2020**, *582*, 365−369.
(197) Arnold, S.; Shopova, S. I.; Holler, S. Whispering Gallery Mode Bio-Sensor for Label-Free Detection of Single Molecules: Thermo-Optic *vs.* Reactive Mechanism. *Opt. Express* **2010**, *18*, 281−287.
(198) Vollmer, F.; Braun, D.; Libchaber, A.; Khoshsima, M.; Teraoka, I.; Arnold, S. Protein Detection by Optical Shift of a Resonant Microcavity. *Appl. Phys. Lett.* **2002**, *80*, 4057−4059.
(199) Knapper, K. A.; Heylman, K. D.; Horak, E. H.; Goldsmith, R. H. Chip-Scale Fabrication of High-Q All-Glass Toroidal Microresonators for Single-Particle Label-Free Imaging. *Adv. Mater.* **2016**, *28*, 2945−2950.
(200) Heylman, K. D.; Thakkar, N.; Horak, E. H.; Quillin, S. C.; Cherqui, C.; Knapper, K. A.; Masiello, D. J.; Goldsmith, R. H. Optical Microresonators as Single-Particle Absorption Spectrometers. *Nat. Photonics* **2016**, *10*, 788−795.
(201) Thakkar, N.; Rea, M. T.; Smith, K. C.; Heylman, K. D.; Quillin, S. C.; Knapper, K. A.; Horak, E. H.; Masiello, D. J.; Goldsmith, R. H. Sculpting Fano Resonances To Control Photonic−Plasmonic Hybridization. *Nano Lett.* **2017**, *17*, 6927−6934.
(202) Knapper, K. A.; Horak, E. H.; Vollbrecht, C. H.; Heylman, K. D.; Goldsmith, R. H. Phase-Sensitive Photothermal Imaging of Ultrahigh-Q Polyoxide Toroidal Microresonators. *Appl. Phys. Lett.* **2018**, *113*, 231105.
(203) Hogan, L. T.; Horak, E. H.; Ward, J. M.; Knapper, K. A.; Nic Chormaic, S.; Goldsmith, R. H. Toward Real-Time Monitoring and Control of Single Nanoparticle Properties with a Microbubble Resonator Spectrometer. *ACS Nano* **2019**, *13*, 12743−12757.

https://dx.doi.org/10.1021/acsnano.0c07638
ACS Nano 2020, 14, 16414−16445

(204) Maayani, S.; Martin, L. L.; Carmon, T. Water-Walled Microfluidics for High-Optical Finesse Cavities. *Nat. Commun.* **2016**, *7*, 10435.
(205) Barnes, J. R.; Stephenson, R. J.; Welland, M. E.; Gerber, C.; Gimzewski, J. K. Photothermal Spectroscopy with Femtojoule Sensitivity Using a Micromechanical Device. *Nature* **1994**, *372*, 79−81.
(206) Barnes, J. R.; Stephenson, R. J.; Woodburn, C. N.; O'Shea, S. J.; Welland, M. E.; Rayment, T.; Gimzewski, J. K.; Gerber, Ch. A Femtojoule Calorimeter Using Micromechanical Sensors. *Rev. Sci. Instrum.* **1994**, *65*, 3793−3798.
(207) Krause, A. R.; Van Neste, C.; Senesac, L.; Thundat, T.; Finot, E. Trace Explosive Detection Using Photothermal Deflection Spectroscopy. *J. Appl. Phys.* **2008**, *103*, 094906.
(208) Senesac, L.; Thundat, T. G. Nanosensors for Trace Explosive Detection. *Mater. Today* **2008**, *11*, 28−36.
(209) Arakawa, E. T.; Lavrik, N. V.; Datskos, P. G. Detection of Anthrax Simulants with Microcalorimetric Spectroscopy: Bacillus Subtilis and Bacillus Cereus Spores. *Appl. Opt.* **2003**, *42*, 1757−1762.
(210) Wig, A.; Arakawa, E. T.; Passian, A.; Ferrell, T. L.; Thundat, T. Photothermal Spectroscopy of Bacillus Anthracis and Bacillus Cereus with Microcantilevers. *Sens. Actuators, B* **2006**, *114*, 206−211.
(211) Arakawa, E. T.; Lavrik, N. V.; Rajic, S.; Datskos, P. G. Detection and Differentiation of Biological Species Using Microcalorimetric Spectroscopy. *Ultramicroscopy* **2003**, *97*, 459−465.
(212) Yun, M.; Kim, S.; Lee, D.; Jung, N.; Chae, I.; Jeon, S.; Thundat, T. Photothermal Cantilever Deflection Spectroscopy of a Photosensitive Polymer. *Appl. Phys. Lett.* **2012**, *100*, 204103.
(213) Kim, S.; Lee, D.; Yun, M.; Jung, N.; Jeon, S.; Thundat, T. Multi-Modal Characterization of Nanogram Amounts of a Photosensitive Polymer. *Appl. Phys. Lett.* **2013**, *102*, 024103.
(214) Yamada, S.; Schmid, S.; Larsen, T.; Hansen, O.; Boisen, A. Photothermal Infrared Spectroscopy of Airborne Samples with Mechanical String Resonators. *Anal. Chem.* **2013**, *85*, 10531−10535.
(215) Larsen, T.; Schmid, S.; Grönberg, L.; Niskanen, A. O.; Hassel, J.; Dohn, S.; Boisen, A. Ultrasensitive String-Based Temperature Sensors. *Appl. Phys. Lett.* **2011**, *98*, 121901.
(216) Larsen, T.; Schmid, S.; Villanueva, L. G.; Boisen, A. Photothermal Analysis of Individual Nanoparticulate Samples Using Micromechanical Resonators. *ACS Nano* **2013**, *7*, 6188−6193.
(217) Schmid, S.; Wu, K.; Larsen, P. E.; Rindzevicius, T.; Boisen, A. Low-Power Photothermal Probing of Single Plasmonic Nanostructures with Nanomechanical String Resonators. *Nano Lett.* **2014**, *14*, 2318−2321.
(218) Chien, M.-H.; Brameshuber, M.; Rossboth, B. K.; Schütz, G. J.; Schmid, S. Single-Molecule Optical Absorption Imaging by Nanomechanical Photothermal Sensing. *Proc. Natl. Acad. Sci. U. S. A.* **2018**, *115*, 11150−11155.
(219) Chien, M.-H.; Steurer, J.; Sadeghi, P.; Cazier, N.; Schmid, S. A Nanoelectromechanical Position-Sensitive Detector with Picometer Resolution. *ACS Photonics* **2020**, *7*, 2197.
(220) Qiu, J.; Wei, W. D. Surface Plasmon-Mediated Photothermal Chemistry. *J. Phys. Chem. C* **2014**, *118*, 20735−20749.
(221) Baffou, G.; Quidant, R. Nanoplasmonics for Chemistry. *Chem. Soc. Rev.* **2014**, *43*, 3898−3907.

https://dx.doi.org/10.1021/acsnano.0c07638
ACS Nano 2020, 14, 16414−16445